Response to anonymous Referee #2

Interactive comment on "Comparing Airborne and Satellite Retrievals of Optical and Microphysical Properties of Cirrus and Deep Convective Clouds using a Radiance Ratio Technique"

by Trismono C. Krisna et al.

==========

We thank the reviewer for the time and efforts reading our manuscript and providing valuable comments and suggestions. We have made revisions according to your comments and suggestions, as described below. The reviewer comments are written in roman and while the author responses are in *italic*. The diff file indicating changes in the manuscript is enclosed in the end of this document.

General comments:

The authors utilize an airborne radiometer to evaluate MODIS ice cloud retrievals and determine the impact of photons vertical penetration in remotely-sensed cloud effective radius. In addition, in-situ aircraft observations appear to partially validate their hypothesis on the value of different wavelengths for assessing the cloud microphysical vertical structure. The manuscript is interesting and the idea that different near-infrared wavelengths provide information about the cloud vertical structure is interesting. However, the sampling is very small and the in-situ observations matched with MODIS and the radiometer SMART are limited to a few points, so any solid statistical inference or validation of the authors' algorithm (and assumptions) are difficult. Moreover, I do not think it is well-justified the pre-processing of MODIS reflectances as the derivation of a new MODIS 1640 nm using only the 2130 nm reflectance is unphysical. The authors cite a number of papers for justifying the MODIS corrections, but this is a misinterpretation of the literature results. I am struggling with my recommendations because even though the authors show some interesting results, the analysis is not rigorous, and the comparison between MODIS science team retrievals and their own MODIS cloud retrievals is flawed.

Response of general comments:

The reviewer is rightfully spotted that one scientific question is using multi near-infrared wavelengths to investigate the cloud vertical structure based on the theory of vertical photon transport. We agree, that the limited and not well suited cases investigated in the study are not sufficient to draw general conclusions about the MODIS performance using airborne measurements. The limited number of cases results from the careful selection of measurements which allows to evaluate the radiance measurements and retrieved cloud products. Such comparisons

require almost perfectly collocated measurement between airborne and satellite, which is given by only few flights during the two investigated campaigns (ML-CIRRUS and ACRIDICON-CHUVA). In addition, inappropriate cloud situations had to be rejected. In order to avoid the impression, that the comparison is valid for cirrus and deep convective clouds in general, we strengthen throughout the revised manuscript, that only a case study is presented. The title is changed to:

> *"Comparing airborne and satellite retrievals of cloud optical thickness and particle effective radius using a spectral radiance ratio technique: Two case studies for multilayer cirrus and deep convective clouds"*

It is right, that the treatment of the MODIS measurements is questionable and not well justified in the previous manuscript. The motivation is to use identical wavelength for both SMART and MODIS retrievals. Unfortunately, the SMART measurements in the near-infrared do only cover the MODIS bands centered at \lambda = 1240 nm and 1640 nm. At 2130 nm the uncertainty of SMART is large. Therefore, it could not be included in the study. It is known that MODIS band 6 (\lambda = 1640 nm) has problems with the detector. Using remaining detectors of MODIS band 6 is not possible due to the very limited number of pixel in our cloud cases. Therefore we used the approach by Wang et al. (2006), which indeed was developed for snow surfaces to 'retrieve' MODIS band 6. We think that this approach is justified also for measurements above ice clouds because, the optical properties of ice clouds are very similar to a snow surface (similar refractive index). To some degree this is confirmed by the agreement between restored MODIS band 6 and SMART as shown the revised manuscript (Fig. 4c, 5c, and 6b). In the revised manuscript we also added the motivation and the method of MODIS band 6 more clearly.

==========

Specific comments:

1) The derivation of MODIS band 6 using band 7 is unphysical and the justification based on the results in Wang et al (2006) is misleading as Wang et al. shows that the correction is useful for estimating NDVI, which is a completely different problem. The 2130 nm and 1640 nm have distinctive photon vertical penetration (e.g. your figure 11) so the conversion is unphysical. I do not think the paper can be accepted until they authors use the standard MODIS channels without any correction. I agree that the 1640 nm MODIS channel has issues, so I would suggest the direct use of the 2130 nm channel instead.

Response:

The reviewer is correct that the original approach by Wang et al. (2006) to retrieve MODIS band 6 from band 7 was applied on the basis of NDSI (normalized difference snow index), while in this study we intended to apply comparisons of radiance and retrieval results using the collocation wavelengths between SMART and MODIS. The spectral range covered by SMART is indeed between 300 - 2200 nm. However, the sensitivity decreases for small and large wavelengths depending on the magnitude of radiation. Only the wavelengths range between 400 - 1800 nm provides measurements with reasonable uncertainty. Therefore, a direct comparison with the 2130 nm MODIS band is not possible.

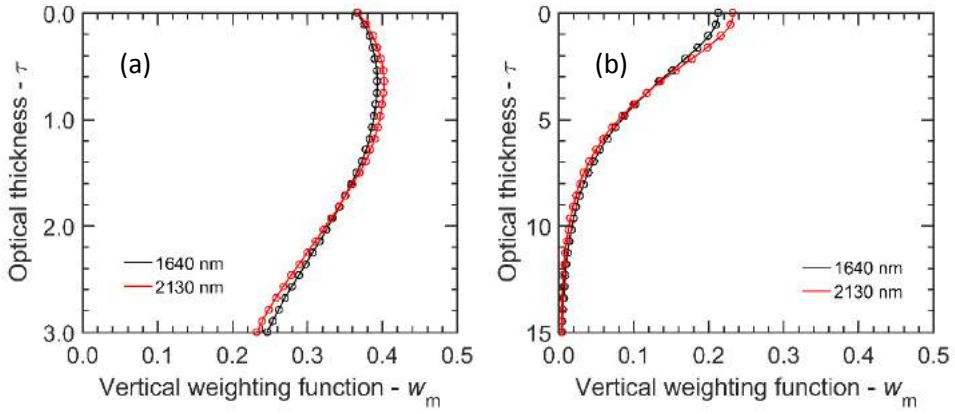

Wang et al. (2006) demonstrated that that snow have similar reflectance characteristics in both wavelengths. Due to similarities on the optical properties of snow and ice clouds, we think that both would also have similar absorptions. Fig. 11 in the manuscript only shows wm up to 2000 nm. To provide more relevant information, we calculated wm at \lambda centered at 1640 nm and 2130 nm as shown in the plots above. (a) is for \tau_ci = 3, while (b) is for (\tau_ci = 15). Our findings illustrate that both wavelengths have almost identical wm for ice clouds, in accordance with findings by Wang et al. (2009) and Zhang et al. (2010). For the two idealized clouds presented in our study, the reff retrieved using 1640 nm and 2130 nm only differs about 0.2-0.4 µm.

Following Wang et al. (2006), we performed a study to investigate and further to parameterize the correlation between band 6 and 7 for measurements of ice clouds. The motivation and technique to retrieve MODIS band 6 is presented in the revised manuscript:

> *"According to Wang et al. (2006), the MODIS radiance band 6 (IM,B6) can be retrieved using band 7 IM,B7 (\lambda = 2130 nm). This technique was originally developed and tested on the basis of snow surface, assuming that the spectral characteristics of the snow reflectivity between MODIS band 6 and 7 does not change significantly for different snow types. Assuming that ice clouds and snow have similar optical properties, the same approach can be applied. Similar to Wang et al. (2006), a parameterization of IM,B6 is*

developed on the basis of radiative transfer simulations of upward radiance performed for cirrus with different \tau and reff. A polynomial fit is applied to quantify the relation between IM,B6 and IM,B7 which result the parameterization:

IM,B6 = -81.033 IM,B7^2 + 3.257 IM,B7 + 0.002 "

"The validity of the parameterization is tested using the remaining detectors of MODIS band 6 for observations above cirrus (not shown here). The linear regression between original and retrieved IM,B6 showed differences below 5% (slope of 0.95 and zero bias) with a correlation coefficient of 0.94."

To develop the parameterization as shown by the Equation above, the simulations are run for different values of \tau (2-7) and reff (10-45 µm). Fig. a below is the scatter plot between radiance band 6 (1640 nm) and band 7 (2130 nm). The dashed line is the linear regression line. The equation is developed by making use of the relation between the two bands. Fig. b is the scatter plot of radiance band 6 original vs. 'retrieved' using the Equation above. Here we see that, the retrieval of MODIS band 6 shows a good performance with a slope of 1, no bias, and R^2= 1.

Finally, as suggested by the first reviewer we compared the radiance from the remaining detectors of MODIS band 6 with the retrieved values to test the validity of this band retrieval technique in real measurements (Fig. c below). Here we compared the remaining detectors of MODIS band 6 and the retrieved values for measurements above clouds. The result confirms the performance and validity of the 'retrieved' MODIS band 6 for cloud measurements.

We do not omit the reviewer suggestion to use 2130 nm in the retrieval. Therefore in Sec. 5 we also run MODIS retrievals using 2130 nm for the comparison with the in situ data. The results is presented in Fig. 14 and Table 4.

"Additionally, the reff retrieved using additional SMART measurements at \lambda = 1500 nm, 1550 nm, and 1700 nm, and also MODIS radiances centered at \lambda = 2130 nm and 3700 nm (band 20) are applied in this comparison."

Here we also found the similarities between the result of \lambda = 1640 nm and 2130 nm showed by the mean value of reff which only differs by 0.3 µm (Table 4).

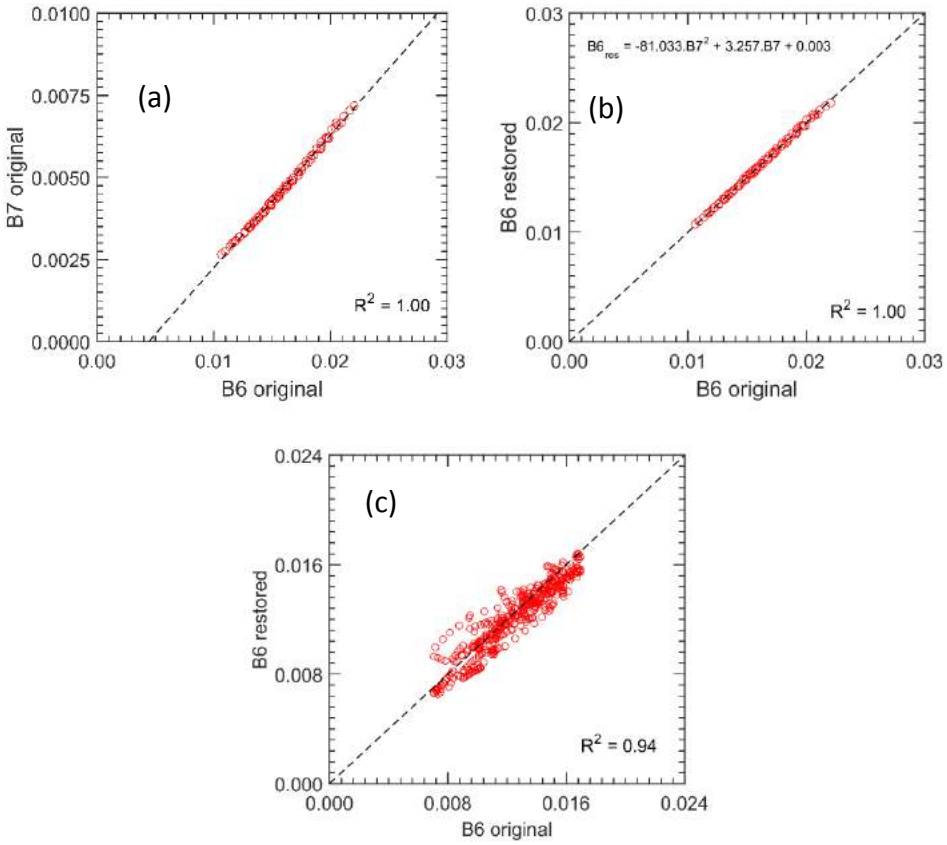

2) The authors correct the MODIS 1240 nm channels using as a justification Lyapustin et al (2014) but, again, the use of this reference is misleading. This paper only corrects MODIS in order to remove a spurious trend. Moreover, the new collection 6 radiances should have incorporated the modifications described in Lyapustin et al. Overall, the use of SMART for correcting MODIS is unjustified. It is much more rigorous to list the differences between SMART and MODIS and then compare the retrievals, keeping in mind the instruments differences.

Response:

It is correct, that without independent standard, we cannot judge, if MODIS or SMART do measure right or wrong. The major justification why we corrected MODIS and used SMART as reference shows up in the cloud retrieval. In the revised manuscript, we added all measured radiances into the LUTs in Fig. 8. Here it is obvious, that the MODIS data does not fall into the parameter space of the forward simulations. While the range of radiance I,645 still matches the simulations, the ratio R_1240 = I,1240/I,645 nm does not. We also could not find any comment about such a bias in literature and also cannot exclude that the forward simulations are biased (effect of ice crystal shape or scattering library), while in this study we already use MODIS collection 6. In order to allow a reasonable retrieval with MODIS data, we finally decided to scale the MODIS band 5 (1240 nm). For both cloud cases, the bias is nearly consistent about 10%. Increasing

retrieval failure in the cirrus case is related to the larger solar zenith angle, which makes the reff LUTs more denser. Therefore small changes in the measurements can lead to a significant bias.

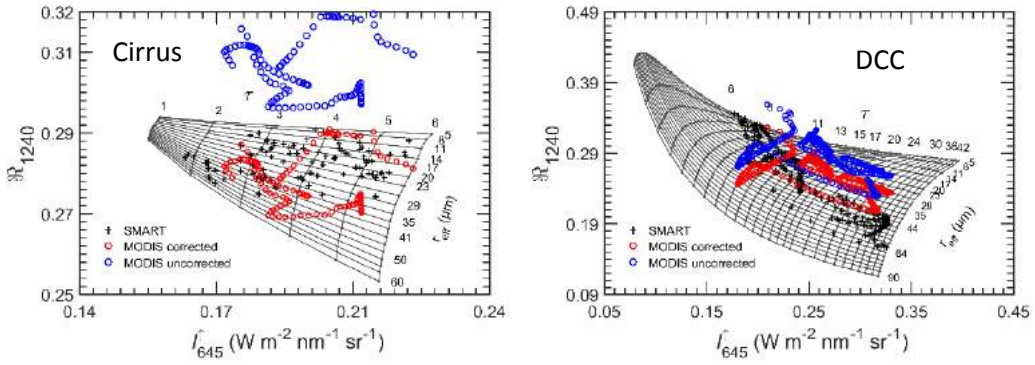

A detailed discussion on the scaling is added to the revised manuscript:

> *"The measurements of SMART (black crosses) and MODIS (blue circles) are included for both scenes in Fig. 8. For the C1 which is based on I_1240, the MODIS data does not match the lookup table solution space. The results in Section 3.3 show clearly, that I_M,1240 are higher than I_S,1240 by about 15%. Using the original I_M,1240 for the cirrus case, all the retrievals of reff are fail because the measurements lie far outside the lookup table solution space (see Fig. 8a), while for the DCC case the retrieval failure is smaller (see Fig. 8c). Enhancing retrieval failure in the cirrus case is due to the larger \theta_0. At a larger \theta_0, the upward radiance becomes more insensitive to the changes of reff and consequently the lookup tables are denser. To gain meaningful retrieved cloud properties, a correction of I_M,1240 is applied. Following Lyapustin et al. (2014), a correction factor g is calculated by the slope of linear regression between I_M,1240 and I_S,1240, which results in g = 0.88 for the cirrus case and g = 0.90 for the DCC case. The corrected I_M,1240 (red circles) are added in Fig. 8 and now match the lookup table solution space. Therefore, all following radiance ratio retrievals for the two cloud cases use these corrected I_M,1240."*

3) A central assumption is the liquid optical depth and effective radius of the layer below the cirrus clouds. The authors choose constant values for each case but these uncertain values can substantially bias the retrievals, and moreover there is no way to know if the constant values are correct or not. So, any comparison with MODIS standard retrievals will have the huge uncertainty due to the liquid optical depth utilized for creating the lookup tables (the use of climatological values is suspicious). This is very problematic because it is unclear whether the new retrievals are better than MODIS. Overall, to prove the point that accurate ice retrievals depend on the ability of accounting for the cloud layer below the cirrus

clouds, you only need synthetic observations, which is why I do not see the point of comparing satellite and airborne remote sensing retrievals.

Response:

As stated by the reviewer, the characterization of the liquid cloud layer is crucial for the retrieval of the cirrus properties and the manuscript did not present this issue properly. Disentangling the contribution of both cloud layers to the total measured radiance is challenging. We used simulations for different combinations of liquid water and cirrus cloud properties and compared the simulated radiance with SMART measurements of the entire spectral range covered by SMART (see figure below). The absorption bands of water vapor (940 and 1135 nm) and the O2 A-band (761 nm) provide some information on the multi-layer structure. Depending on the \tau of the high (cirrus) and low (liquid) cloud layer, absorption features by atmospheric trace gases are stronger or weaker imprinted in the spectral radiance.

Fig. a-c below indicate, that the best fit in the spectral, especially in the absorption bands of water vapor and O2 A-band, was found for \tau_li = 8 and reff_li = 10 µm combined with \tau_ci = 3 and reff_ci = 15 µm. The reff of the liquid cloud is of less importance. If the \tau of the cirrus is sufficiently high, the spectral range used to derive the reff of the cirrus dominated by scattering in the cirrus layer only. In Fig. d, we show the impact of the combination between \tau_ci and \tau_li, which can also give some insights by observing changes in the spectral. For this purpose, we hold \tau_ci + \tau_li = constant with fixed reff_ci = 15 µm and reff_li = 10 µm. Here, again we found the best fit in the spectral is given by \tau_ci = 3 and \tau_li = 8. Underestimation / overestimation of \tau_li will produce gaps, particularly in water vapor absorption bands and O2-A band.

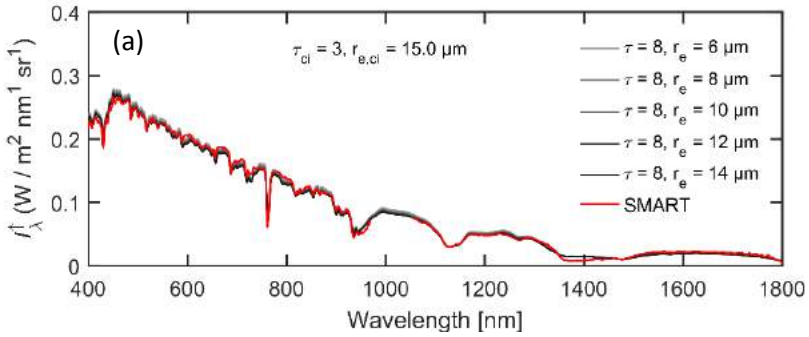

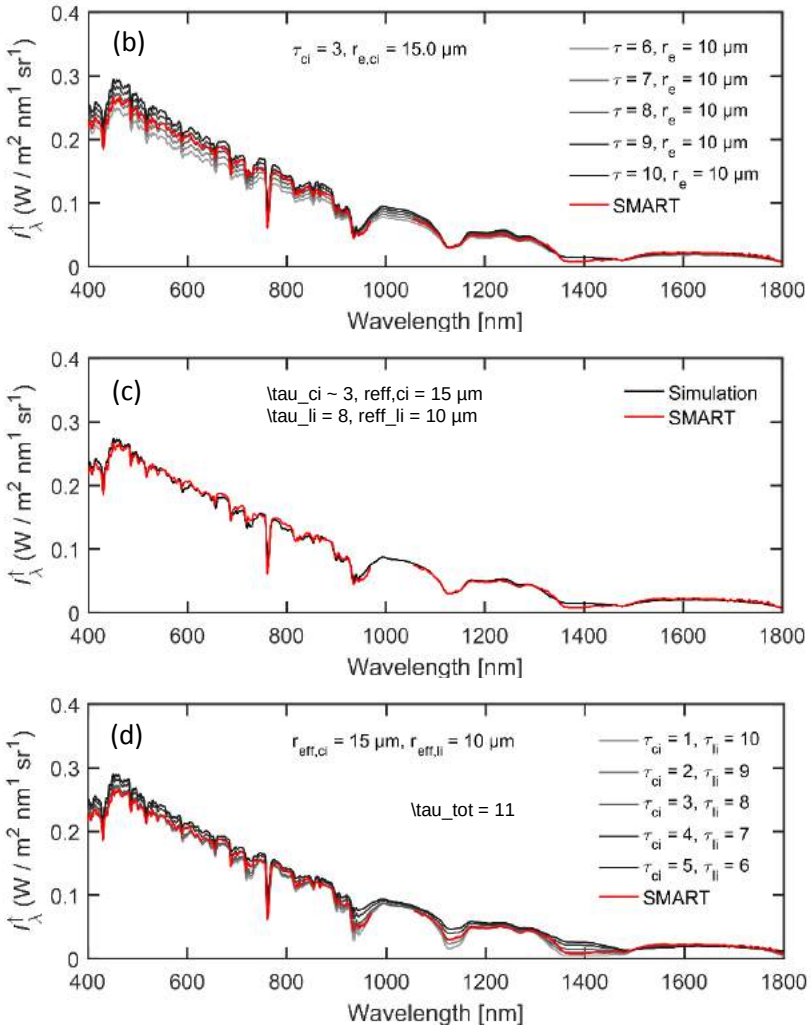

In the revised manuscript, we also considered the variability of the liquid cloud properties along the flight path. To illustrate this problem more clearly, we added a sensitivity study in Sec. 4.2 with respect to the assumed properties of the liquid cloud which provides an estimation of the retrieval uncertainties due to uncertainties in the assumption of the liquid cloud properties.

> *"For the cirrus case, the properties of the low liquid water cloud is assumed to be constant along the flight leg. This assumption might not hold in reality and affect the retrieved cirrus properties. Therefore, the sensitivity of the cirrus retrieval on the assumed properties of the liquid water cloud is quantified using radiative transfer simulations. Spectral radiance are simulated for different combinations of liquid water cloud and cirrus properties. The liquid water cloud is varied for \tau_li = 6 - 10 and reff_li = 6 - 14 µm, while the cirrus is changed for \tau_ci = 2 - 8 and reff_ci = 10 - 40 µm. These simulated radiances are used as synthetic measurements and analyzed with the retrieval algorithm using C2 (I_645 and \Re_1640), which assumes a liquid water cloud with \tau_li = 8 and reff_li = 10 µm. The comparison of synthetically retrieved and original \tau_ci*

and r_eff,ci is shown in Fig. 9. The annotation of "overestimation" (below one-to-one line) and "underestimation" (above one-to-one line) corresponds to when the retrieval is run with an overestimation and underestimation of the properties of liquid water cloud. The retrieved \tau_ci are analyzed in Fig. 9a for different \tau_li, while r_eff,ci and r_eff,li are fixed to 20 µm and 10 µm, respectively. Similarly, the retrieved r_eff,ci are analyzed in Fig. 9b for different r_eff,li but for a fixed combination of \tau_ci = 3 and \tau_li = 8. In general, the simulations show that an overestimation of \tau_li leads to an underestimation of \tau_ci because in this case, the liquid water cloud contribute stronger to the reflected radiation than in reality. Therefore, a smaller \tau_ci is required to match the measurement, and vice versa. For the range of \tau_ci analyzed here, the retrieved \tau_ci is found be over- or underestimated by 1.3 when in reality \tau_li is 6 or 10, while the retrieval assumes \tau_li = 8. These biases of $\tau_ci show, that \tau_li needs to be estimated accurately because a wrong assumption of tau_li almost directly propagates in uncertainties of \tau_ci.

A similar behavior is found for the retrieval of reff_ci, where an overestimation of reff_li leads to an underestimation of reff_ci, and vice versa. Assuming larger liquid droplets than in reality implies that these droplets contribute stronger to the measured absorption at \lambda = 1640 nm, and therefore the ice crystals only contribute less (smaller reff_ci). Fig. 9b illustrates, that the impact of reff_li is strongest when small liquid droplets (reff_li <= 8 µm) are present. For larger liquid droplets (reff_li > 10 µm), the impact is smaller. The maximum uncertainties of reff_ci found for the range of reff_ci and reff_li considered here are about 8 µm for the underestimation of µm which show a tendency of higher uncertainties for higher reff_ci. The retrieval of reff_ci is less affected by reff_li, when the cirrus layer is sufficiently thick (\tau_ci > 5) since the cirrus layer will dominate the reflected radiation in the absorption bands."

4) I find it surprising that the authors did not retrieve effective radius using MODIS 3.78 um channel. If you want to demonstrate that the liquid cloud layer can bias the retrievals, then you have to calculate the effective radius for all the available MODIS channels. In my opinion, the main conclusion of the paper is that accounting for liquid clouds is far more important than accounting for the vertical inhomogeneity.

Response:

It is correct, that to demonstrate the bias due of low liquid cloud, we should use MODIS radiance and run the radiance ratio retrieval considering the low liquid cloud. Therefore in the revised manuscript, we introduced retrievals using MODIS band 7 and band 20 (3700 nm). By doing this, the correlation between the retrieval results with the in situ weighting-estimate reff,w is significantly improved, which*

also can be used to estimate the impact of low liquid cloud. A normalized mean absolute deviation of \zeta= 8.3% and 1.5% for retrieval using 2130 nm and 3700 nm was obtained, where using the reff derived from the MODIS cloud product the \zeta is up to 47.5%. By removing MODIS cloud product in this analysis, overall, the \zeta between in situ reff,w and retrieved reff ranges between 1.5 - 10.3% which falls within the standard deviation (variability of horizontal reff) and considerably as a good agreement. The resulting correlation coefficient R^2 is 0.82 which shows a robust agreement. We changed the discussion in the manuscript accordingly.*

> *"Additionally, the reff retrieved by using additional SMART measurements at \lambda = 1500 nm, 1550 nm, and 1700 nm, and also MODIS radiances centered at \lambda = 2130 nm and 3700 nm (band 20) are applied in this comparison. The retrieval and the calculation of wm for \lambda = 3700 nm are performed by considering both solar and thermal radiation….."*
>
> *"The deviations of in situ reff,w^* and SMART reff range between 3.2% (\lambda = 1500 nm) and 10.3% (\lambda = 1550 nm). Between reff,$w^*$and MODIS reff, the \zeta results in a value between 1.5% for \lambda = 3700 nm and 9.1% for \lambda = 1640 nm. Overall, the values of \zeta are in the range between 1.5 - 10.3% and agree within the horizontal standard deviation, as shown in Fig. 15b."*
>
> *"The reff derived from the MODIS cloud product are obviously affected by the low liquid water cloud, which is not included in the algorithm of MODIS operational retrieval. Therefore, a \zeta of 47.5% and 19.3% are obtained for reff,L,2130 and reff,L,3700, respectively. The absorption by ice crystals at \lambda = 3700 nm is very strong. Consequently, the first top layers will dominate the absorption and significantly reduce the effect of the underlying liquid water cloud. Fig. 15c shows a scatter plot of in situ reff,w^* and reff retrieved from SMART (black triangles) and MODIS (red dots), while the dashed line represents the one-to-one line. There is a robust agreement between in situ reff,w^* and retrieved reff with a correlation coefficient R^2 of 0.82."*

5) In my opinion, the main conclusion of the paper is that accounting for liquid clouds is far more important than accounting for the vertical inhomogeneity.

Response:

A bias of 1 micron is small or not might depend on the related question. We agree, compared to other retrieval uncertainties this is not the major issue and the vertically homogeneous assumption might be sufficient. Also with considering the first reviewer comment, we modified the conclusion in the revised manuscript as follows:

"The variability of particle size distributions, the uncertainties of deriving reff from the in situ measurements, the presence of liquid water cloud below cirrus, and the uncertainties caused by unconstrained choice of ice crystal shapes for the retrievals, are considered as the main contributor which can reveal the discrepancies between in situ and retrieved reff. The assumption of vertically homogeneous cloud in the retrieval algorithm has only a small impact on the retrieval results."

6) I believe collection 6 utilizes a new habit for the lookup table calculations. This new habit appears to produce different results compared to the ice crystal habit of collection 5.

Response:

For the retrievals of the cirrus case, we use GHM based on severely roughened aggregates composed of nine habits (Baum et al., 2014), while the ice crystal habit of plate with high surface roughness (Yang et al., 2013) is applied for the retrievals of the DCC case. The assumption of ice crystal habit considers the measurements by in situ probes. The In the revised manuscript, we added a discussion on the impact of using GHM instead of aggregated columns which is based on the suggested literature.

"These particle habits differ from the MODIS collection 6 retrievals which use severely-roughened compact aggregates of solid columns (so-called aggregated columns) by Yang et al. (2013). A sensitivity study infers that the retrievals assuming GHM and plate generally will result in a larger \tau and smaller reff (not shown here), which is in agreement with findings by van Diedenhoven et al. (2014) and Holz et al. (2016)."

7) I do not see the value of section 5.4. If you deem it necessary, please include the section as a part of the appendix.

We merged and tightened the discussion of the surface albedo in Section 4.1.

"For the cirrus case, the spectral surface albedo \rho of ocean implemented in the forward simulations was measured by SMART. For the DCC case, which is above Amazonian rainforest, no corresponding SMART albedo measurements at low altitude covering exactly the same flight path are available. In this area, the heterogeneity of the surface albedo is very high because where forested and deforested areas are located close to each other. This implies, that a representative assumption of homogeneous surface for the whole flight legs is not appropriate. Therefore, in the DCC case \rho derived from the MODIS BRDF/Albedo product (Strahler et al., 1999) is used to include the horizontal variability of the surface albedo of tropical rainforest."

Reference

Baum, B.A., Yang, P., Heymsfield, A.J., Bansemer, A., Cole, B.H., Merrelli, A., Schmitt, C., Wang, C., 2014. Ice cloud single-scattering property models with the full phase matrix at wavelengths from 0.2 to 100Âμm. J. Quant. Spectrosc. Radiat. Transf. 146, 123–139. https://doi.org/https://doi.org/10.1016/j.jqsrt.2014.02.029

Holz, R.E., Platnick, S., Meyer, K., Vaughan, M., Heidinger, A., Yang, P., Wind, G., Dutcher, S., Ackerman, S., Amarasinghe, N., Nagle, F., Wang, C., 2016. Resolving ice cloud optical thickness biases between CALIOP and MODIS using infrared retrievals. Atmos. Chem. Phys. 16, 5075–5090. https://doi.org/10.5194/acp-16-5075-2016

Lyapustin, A., Wang, Y., Xiong, X., Meister, G., Platnick, S., Levy, R., Franz, B., Korkin, S., Hilker, T., Tucker, J., Hall, F., Sellers, P., Wu, A., Angal, A., 2014. Scientific impact of MODIS C5 calibration degradation and C6+ improvements. Atmos. Meas. Tech. 7, 4353–4365. https://doi.org/10.5194/amt-7-4353-2014

Strahler, A.H., Muller, J.P., Members, M.S.T., 1999. MODIS BRDF/Albedo product: Algorithm Theoretical Basis Document Version 5.0.

van Diedenhoven, B., Fridlind, A.M., Cairns, B., Ackerman, A.S., 2014. Variation of ice crystal size, shape, and asymmetry parameter in tops of tropical deep convective clouds. J. Geophys. Res. Atmos. 119, 11,809-811,825. https://doi.org/10.1002/2014JD022385

Wang, L., Qu, J.J., Xiong, X., Hao, X., Xie, Y., Che, N., 2006. A new method for retrieving band 6 of aqua MODIS. IEEE Geosci. Remote Sens. Lett. 3, 267–270. https://doi.org/10.1109/LGRS.2006.869966

Wang, X., Liou, K.N., Ou, S.S.C., Mace, G.G., Deng, M., 2009. Remote sensing of cirrus cloud vertical size profile using MODIS data. J. Geophys. Res. 114. https://doi.org/10.1029/2008JD011327

Yang, P., Bi, L., Baum, B.A., Liou, K.N., Kattawar, G.W., Mishchenko, M.I., Cole, B., 2013. Spectrall consistent scatterin, absorption, and polarization properties of atmospheric ice crystals at wavelengths from 0.2 to 100 $\mathrm{\mu m}$. J. Atmos. Sci. 70, 330–347.

Zhang, Z.B., Platnick, S., Yang, P., Heidinger, A.K., Comstock, J.M., 2010. Effects of ice particle size vertical inhomogeneity on the passive remote sensing of ice clouds. J. Geophys. Res. 115, D17203. https://doi.org/10.1029/2010JD013835

Comparing ~~Airborne~~ airborne and ~~Satellite Retrievals~~ satellite retrievals of ~~Optical~~ cloud optical thickness and ~~Microphysical Properties of Cirrus and Deep Convective Clouds~~ particle effective radius using a ~~Radiance Ratio Technique~~spectral radiance ratio technique: Two case studies for multilayer cirrus and deep convective clouds

Trismono C. Krisna[1], Manfred Wendisch[1], André Ehrlich[1], Evelyn Jäkel[1], Frank Werner[1,*], Ralf Weigel[3,4], Stephan Borrmann[3,4], Christoph Mahnke[3], Ulrich Pöschl[4], Meinrat O. Andreae[4,6], Christiane Voigt[2,3], and Luiz A. T. Machado[5]

[1]Leipziger Institut für Meteorologie (LIM), Universität Leipzig, Leipzig, Germany
[2]Institut für Physik der Atmosphäre, Deutsches Zentrum für Luft und Raumfahrt (DLR), Oberpfaffenhofen, Germany
[3]Institut für Physik der Atmosphäre, Johannes Gutenberg-Universität Mainz, Mainz, Germany
[4]Biogeochemistry, Multiphase Chemistry, and Particle Chemistry Departments, Max Planck Institute for Chemistry (MPIC), Mainz, Germany
[5]Center of Weather Forecast and Climates Studies, National Institute for Space Research, Sao Jose Dos Campos, Brazil
[6]Scripps Institution of Oceanography, University of California San Diego, La Jolla, California, USA
[*]now at : Joint Center for Earth Systems Technology, University of Maryland, Baltimore, MD, USA

Correspondence to: Trismono Candra Krisna
(trismono_candra.krisna@uni-leipzig.de)

Abstract. Solar radiation reflected by cirrus and deep convective clouds (DCCs) was measured by the Spectral Modular Airborne Radiation Measurement System (SMART) installed on the German HALO (High Altitude and Long Range Research Aircraft) during the ML-CIRRUS and the ACRIDICON-CHUVA campaigns. ~~In~~ On particular flights, HALO performed ~~closely collocated measurements~~ measurements closely collocated with overpasses of the Moderate Resolution Imaging Spectroradiometer (MODIS) on board of the Aqua satellite. A cirrus cloud located above liquid water clouds and a DCC topped by an anvil cirrus are analyzed in this paper. Based on the nadir ~~upward radiance~~spectral upward radiance measured above the clouds, the optical thickness τ and ~~bulk~~ the particle effective radius r_{eff} of the cirrus and DCC are retrieved using a radiance ratio algorithm, which considers the cloud thermodynamic phase, the ~~cloud vertical profile , multi layer~~ vertical profile of cloud microphysical properties, the presence of multilayer clouds, and the heterogeneity of the surface albedo. For the cirrus case, the comparison of ~~τ_{ci} and $r_{\mathrm{eff,ci}}$~~ τ and r_{eff} retrieved on the basis of SMART and MODIS ~~upward radiances~~ measurements yields a normalized mean absolute deviation ~~of 0.5 % for τ_{ci} and 2.5 % for $r_{\mathrm{eff,ci}}$. While for~~ up to 1.2 % for τ and 2.1 % for r_{eff}. For the DCC case, ~~the respective deviation is 5.9 % for τ_{dcc} and 13.2 % for $r_{\mathrm{eff,dcc}}$~~deviations of up to 3.5 % for τ and 6.5 % for r_{eff} are obtained. The larger deviations in ~~case of DCC~~ the DCC case are mainly attributed to the fast cloud evolution and significant three-dimensional radiative effects. Measurements of spectral upward radiance at near-infrared wavelengths ~~with~~

different absorption by cloud particles are employed to investigate the vertical profile of cirrus effective radius r_{eff} in the cirrus. The retrieved values of cirrus effective radius are further r_{eff} are compared with corresponding in situ measurements using a vertical weighting method. Compared to the MODIS observation, spectral observations, measurements of SMART provide an increased amount of more information on the vertical distribution of particle sizes at close to the cloud top, and therefore allow to reconstruct which allow reconstructing the profile of effective radius r_{eff} at cloud top. The retrieved effective radius differs to in situ measurements with comparison between retrieved and in situ values yields a normalized mean absolute deviation between $4 - 19\,\%$, depending on the wavelength chosen in the retrieval algorithm. While, the MODIS cloud product underestimates the in situ measurements by $48\,\%$. The presence of liquid water clouds below the cirrus, the variability of particle size distributions, and the simplification in the retrieval algorithm assuming vertically homogeneous cloud are identified as the potential error contributorswhich ranges between $1.5 - 10.3\,\%$ and a robust correlation coefficient of 0.82.

1 Introduction

Clouds constitute an important component of the global climate system. Covering about $75\,\%$ of the Earth, their high albedo essentially strongly affects to the Earth's energy budget (Wylie et al., 2005; Kim and Ramanathan, 2008; Stubenrauch et al., 2013). In particular, cirrus clouds are not adequately represented in general circulation models. They pose large challenges in predicting future climate changes (Heymsfield et al., 2017) because their coverage regionally can be as high as about $50\,\%$ in the tropics and $30\,\%$ over Europe. Cirrus clouds optically thin cirrus is expected to contribute to a warming of the atmosphere below the cloud, while thick cirrus may cool it (e.g., Liou, 1986; Wendisch et al., 2005, 2007; Voigt et al., 2017). Cirrus reflect solar radiation and reduce the loss of radative radiative energy to space due to absorption of terrestrial radiation and re-emission at a lower temperature (greenhouse effect). Optically thin cirrus is expected to contribute to a warming of the atmosphere below the cloud, while thick cirrus may cool (e.g., Liou, 1986; Wendisch et al., 2005, 2007; Voigt et al., 2017)They pose large challenges in predicting future climate changes (Heymsfield et al., 2017) because they are not adequately represented in general circulation models in spite of the fact that their regional coverage can be as high as about $50\,\%$ in the tropics and $30\,\%$ over Europe.

On the other hand, deep convective clouds (DCCs) alter the radiative energy distribution in the atmosphere by reflection of solar and absorption or emission of terrestrial radiation, as well as by changes of liquid and ice water and hydrometeor profiles (Jensen and Del Genio, 2003; Sherwood et al., 2004; Sohn et al., 2015). Their life cycle is determined by complex microphysical processes including different cloud particle growth/shrinking mechanisms, changes of the thermodynamic phase, and the development of precipitation. DCCs are typically optically thick and often associated with heavy precipitationand severe weather events. In addition, DCCs are related to , strong turbulence, considerable vertical motion, lightning, hail formation and icing (Mecikalski et al., 2007; Lane and Sharman, 2014).

Two important cloud parameters which quantify cloud radiative properties properties which determine the cloud radiative impact are the cloud optical thickness τ and particle effective radius r_{eff} (King et al., 2013). Changes in τ and r_{eff} can lead to a They will decide if a cloud has cooling or warming effect (Slingo, 1990; Shupe and Intrieri, 2004). Passive remote

~~sensing using reflected~~ Several passive remote sensing techniques have been developed to retrieve τ and r_{eff} using spectral upward (cloud-reflected) solar or emitted ~~thermal infrared radiance measured either by satellite or airborne platform is a well–established technique to retrieve cloud properties such as τ and r_{eff} (Stephens and Kummerow, 2007). Cloud properties~~ thermal-infrared radiance measured by airborne and satellite sensors, where the most common technique relies on the bi-spectral methods (e.g., Nakajima and King, 1990; King et al., 1997; Stephens and Kummerow, 2007; Platnick et al., 2017). A radiance ratio method was introduced by Werner et al. (2013), who showed that the use of radiance ratios is capable to reduce the retrieval uncertainties. The cloud properties are retrieved by inversion of radiative transfer model simulations, which is often realized by pre–calculated lookup tables~~(Nakajima and King, 1990; Platnick et al., 2017).~~ .

Airborne remote sensing of cirrus and DCCs properties gives a snapshot of the cloud field only, whereas satellite remote sensing (e.g., MODIS) may provide statistical data on a global scale and record long time series to determine temporal changes of cloud properties (Rosenfeld and Lensky, 1998; Lindsey et al., 2006; Berendes et al., 2008).

~~The performance of post-launch validation activities is crucial to verify~~ Post-launch validation activities of satellite measurements are crucial to verifying the quality of satellite ~~measurement systems~~products. It is essential to address all components of the measurement system, i.e., sensors, algorithms, along with the originally measured radiances and derived data products, and continue validation activities throughout the satellite ~~life~~ lifetime (Larar et al., 2010). Radiance measurements above highly reflecting surfaces such as salt lake, desert, snow/ice (Wan, 2014) and clouds (Mu et al., 2017) are usually evaluated in order to monitor the long term stability of the satellite sensors. An estimated uncertainty of about $1-5\,\%$ in case of MODIS reflective solar bands (RSBs) was reported by Xiong et al. (2003). This measurement ~~uncertainty~~ error propagates into the retrieval results~~(King and Vaughan, 2012). Additionally, uncertainties in the retrieval~~ . Additional uncertainties may arise from ~~errors in the assumed~~ inappropriate assumptions of the surface albedo and ~~three-dimensional (3-D) radiative effects. An~~ the ice crystal habit in case of ice or mixed-phase clouds. According to Rolland and Liou (2001), Fricke et al. (2014), and Ehrlich et al. (2017), an inaccurate assumption of the surface albedo can lead to ~~an uncertainty~~ uncertainties of up to $83\,\%$ for τ and $62\,\%$ for r_{eff}~~(Rolland and Liou, 2001; Fricke et al., 2014; Ehrlich et al., 2017). King et al. (2013) showed that~~ . Eichler et al. (2009) demonstrated, that uncertainties of up to $70\,\%$ for τ and $20\,\%$ for r_{eff} are obtained when an inappropriate ice crystal habit is assumed in cirrus retrievals. Further, the influence of three-dimensional (3-D) radiative effects that can enhance the retrieval ~~uncertainty and~~ uncertainties has been demonstrated by King et al. (2013), and therefore should be considered when ~~interpreting the comparison of retrieved cloud properties~~ analyzing comparisons of cloud properties retrieved from different instruments. ~~In order to reduce these uncertainties, collocated measurements i.e., airborne and satellite remote sensing accompanied with in situ observations are necessary. The similar geometry of airborne and satellite radiation sensors allows for a direct comparison of upward radiance and a stringent validation of methodologies and retrieval algorithms. Platnick (2000), King et al. (2013), Nagao et al. (2013), Miller et al. (2016), and van Diedenhoven et al. (2016) discussed~~ Among others, Platnick (2000) and van Diedenhoven et al. (2016) emphasized the fact that r_{eff} retrieved from reflected solar radiation measurements depends on the vertical penetration of reflected photons into the cloud. At a wavelength with higher absorption by cloud particles, the probability of photons being scattered back out of the cloud without being absorbed decreases. Therefore, retrievals of r_{eff} using different near-infrared wavelengths with different absorption by cloud particles ~~in the retrieval algorithm~~

will result in r_{eff} related to different cloud altitudes. ~~Chang and Li (2002), Chang and Li (2003), and King and Vaughan (2012) showed that airborne-satellite retrievals assuming a vertically homogeneous cloud result in~~ This approach commonly assumes in-cloud vertical homogeneity, where the result is a single bulk value of ~~effective radius~~ r_{eff} representing the entire cloud layer~~where the contribution of each individual layer to the absorption is a function the cloud profile itself and the wavelength chosen in the retrieval~~. Thus, ~~it should be noted that the effective radius retrieved by this technique~~ the retrieved r_{eff} does not represent ~~an effective radius~~ a particle size at a single layer ~~only, and therefore does not represent the real profile of effective radius in the cloud. In reality,~~ as measured by in situ ~~instruments, the cloud~~ observations, where the particle effective radius is sampled at a specific cloud altitude ~~z and it considerably varies as a function of altitude $r_{\mathrm{eff},z}$~~ $r_{\mathrm{eff}}(z)$. These different ~~definitions make difficulties to compare~~ approaches need to be kept in mind when comparing remote sensing and in situ ~~observations and can lead to large discrepancies~~measurements, otherwise a systematic discrepancy might be misinterpreted. A direct comparison at a ~~single cloud layer~~ certain cloud altitude is problematic because it is unclear ~~to~~ for what level the ~~remote sensing~~ retrieved r_{eff} corresponds to the in situ ~~$r_{\mathrm{eff,z}}$. Consequently, this also can reveal significant discrepancies between retrieved an in situ measured cloud water path, as reported in Chang and Li (2003), Chen et al. (2007), and King and Vaughan (2012).~~ r_{eff}.

~~A useful comparison between remote sensing results and in situ measurements can only be made when the full vertical extent of the cloud is measured by an aircraft profiling throughout the cloud. Studies~~ Studies for liquid water clouds by Painemal and Zuidema (2011) and King et al. (2013), who compared the ~~effective radius~~ r_{eff} retrieved from MODIS observations with the ~~average value of effective radius measured in the near cloud top in several cases of in situ profile measurements~~ mean value of r_{eff} measured by cloud probes near the cloud top, revealed absolute deviations of up to 20 %. King et al. (2013) ~~found~~ argued that there is no apparent link between the variation of the ~~effective radius~~ r_{eff} retrieved using different near-infrared wavelengths of MODIS and the vertical structure of ~~effective radius~~ r_{eff} measured by in situ methods. Painemal and Zuidema (2011) identified four ~~potential error sources~~ reasons, such as the variability of droplet size distributions, forming of precipitation, ~~above cloud water vapour absorption~~ water vapor absorption above the cloud, and viewing geometry dependent biases, as potential contributors to the deviation. ~~While, studies by Zhang et al. (2010) and Nagao et al. (2013) argued that the discrepancy between passive remote sensing~~ For cirrus clouds, Wang et al. (2009) and Zhang et al. (2010) demonstrated that the differences between retrievals and in situ measurements ~~is due to~~ are also influenced by the simplification in the retrieval algorithm which assumes in-cloud vertical homogeneity.

Standard satellite retrieval methods such as that applied by MODIS commonly assume a priori, that there is one single homogeneous cloud layer with a specific thermodynamic phase, either liquid water or ice (Platnick et al., 2017). However, studies by Hahn et al. (1984) and Warren et al. (1985) analyzing ground-based observations reported, that the coexistence of multilayer clouds (e.g., cirrus above liquid water clouds) is found in about 50 % of the data. Chang and Li (2005) and Sourdeval et al. (2015) have demonstrated, that omitting the low liquid water cloud in the retrieval algorithm will introduce significant uncertainties in the retrieved cirrus properties.

In order to assess the aspects discussed above, collocated airborne and satellite remote sensing measurements accompanied by in situ observations are necessary. The similar observation geometry of airborne and satellite radiation sensors allows a direct comparison of upward radiance data and a stringent validation of methodologies and retrieval algorithms. The validity of the

retrieval results can be explored by comparison with collocated in situ measurements. This has been realized in this paper for two different cloud cases, a cirrus above low liquid water clouds and a DCC topped by an anvil cirrus.

Measurements of spectral solar radiation using ~~SMART~~ the Spectral Modular Airborne Radiation Measurement System (SMART) installed on board of HALO during the Mid-Latitude Cirrus (ML-CIRRUS) and the Aerosol, Cloud, Precipitation, and Radiation Interaction and Dynamic of Convective Clouds System - Cloud Processes of the Main Precipitation Systems in Brazil: A Contribution to Cloud Resolving Modelling and to the Global Precipitation Measurement (ACRIDICON-CHUVA) ~~campaign~~ campaigns are analyzed. For the purpose of airborne-satellite validation, designated flights above clouds were carried out during ML-CIRRUS and ACRIDICON-CHUVA (Wendisch et al., 2016; Voigt et al., 2017), which were closely collocated with overpasses of the A–Train satellites (Savtchenko et al., 2008). HALO with its long endurance of up to 8 hours and high ceiling of up to 15 km altitude is optimally suited to fly above cirrus and DCCs~~(Wendisch et al., 2016; Voigt et al., 2017). In high altitude~~. High cirrus and DCCs are an appropriate target to perform airborne-satellite comparison because in high altitudes, measurements of upward radiance (cloud-reflected) are only marginally affected by atmospheric interferences due to scattering and absorption by gas molecules and aerosol particles. ~~For the purpose of airborne-satellite validation, designated flights above clouds were carried out during the ML-CIRRUS and ACRIDICON-CHUVA campaign (Wendisch et al., 2016; Voigt et al., 2017) , which were closely collocated with overpasses of the A–Train constellation (Savtchenko et al., 2008).~~

~~Two airborne campaigns~~The two airborne campaigns, involved instrumentations, and satellite observations are introduced in Section ~~?? followed by instrumentation in Section ??~~2. In Section 3, the comparison techniques, data filters, and results of upward radiance comparison are presented. The radiance ratio algorithm ~~,~~ and uncertainty estimation, impact of underlying liquid water cloud on the cirrus retrieval, forward simulation of vertically inhomogeneous cloud, vertical weighting function, ~~heterogeneity of the surface albedo, impact of underlying liquid water cloud,~~ and results of τ and r_{eff} comparison are discussed in Section 4. In Section 5, the methods and results of the comparison between in situ and retrieved effective radius are presented. Finally, the conclusions are given in Section 6.

2 ~~Airborne campaigns~~Observations

2.1 Airborne campaigns

Data from two airborne campaigns with HALO are used in this study. Between 21 March 2014 and 15 April 2014, the ML-CIRRUS campaign performed 16 research flights over Europe and the Atlantic ocean to study nucleation, life-cycle, and climate impact of natural cirrus and ~~aircraft induced~~ aircraft-induced contrail cirrus (Voigt et al., 2017; Schumann et al., 2017). Between 1 September 2014 and 4 October 2014, the ACRIDICON-CHUVA campaign performed 14 research flights combined with satellite and ground-based observations over the Brazilian Amazon rainforest to quantify aerosol-cloud-precipitation interactions and ~~their~~ the thermodynamic, dynamic, and radiative effects of tropical deep convective clouds (DCCs) over the Amazon rainforest (Wendisch et al., 2016).

~~The flight trajectory of ML-15 (a) and AC-18 (b) overlayed with MODIS true color image. The yellow cross indicates the flight section which is selected for the analysis.~~

One common objective of ML-CIRRUS and ACRIDICON-CHUVA was ~~the validation of~~ to compare airborne and satellite measurements and products. ~~Closely~~ Therefore, closely collocated measurements with overpasses of the A-Train ~~during satellite overpasses were performedin order to evaluate optical and microphysical properties of cirrus and DCCs~~satellites were performed. One flight from the ML-CIRRUS flight number 15 (ML-15, 13 April 2014) and another one from the ACRIDICON-CHUVA flight number 18 (AC-18, 28 September 2014) ~~fulfill the requirements of a reliable satellite comparison~~were selected for detailed analyses. The flight ~~trajectory~~ path of ML-15 is shown in Fig. 1a. During the MODIS overpass at 13:55:00 UTC, HALO flew west of Portugal over the North Atlantic. In this area, a wide field of cirrus was located above ~~a~~ low liquid water ~~cloud~~ clouds (stratocumulus). Fig. 1b shows the flight trajectory of AC-18~~. HALO was flying~~ , when HALO flew in the northwest of Brazil over Amazonian rainforest during MODIS overpass at 17:55:00 UTC, where a DCC topped by an anvil cirrus was observed.

3 ~~Instrumentation~~

2.1 Airborne instrumentation

A comprehensive overview of commonly applied airborne instrumentation is given by (Wendisch and Brenguier, 2013). During the ML-CIRRUS and ACRIDICON-CHUVA campaign, a ~~comprehensive set of in situ and remote sensing~~ set of remote sensing and in situ instruments were operated on board of HALO (Wendisch et al., 2016; Voigt et al., 2017). SMART measured spectral upward radiance $I^{\uparrow}_{s,\lambda}$, as well as spectral upward $F^{\uparrow}_{s,\lambda}$ and downward ~~irradiace~~ irradiance $F^{\downarrow}_{s,\lambda}$. The index "s" refers to measurements ~~of~~ by SMART, while λ indicates spectral quantities in units of nm^{-1}. The irradiance data can be used to determine the spectral surface albedo (Wendisch et al., 2001; Wendisch and Mayer, 2003; Wendisch et al., 2004). An active stabilization system keeps the optical inlets in a horizontal position during aircraft movements of up to $\pm$ 6° from the horizontal plane (Wendisch et al., 2001). The spectral resolution defined by the full width at half maximum (FWHM) is 2 - 3 nm for the VNIR spectrometer and 8 - 10 nm for the SWIR spectrometer (Werner et al., 2013).

SMART has two ~~types of separate~~ separate types of spectrometers, which measure in the solar spectrum. The Visible to Near Infrared (VNIR) spectrometer ~~ranges~~ covers wavelengths from 300 - 1000 nm and the Shortwave-Infrared (SWIR) spectrometer ~~ranges~~ covers from 1000 - 2200 nm. ~~Combination~~ The combination of both spectrometers ~~cover~~ covers approximately 97 % of the entire solar spectrum ~~Bierwirth (2008).~~ (Bierwirth, 2008). However, due to the decreasing sensitivity of the spectrometers at small and large wavelengths, the reasonable wavelength range was restricted to 400 - 1800 nm.

~~The spectral resolution defined by the full width at half maximum (FWHM) is 2 - 3 nm for the VNIR spectrometer and 8 - 10 nmfor the SWIR spectrometer (Werner et al., 2013). For the purpose of~~ In this study, ~~we focus on the upward radiance~~ only the radiance data are analyzed. The radiance optical inlet has a field of view (FOV) of 2° looking at nadir (Wolf et al., 2017). The nadir radiance measured by SMART is comparable to measurements of MODIS reflective solar bands (RSBs) in the band number 1 - 19, and 26 ranging between 410 - 2130 µm (Xiong and Barnes, 2006). ~~Primarily,~~ SMART is calibrated radiometrically before, during, and after each campaign using certified calibration standards traceable to NIST (National Institute of Standards and Technology) and by secondary calibration using a travelling standard. The measurement uncertainty of $I^{\uparrow}_{s,\lambda}$ is ~~comprised~~

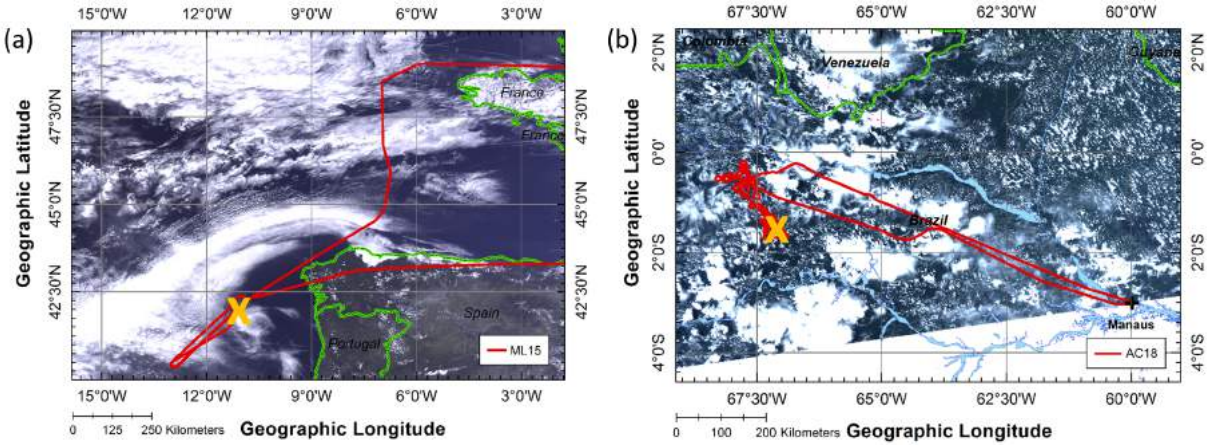

Figure 1. (a) is the HALO flight path of ML-15 on 13 April 2014 while (b) is for AC-18 on 28 September 2014 overlaid with MODIS true color image. The yellow cross indicates the flight section that is selected for the analysis.

~~of~~ determined by the accuracy of the spectral calibration, spectrometer noise and dark current, ~~radiometric calibration, and transfer calibration~~ as well as radiometric and transfer calibrations (Eichler et al., 2009; Brückner et al., 2014; Wolf et al., 2017). The main uncertainty results from the Signal-to-Noise-Ratio (SNR) and the calibration standard, while spectral and transfer calibration errors are ~~almost~~ negligible (Wolf et al., 2017). The resulting total uncertainty is about $4\,\%$ for the VNIR and $10\,\%$ for the SWIR.

The Cloud Combination Probe (CCP) incorporates two separate instruments, the Cloud Droplet Probe (CDP) and the greyscale Cloud Imaging Probe (CIPgs) (Weigel et al., 2016). ~~This way the~~ The CCP overall covers a ~~size~~ diameter range from 2 µm to 960 µm, including large aerosol particles, liquid cloud droplets and small frozen hydrometeors (Klingebiel et al., 2015). The CDP part detects the ~~forward scattered~~ forward-scattered laser light when cloud particles cross the CDP laser beam (Lance et al., 2010). Thus, the CDP provides an improved replacement for the Forward Scattering Spectrometer Probe (FSSP) (Dye and Baumgardner, 1984; Baumgardner et al., 1985). Molleker et al. (2014) ~~characterized the CDP in detail, revealing that the instrument~~ showed, that the CCP exhibits a nominal limit for cloud particle diameters from 3 µm up to 50 µm. The CIPgs records two-dimensional shadow images of cloud particles in a size range from 15 µm up to 960 µm with an optical resolution of 15 µm (Klingebiel et al., 2015; Weigel et al., 2016).

~~Specialized~~ Special algorithms are used to process and analyze the captured images in order to estimate particle number concentrations, particle size distributions, and to differentiate particle shapes (Korolev, 2007). ~~The~~

The CCP measurements are employed to derive the r_{eff} for the comparison with the retrieval products from SMART and MODIS. The r_{eff} from the CCP is derived from the geometrical properties and number of detected particles. Many definitions of r_{eff} exist as summarized in McFarquhar and Heymsfield (1998). In general, r_{eff} as a measure for the cloud radiative properties is defined as the ratio of the third to the second moment of a cloud particle size distribution, implying spheres of equivalent cross-sectional area for any cloud particle shape (McFarquhar and Heymsfield, 1996; Frey et al., 2011). The accuracy of the

cloud particle sizing is conservatively estimated to be about 10 % for spherical particles ~~and correctly assumed refractive indices~~ (Molleker et al., 2014). The sizing uncertainty increases as a function of particles ~~size.~~shape complexity (i.e., when dendrites or particles with elevated aspect ratio were predominating). The size bin limits of the CCP cloud particle data are adapted to reduce ambiguities due to the Mie curve, particularly for cloud particles with small sizes less than 5 µm. The instrument sample volume is calculated as a product of the probe air speed (measurement condition) and the instrument specific effective detection area. All concentration data are corrected concerning the air compression upstream of the underwing cloud probe at the high flight speeds ~~inherent with airborne measurements on board of HALO~~ (Weigel et al., 2016). The robust performance of the specific CCP instrument used in this study was demonstrated by ~~Frey (2011)~~ Frey et al. (2011) for tropical convective outflow, by Molleker et al. (2014) for polar stratospheric clouds~~(PSC)~~, Klingebiel et al. (2015) for low level mixed-phase clouds in the Arctic, as well as by ~~(Braga et al., 2017)~~ Braga et al. (2017) and Cecchini et al. (2017) for tropical convective clouds.

Water vapor was measured by the Water Vapor Analyzer (WARAN), which is a tunable diode laser hygrometer based on the absorption of a laser beam by gaseous water molecules at λ = 1370 nm (Voigt et al., 2014; Kaufmann et al., 2014). The WARAN is installed on the forward-facing HALO trace gas inlet (HALO-TGI). The instrument measures total water, i.e., gas phase plus enhanced ice water content (IWC), in the range between 50 - 40,000 ppm with an accuracy of about $\pm$50 ppm or 5 % of reading. Detailed descriptions about the measurement strategy and uncertainties in the data processing are discussed in Afchine et al. (2017). IWC is derived from the difference between the amount of total enhanced water (H_2O_{tot}) and the amount of gas phase water (H_2O_{gas}) (Kaufmann et al., 2016). Due to the enhancement factor (Voigt et al., 2006) at the HALO-TGI, which is about 20 - 35, the minimum detectable IWC is in the range between 1 - 2000 ppm ($1 - 2000 \times 10^{-2}$ mg m^{-3}). In this study, the IWC is used to obtain the profile of cloud optical thickness $\tau(z)$.

2.2 Satellite observations

Satellite data used in this ~~sudy~~ study stem from the Level 1B Moderate Resolution Imaging Spectroradiometer (MODIS) - Aqua ~~calibrated products MYD021KM.~~ collection 6. Detailed instrument specifications and features of MODIS have been described by Platnick et al. (2003), Xiong and Barnes (2006), and others. The data contain calibrated and geolocated radiances and reflectances for 36 discrete spectral bands distributed between 0.41 µm and 14.2 µm, including 20 ~~RSBs~~ reflective solar bands (RSBs) and 16 thermal emissive bands (TEBs) (Platnick et al., 2003; Xiong and Barnes, 2006), with a nadir horizontal resolutions of about 1 km. The radiances are generated from MODIS Level 1A scans of raw radiance and in the process converted to geophysical units. The solar reflectance values are based on a solar diffuser panel for reflectance calibration up through the RSBs and an accompanying diffuser stability monitor for assessing the stability of the diffuser of up to 1 µm (Platnick et al., 2003). The spectral response is determined by an interference filter overlying a detector array imaging a 10-km along track scene for each scan (40, 20, and 10 elements arrays for the 250 m, 500 m, and 1 km bands, respectively)~~(Platnick et al., 2003)~~. Onboard instruments used for in-orbit radiometric calibration were discussed by Xiong et al. (2003) and Sun et al. (2007).

3 Comparison of upward radiance

3.1 Spectral and spatial resolution adjustment

SMART and MODIS have different ~~different~~ spectral resolutions. MODIS measures in broad spectral bands, while SMART measures ~~a continuous spectrum~~ in much narrower spectral with FWHM between 2 - 10 nm. ~~Therefore, to compare both measurements~~ To allow the comparison, the spectral upward radiance ~~of~~ measured by SMART $I^{\uparrow}_{\mathrm{s},\lambda}$ must be convoluted with the MODIS relative spectral response $R(\lambda)$. The convoluted radiance of SMART $I^{\uparrow}_{\mathrm{S},\lambda}$ is calculated by:

$$I^{\uparrow}_{\mathrm{S},\lambda} = \frac{\int_{\lambda_1}^{\lambda_2} I^{\uparrow}_{\mathrm{s},\lambda} \cdot R(\lambda)\,\mathrm{d}\lambda}{\int_{\lambda_1}^{\lambda_2} R(\lambda)\,\mathrm{d}\lambda}, \tag{1}$$

In this study, upward radiances centered at the MODIS band 1 (λ = 645 nm), band 5 (λ = 1240 nm), and band 6 (λ = 1640 nm) will be primarily used to retrieve τ and r_{eff}. ~~However, it~~ It is known that 15 of the 20 detectors in the MODIS-Aqua band 6 are either nonfunctional or noisy. ~~According to Wang et al. (2006)~~However, according to Wang et al. (2006), the MODIS radiance band 6 $I_{\mathrm{M,B6}}$ can be ~~restored using the MODIS radiance~~ retrieved using band 7 $I_{\mathrm{M,B7}}$ (λ = 2130 nm)~~by:~~. This technique was originally developed and tested on the basis of snow surfaces assuming that the spectral characteristics of the snow reflectivity between MODIS band 6 and 7 do not change significantly for different snow types. Assuming that ice clouds and snow have similar optical properties, the same approach can be applied. Similar to Wang et al. (2006), a parameterization of $I_{\mathrm{M,B6}}$ is developed on the basis of radiative transfer simulations of upward radiance performed for cirrus with different τ and r_{eff}. A polynomial fit is applied to quantify the relation between $I_{\mathrm{M,B6}}$ and $I_{\mathrm{M,B7}}$ which result the parameterization:

$$I_{\mathrm{M,B6}} = 1.6032 - 81.033 \cdot I_{\mathrm{M,B7}}{}^{3} - 1.9458 \cdot I_{\mathrm{M,B7}}{}^{2} + 1.7948 3.257 \cdot I_{\mathrm{M,B7}} + 0.012396, 0.002 \tag{2}$$

The validity of the parameterization is tested using the remaining detectors of MODIS band 6 for observations above cirrus (not shown here). The linear regression between original and retrieved $I_{\mathrm{M,B6}}$ showed differences below 5 % (slope of 0.95 and zero bias) with a correlation coefficient of 0.94.

MODIS data used in this study are delivered at a horizontal resolution of 1 km at nadir, whereas the spatial resolution of SMART varies depending on the flight altitude and temporal resolution. At a flight altitude of 10 km, SMART has a swath of approximately 349 m at the Earth surface. During the two campaigns, the temporal resolution of SMART was between 0.2 - 0.5 s, depending on the measurement conditions. ~~Therefore, this~~ This has to be considered in the data analysis. In order to decrease biases resulting from comparisons of individual measurements, SMART ~~measurements~~ data are averaged over 1 s resolution using a binning method.

3.2 Data filter

Only clouds with a top altitude higher than 8 km are selected for this study. The higher proximity to TOA reduces the influence of scattering and ~~absorbtion~~ absorption by atmospheric molecules and aerosol particles above cloud. Consequently, no correction ~~of~~ for the influence of the atmospheric layer above HALO is needed. To assure a similar viewing zenith angle of

SMART and MODIS, only nadir observations in the center of MODIS swath were selected for the comparison. Werner et al. (2013) discussed that off-nadir measurements of less than 5° may lead to a bias in the retrieved τ and r_{eff} of up to 1 % and 5 %, respectively. To minimize this bias, SMART measurements with roll and pitch angles larger than 3° are discarded and only straight flight legs with altitude changes of less than 50 m are analyzed. ~~Cloud edges are associated with sharp changes in $I^{\uparrow}_{\lambda}$ and 3-D radiative effects. Fisher (2014) discussed variations in cloud height and surface orology to find an offset distance assigned to an uncertainty of ± 40 m. Therefore, the first and the last pixel of MODIS cloudy pixels are masked. For this purpose, the cloud mask algorithm by Ackerman et al. (1998) is employed to discriminate clear and cloudy pixels.~~

~~Comparison of $I^{\uparrow}_{645}$ measurements between SMART and MODIS for an absolute time difference $|\Delta t|$ of $\leq$ 500 s (a) and $\geq$ 500 s (b). Data were taken from ML-15 during 13:40:00 - 14:20:00 UTC.~~

~~MODIS radiance band 1 (λ = 645 nm) for the cirrus case (a) and the DCC case (b) overlayed with the selected flight legs of HALO during cloud measurements (red line). The flight direction is from point A to B.~~

Table 1. Flight descriptions and atmospheric conditions during cloud measurements. Horizontal wind speed ~~HWS~~ v and solar zenith angle θ_0 are averaged during the selected time series.

Flight	Date	Cloud Type	Appearance	z_{t} (km)	Time - UTC (HH:MM:SS)	v ($\mathrm{m\,s^{-1}}$)	θ_0 (°)
ML-15	04/13/2014	Cirrus above liquid cloud	Homogeneous	12	13:56:20 - 13:57:35	21	37
AC-18	09/28/2014	Anvil topped DCC	Inhomogeneous	8	17:56:00 - 17:57:30	9	26

~~MODIS flies~~ The nadir point of MODIS moves much faster than the aircraft. Therefore, it is impossible that SMART and MODIS always measure exactly above each other along the joint flight track. To analyze the effects caused by time shifts between SMART and MODIS measurements, data from the ML-CIRRUS and ACRIDICON-CHUVA are divided into groups within and without a threshold $|\Delta t|$ of 500 s ~~time delay.~~ for the cirrus and 300 s for the DCC. Scatter plots of SMART and MODIS radiance at λ = 645 nm are shown in Fig. 2a ~~yields that the comparison between~~ for the cirrus and Fig. 2b for the DCC. For the cirrus (Fig. 2a), $I^{\uparrow}_{\mathrm{S},645}$ and $I^{\uparrow}_{\mathrm{M},645}$ ~~for $|\Delta t| \leq$ 500 s shows~~ are in a better agreement ~~, while~~ for $|\Delta t| \geq <$ 500 s ~~reveals a scatter as shown in Fig. 2b with the respective~~ with a correlation coefficient R^2 = 0.96, while for $|\Delta t| \leq >$ 500 s ~~and~~ deviations are larger with R^2 = 0.58~~for $|\Delta t| \geq$ 500 s~~. The large scatter for $|\Delta t| \geq >$ 500 s is mainly attributed to the fast horizontal wind speed during cirrus measurements which was 21 $\mathrm{m\,s^{-1}}$ on average. ~~In addition~~Additionally, the wind direction is also a key factor causing a significant cloud drift ~~within~~ for the larger time delay. ~~In case of DCC~~For the DCC (Fig. 2b), the scatter is significantly larger compared to the cirrus for the given threshold of $|\Delta t|$ < 300 s and even worse for the threshold of $|\Delta t|$ > 300 s with R^2 = 0.79 and -0.09, respectively. In this case, the horizontal wind speed ~~was~~ is smaller with an average of 9 $\mathrm{m\,s^{-1}}$~~. However,~~, but the fast cloud evolution is the major issue~~for DCC. Therefore, all comparisons~~. Luo et al. (2014) and Schumacher et al. (2015) reported, that tropical DCCs located at altitude between 6 - 8 km typically have an updraft velocity

about 2 - 4 $\mathrm{m\,s^{-1}}$. According to this analysis, the comparison are restricted to $|\Delta t| \leq < 500$ s ~~.~~ for the cirrus case, while for the DCC case the threshold is tightened to $|\Delta t| < 300$ s.

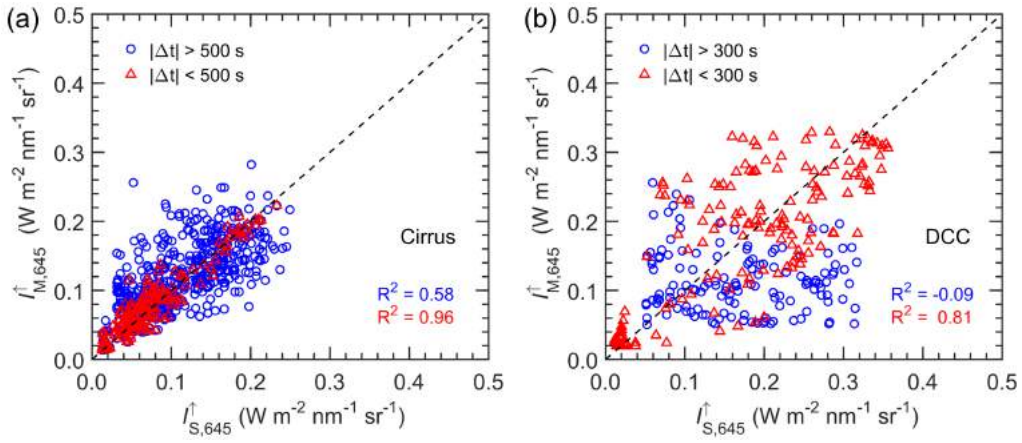

Figure 2. Scatter plots of upward radiance at $\lambda = 645$ nm measured by SMART ($I^{\uparrow}_{S,645}$) and MODIS ($I^{\uparrow}_{M,645}$) within a threshold of 500 s for the cirrus (a) and 300 s the DCC (b). Blue circles and red triangles represents data within and without the predetermined threshold.

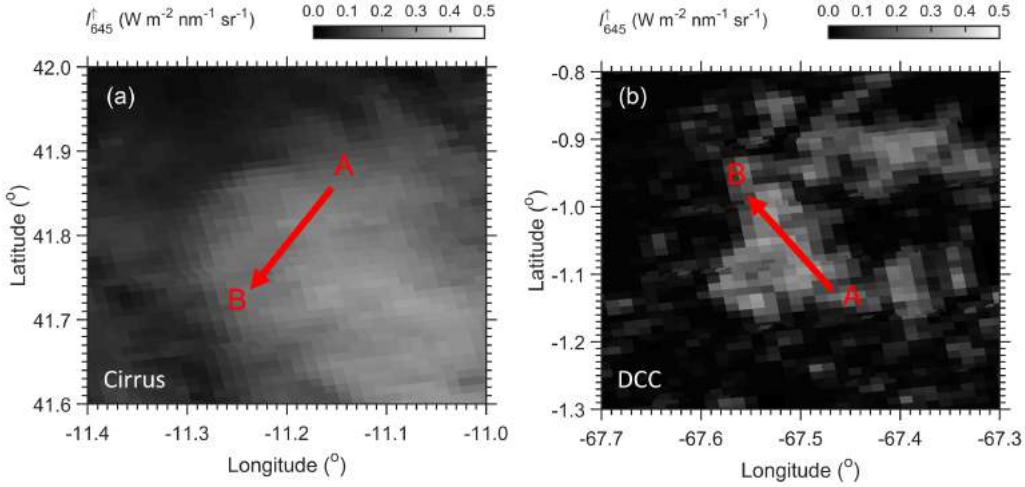

Figure 3. MODIS radiance band 1 ($\lambda = 645$ nm) for the cirrus case (a) and the DCC case (b) superimposed with the selected flight legs of HALO during cloud measurements (red line). The flight direction is from point A to B.

After the filtering, ~~only~~ two suitable cases are left which fulfill ~~all the~~ most requirements of the analysis. The first case, a cirrus cloud located above low liquid water clouds (stratocumulus) is selected from ML-15 between 13:56:20 - 13:57:35 UTC as shown in Fig. 3a. The cloud top altitude z_t of the cirrus was about 12 km while HALO flew at about ~~12.2~~ 12.3 km altitude. The second case, a DCC topped by an anvil cirrus is selected from AC-18 between 17:56:00 - 17:57:30 UTC as presented in Fig.

3b. The ~~cloud top altitude~~ z_t of the selected DCC was about 8 km while HALO flew at 8.3 km altitude. Flight descriptions and atmospheric conditions during cloud measurements are summarized in Table 1. ~~Each case is comprised of a~~ The selected time periods extend to 75 s for the cirrus and 90 s for the DCC case. For HALO ~~flight path at constant altitudes~~flying at constant altitude, those correspond to ~~a horizontal distance~~ horizontal distances of about 15 km and 18 km, respectively. For the MODIS data, the cloud mask algorithm by Ackerman et al. (1998) is employed to discriminate clear and cloudy pixels. Cloud edges are associated with sharp changes of $I^{\uparrow}_{\lambda}$ and 3-D radiative effects. Fisher (2014) discussed variations in cloud height and surface orology to find an offset distance assigned to an uncertainty of $\pm$ 40 m. Therefore, the first and the last pixel of MODIS cloudy pixels are discarded in the data analysis.

3.3 Result of upward radiance comparison

~~Upward radiances measured by SMART and MODIS are compared for the two cloud cases, cirrus and DCC. Fig. ??a shows time series of upward radiance centered at λ = 1240 nm measured by SMART $I^{\uparrow}_{\mathrm{S},1240}$ and MODIS $I^{\uparrow}_{\mathrm{M},1240}$, while Fig. ??b is the scatter plot of the respective measurements. Although the cirrus was located above liquid water clouds, this multi-layer cloud structure does not affect the comparison as it is independent on the target observed by both instruments. It is found, that $I^{\uparrow}_{\mathrm{M},1240}$ measured by MODIS are systematically higher than those measured by SMART $I^{\uparrow}_{\mathrm{S},1240}$. This wavelength is characterized by low absorption by cloud particles, which is useful to retrieve r_{eff} from the lower cloud layer. Consequently, the retrieval of r_{eff} is highly sensitive to small changes in the measurements. At a given 6 % measurement uncertainty, the observed differences of $I^{\uparrow}_{\mathrm{M},1240}$ can result in an uncertainty of up to 50 % in the retrieved r_{eff}. To gain meaningful cloud properties from the retrieval using measurements at this wavelength, $I^{\uparrow}_{\mathrm{M},1240}$ has to be corrected. According to Lyapustin et al. (2014), a correction factor g is calculated by the slope of the linear regression between $I^{\uparrow}_{\mathrm{M},1240}$ and $I^{\uparrow}_{\mathrm{S},1240}$. The resulting g yields a value of 0.86. Thus, the $I^{\uparrow}_{\mathrm{M},1240}$ is corrected by the following equation:~~

$$I^{\uparrow}_{\mathrm{M},1240,\mathrm{cor}} = g \cdot I^{\uparrow}_{\mathrm{M},1240}\,,$$

~~In the following, $I^{\uparrow}_{\mathrm{M},1240}$ always refers to $I^{\uparrow}_{\mathrm{M},1240,\mathrm{cor}}$~~Upward radiances measured by SMART and MODIS are compared for the two selected cloud cases. Fig. 4 shows time series of upward radiance measured by SMART $I^{\uparrow}_{\mathrm{S},\lambda}$ and MODIS $I^{\uparrow}_{\mathrm{S},\lambda}$ centered at λ = 645 nm (a), 1240 nm (b), and ~~2130~~ 1640 nm (c) for the cirrus case, while Fig. 5 ~~is~~ shows the same for the DCC case. ~~Additionally, the~~ Those three wavelengths will be primarily utilized to retrieve the cloud properties in this study. The scatter plots of the respective measurements are shown in Fig. 6. The ~~results show, that the radiance measurements of SMART and MODIS agree better for the cirrus case than for the DCC case. The larger discrepancies in case of DCC are mainly attributed to the fast cloud evolution.~~ time series in Fig. 4 and Fig. 5 illustrate, that the cirrus is more homogeneous along the flight legs compared to the DCC. For the DCC, the cloud anvil is observed between 17:56:00 - 17:56:20 UTC. Later, $I^{\uparrow}_{645}$ increases sharply corresponding to the DCC core and decreases again towards the cloud edge. Fig. 6 shows obviously, that the scatters are larger for the DCC case which are mainly caused by the cloud evolution. For the cirrus case, the scatters are significantly smaller because high cirrus typically change less rapidly.

~~(a) Time series of SMART $I^{\uparrow}_{S,1240}$ (black) and MODIS uncorrected $I^{\uparrow}_{M,1240}$ (red) for the cirrus case. Shaded areas illustrate measurement uncertainties. Gaps on the time series indicate when the shutter of SMART closed for dark current measurements. (b) The scatter plot of the respective measurements. The black line represents a linear regression line.~~

~~Time series of $I^{\uparrow}_{\lambda}$ centered at λ = 645 nm (a), 1240 nm (b), and 1640 nm (d) measured by SMART (black) and MODIS (red) for the cirrus case. $I^{\uparrow}_{M,1240}$ has been corrected using Eq. **??**.~~

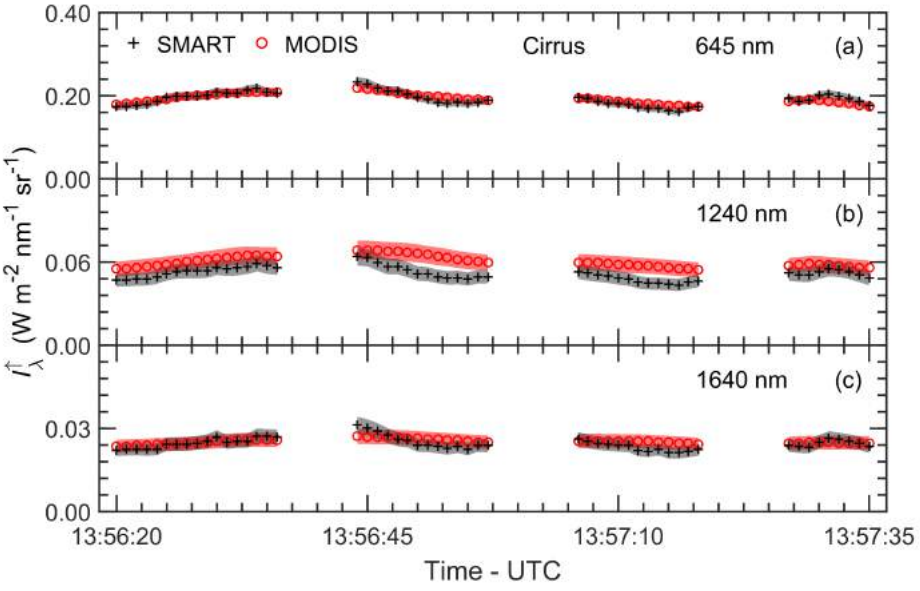

Figure 4. Time series of $I^{\uparrow}_{\lambda}$ centered at λ = 645 nm (a), 1240 nm (b), and 1640 nm (c) measured by SMART (black) and MODIS (red) for the cirrus case. Shaded areas are measurement uncertainties. Gaps on the time series indicate when the shutter of SMART closed for dark current measurements.

~~Fig. 7 shows the comparison of upward radiance measured by SMART and MODIS at reflective solar bands (RSBs) for the cirrus (a) and DCC case (b). Radiance measurements are averaged along the selected time series. The solid line represents spectral radiance measured by SMART $I^{\uparrow}_{s,\lambda}$. $I^{\uparrow}_{S,\lambda}$ represents the convoluted radiance of SMART using Eq. 1, while $I^{\uparrow}_{M,\lambda}$ is the radiance measured by MODIS. The resulting mean $\pm$ standard deviations η are summarized in Table 2. To quantify the agreement between SMART and MODIS measurements, the normalized mean absolute deviation ζ is calculated by:~~

~~$$\zeta = \frac{1}{n}\sum_{i=1}^{n}\left|\frac{x_i - \overline{x}}{\overline{x}}\right|,$$~~

~~where n is the number of the observed values, x_i are the individual values, and $\overline{x}$ is the mean of observed values. In this case, x_i are the mean value of SMART and MODIS measurements along the selected time series. For the purpose of this study, only $I^{\uparrow}_{\lambda}$ centered at λ = 645 nm, 1240 nm, and 1640 nm used in the retrieval of cloud properties are analyzed.~~

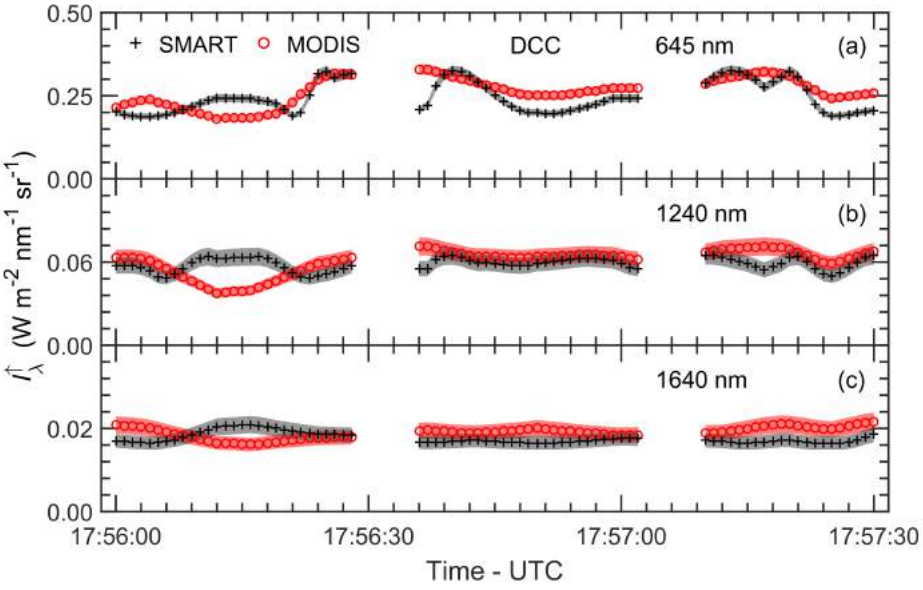

Figure 5. Same as Fig. 4 but for the DCC case.

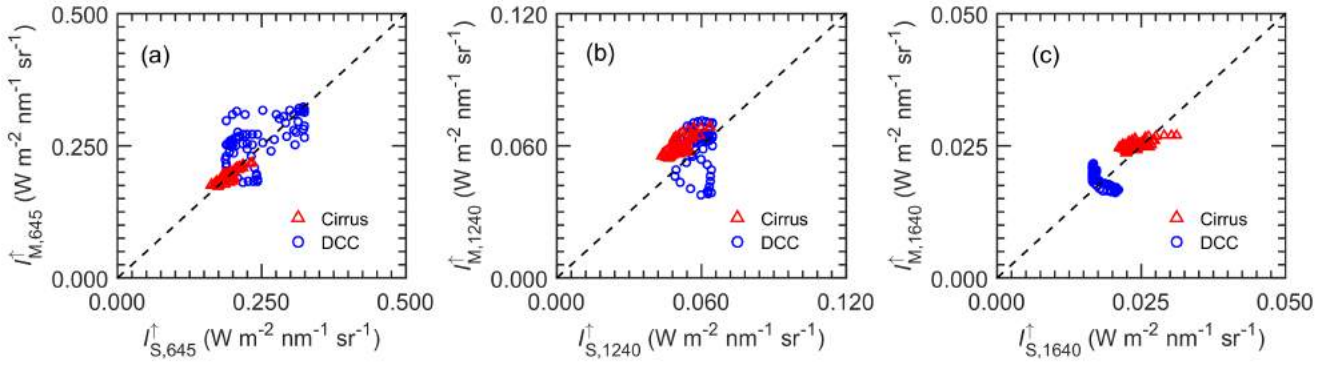

Figure 6. Scatter plots of upward ~~radiances~~ radiance centered at λ = 645 nm (a), 1240 nm (b), and 1640 nm (c) measured by SMART $I^{\uparrow}_{S,\lambda}$ and MODIS $I^{\uparrow}_{M,\lambda}$ ~~. (a), (b), (c) are~~ for the cirrus ~~case, while~~ (dred triangles) ~~, (e), (f) are for~~ and the DCC (blue dotes) case. The ~~black~~ dashed line represents the one-to-one line.

Fig. 7 shows the comparison of mean spectral upward radiance measured by SMART and MODIS for the cirrus (a) and DCC case (b). The solid line represents spectral radiance measured by SMART $I^{\uparrow}_{s,\lambda}$, while $I^{\uparrow}_{S,\lambda}$ is the convoluted radiance of SMART using Eq. 1, and $I^{\uparrow}_{M,\lambda}$ is the radiance measured by MODIS. The values of mean $\pm$ standard deviation η at each spectral

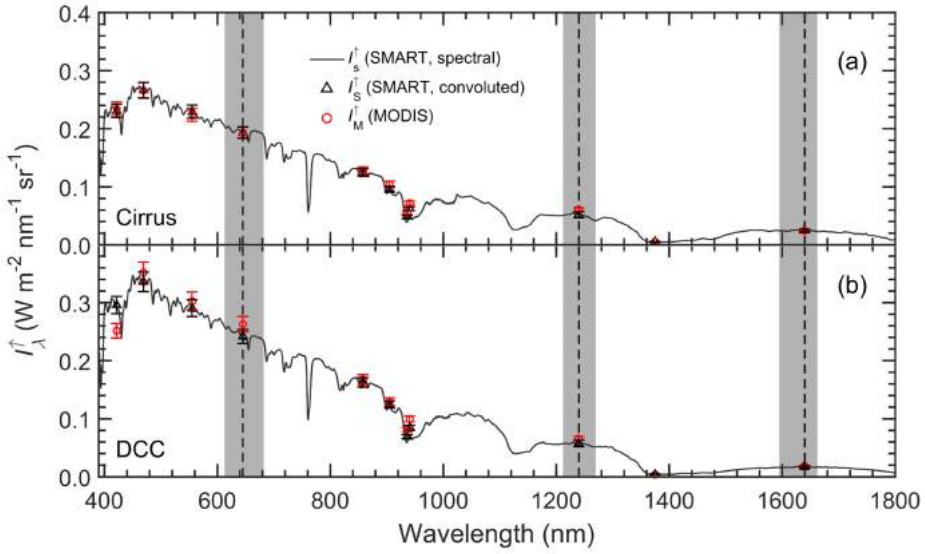

Figure 7. Comparison of mean $I_\lambda^\uparrow$ measured by SMART and MODIS for the cirrus case (a) and the DCC case (b) at ~~RSBs window~~λ between 400 - 1800 nm. Error bars represent measurement uncertainties. Wavelengths centered at λ = 645 nm, 1240 nm, and 1640 nm are indicated by dashed lines while grey band correspond to the interval of MODIS relative spectral response $R(\lambda)$ for the respective wavelengths.

Table 2. Comparison of SMART $I_{\mathrm{S},\lambda}^\uparrow$ and MODIS $I_{\mathrm{M},\lambda}^\uparrow$ for the cirrus (ci) and DCC ~~(dcc)~~ case. η is the mean $\pm$ standard deviation with a subscript of "S" for SMART and "M" for MODIS. ζ is the normalized mean absolute deviation between SMART and MODIS measurements.

λ (nm)	$\eta_{\mathrm{S,ci}}$	$\eta_{\mathrm{M,ci}}$	ζ_{ci} (%)	~~$\eta_{\mathrm{S,dcc}}$~~ $\eta_{\mathrm{S,DCC}}$	~~$\eta_{\mathrm{M,dcc}}$~~ $\eta_{\mathrm{M,DCC}}$	~~ζ_{dcc}~~ ζ_{DCC} (%)
421	0.231 $\pm$ 0.014	0.234 $\pm$ 0.011	0.81	0.295 $\pm$ 0.122	0.251 $\pm$ 0.013	8.06
469	0.266 $\pm$ 0.018	0.265 $\pm$ 0.014	0.20	0.335 $\pm$ 0.149	0.351 $\pm$ 0.050	2.34
555	0.229 $\pm$ 0.018	0.224 $\pm$ 0.013	1.19	0.290 $\pm$ 0.135	0.303 $\pm$ 0.047	2.12
645	0.193 $\pm$ 0.016	0.193 $\pm$ 0.012	0.04	0.241 $\pm$ 0.117	0.263 $\pm$ 0.042	4.25
858	0.125 $\pm$ 0.011	0.128 $\pm$ 0.008	1.29	0.162 $\pm$ 0.069	0.167 $\pm$ 0.018	1.47
905	0.096 $\pm$ 0.008	0.104 $\pm$ 0.007	4.36	0.124 $\pm$ 0.059	0.129 $\pm$ 0.016	1.96
936	0.048 $\pm$ 0.005	0.056 $\pm$ 0.005	7.49	0.069 $\pm$ 0.043	0.080 $\pm$ 0.018	7.95
940	0.062 $\pm$ 0.006	0.071 $\pm$ 0.005	7.18	0.084 $\pm$ 0.047	0.099 $\pm$ 0.018	8.26
1240	0.052 $\pm$ 0.004	~~0.051~~ 0.061 $\pm$ ~~0.003~~ 0.004	~~0.42~~ 7.68	0.057 $\pm$ 0.029	0.065 $\pm$ 0.009	6.72
1375	0.005 $\pm$ 0.001	0.005 $\pm$ 0.001	3.24	0.004 $\pm$ 0.004	0.004 $\pm$ 0.003	6.17
1640	0.024 $\pm$ 0.002	0.025 $\pm$ 0.001	1.36	0.016 $\pm$ 0.010	0.018 $\pm$ 0.001	5.61

wavelength are summarized in Table 2. To quantify the agreement, the normalized mean absolute deviation ζ is calculated by:

$$\zeta = \frac{1}{n}\sum_{i=1}^{n}\left|\frac{x_\mathrm{i} - \overline{x}}{\overline{x}}\right|, \tag{3}$$

where n is the number of observed values, x_i are the individual values, and $\overline{x}$ is the mean value of the radiances measured by SMART and MODIS along the selected time series. For the cirrus case, ζ_{645} is found to be $0.04\,\%$, while ζ_{1240} and ζ_{1640} are ~~$0.42\,\%$~~ $7.68\,\%$ and $1.36\,\%$, respectively. For the DCC case, ζ_{645} yields a value of $4.25\,\%$, while ζ_{1240} and ζ_{1640} are $6.72\,\%$ and $5.61\,\%$, respectively. ~~All~~ The good agreement between SMART $I^{\uparrow}_{\mathrm{S},1640}$ and MODIS $I^{\uparrow}_{\mathrm{M},1640}$ again justifies the application of the retrieval of MODIS band 6 using the parameterization given in Eq. 2. Overall, all the values of ζ ~~are~~ in Table 2 lie within the measurement uncertainties. ~~In case of cirrus, better agreements between~~ The radiance measurements of SMART and MODIS ~~measurements reveal that the cloud evolution is not dominant. The deviations between SMART and MODIS measurements are mainly affected by the horizontal wind speed and wind direction. For the DCC case, in addition of the fast~~ agree better for the cirrus case than for the DCC case. The larger deviations in case of DCC are not only influenced by the cloud evolution, but also due to larger 3-D radiative effects~~are larger~~. Zhang et al. (2011) and King et al. (2013) ~~analyzed~~ estimate the influence of 3-D radiative effects using the cloud heterogeneity index σ_sub, which is calculated ~~by~~ as the ratio of the standard deviation and the mean value of MODIS ~~reflectance~~ radiance band 2. ~~The resulting values of~~ σ_sub ~~range about~~ = 0.1 is obtained for the cirrus case ~~and 0.4 for~~ while the DCC case ~~. The higher values in case of DCC indicates~~ shows higher inhomogeneities with σ_sub = 0.4. These values suggests, that 3-D radiative effects are obviously larger ~~and~~ for the DCC case, and therefore have to be considered ~~in the analysis of~~ when interpreting the retrieval results.

4 ~~Comparison~~ Retrieval of cloud optical thickness τ and particle effective radius r_eff

4.1 Radiance ratio retrieval and uncertainty estimation

A radiance ratio technique adapted from Werner et al. (2013) ~~, Brückner et al. (2014), LeBlanc et al. (2015), Carlsen et al. (2017) , and Ehrlich et al. (2017)~~ is applied to retrieve τ and r_eff of the cirrus and the DCC based on the nadir upward radiance measured by SMART and MODIS. ~~The measurement uncertainties of SMART mostly originate from the radiometric calibration given by the uncertainty of the applied radiation source and the SNR.~~ In case radiance ratios are applied, the uncertainties are reduced because the uncertainties of the radiation source identically influence all measured radiances, and therefore do not contribute to the uncertainty of the ratio. In the radiance ratio algorithm, the upward radiance at the MODIS bands centered at λ_0 = 645 nm (band 1), λ_1 = 1240 nm (band 5), and λ_2 = 1640 nm (band 6) are employed to calculate the following radiance ratios, $\Re_{1240} = I^{\uparrow}_{\lambda_1} / I^{\uparrow}_{\lambda_0}$ and $\Re_{1640} = I^{\uparrow}_{\lambda_2} / I^{\uparrow}_{\lambda_0}$.

In the retrieval algorithm, a decision tree is applied to ~~decide~~ select the retrieval mode. The retrieval can be performed either in the liquid water or ice mode. To decide which mode is used, a cloud phase index I_p is determined by the spectral slope method ~~(Ehrlich et al., 2008; Jäkel et al., 2013).~~ according to Jäkel et al. (2013). In this study, I_p is ~~typically higher~~ defined from the spectral slope of SMART radiance measurements at λ = 1550 nm and 1700 nm, where the value is typically larger than zero

for ice clouds. A threshold of 0.2 is used to discriminate between ice and liquid water clouds. For the cirrus case, time series of I_{p} calculated ~~with the SMART observation~~ from the SMART observations yield values larger than 0.4 indicating ice clouds. This ~~reveals~~indicates, that for the cirrus case the underlying liquid water clouds did not significantly influence I_{p}. Additionally, the high values of I_{p} show that I_{p} is mostly sensitive to the thermodynamic phase of the top cloud layer (cirrus), while the underlying liquid water clouds below the cirrus have a limited influence on the radiances within the wavelength range analyzed for the I_{p}. For the DCC case, I_{p} varies between 0.2 - 0.4 along the time series with a mean value of 0.25. Based on the high I_{p} values, the retrievals in both analyzed cloud cases are performed ~~in the ice mode. However in the cirrus case, to retrieve τ and r_{eff} of the cirrus layer, the underlying liquid water cloud have to be considered in the forward simulations.~~ by assuming ice clouds.

~~Lookup tables for the cirrus case (a,b) and DCC case (c,d). (a) and (c) are using combination 1 ($I^{\uparrow}_{645}$ and $\Re_{1240}$), while (b) and (d) are using combination 2 ($I^{\uparrow}_{645}$ and $\Re_{1640}$). Simulations are performed with solar zenith angle $\theta_0 = 37°$ for the cirrus and $\theta_0 = 26°$ for the DCC case. Ice crystal shape of GHM (Baum et al., 2007) is assumed in the forward simulation.~~

~~To calculate the lookup table,~~ Forward simulations of upward radiance have been performed by 1-D radiative transfer simulations ~~are performed~~ using the radiative transfer package LibRadtran 2.0 (Mayer, 2005; Emde et al., 2016), the discrete ordinate radiative transfer solver (DISORT) version 2 (Stamnes et al., 2000), and ~~assumming~~ assuming vertically homogeneous clouds. The atmospheric profiles of gases and constituents are adapted from the standard profile (Anderson et al., 1986) "mid-latitude" for ML-CIRRUS and "tropical" for ACRIDICON-CHUVA, and are adjusted to radio soundings close to the measurement area. Extraterrestrial spectral irradiance is taken from Gueymard (2004). The standard aerosol particle profile for "spring/summer condition" of "maritime aerosol type" is applied (Shettle, 1989). ~~Droplet optical properties~~ For the cirrus case, the spectral surface albedo ρ of ocean implemented in the forward simulations was measured by SMART. For the DCC case, which is above Amazonian rainforest, no corresponding SMART albedo measurements at low altitude covering exactly the same flight path are available. In this area, the heterogeneity of the surface albedo is very high because forested and deforested areas are located close to each other. This implies, that a representative assumption of a homogeneous surface for the whole flight legs is not appropriate. Therefore, ρ derived from the MODIS BRDF/Albedo product (Strahler et al., 1999) is used to include the horizontal variability of the surface albedo of tropical rainforest.

In the forward simulations, the optical properties of liquid water droplet are derived from Mie calculation (Wiscombe, 1980)~~,~~ ~~while ice properties of~~ . The assumption of ice crystal habit considers ice crystal shapes measured by the in situ probes during the two campaigns (Voigt et al., 2017; Järvinen et al., 2016). For the cirrus, representative ice crystal properties of a general habit mixture ~~(~~based on severely roughened aggregates (so-called GHM) by ~~Baum et al. (2007) are appliedcorresponding to ice crystal shapes measured by in situ probes during the campaigns.~~ Baum et al. (2014) is applied, while for the DCC ice properties of plate with a high surface roughness (Yang et al., 2013) are assumed. These particle habits differ from the MODIS collection 6 retrievals which use severely-roughened compact aggregates of solid columns (so-called aggregated columns) by Yang et al. (2013). A sensitivity study infers that the retrievals assuming GHM and plate generally will result in a larger τ and smaller r_{eff} (not shown here), which is in agreement with findings by van Diedenhoven et al. (2014) and Holz et al. (2016).

The radiance is simulated for both, the actual flight altitude of HALO for the SMART measurements and the top of atmosphere (TOA) for MODIS observations. Due to the high flight altitude no significant differences are observed.

~~The~~ Due to the multilayer cloud situation in the cirrus case, a liquid water cloud layer is considered in the forward simulations. The properties of the liquid water cloud are estimated by comparing the entire spectral signature of the radiance measured by SMART and the simulations assuming different combinations of cloud properties. For the average of the selected time series, a simulation (not shown here) with a liquid water cloud located between 1.5 and 2 km, τ = 8, and r_{eff} = 10 µm shows the best agreements with the measurements in the water vapor absorption bands (e.g., λ = 940 nm and 1135 nm) and the O_2 A-band (λ = 760 nm), which are sensitive to such multilayer cloud conditions (Rozanov and Kokhanovsky, 2004; Wind et al., 2010). The radiance lookup tables for the ~~DCC~~ cirrus case are shown in Fig. 8a and 8b, whereas Fig. 8c and 8d ~~display the lookup tables for the cirrus~~ are for the DCC case. The upward radiance at a non-absorbing wavelength $I^{\uparrow}_{645}$ is combined with $\Re_{1240}$ (~~C1 -~~ combination 1 - C1) and with $\Re_{1640}$ (~~C2 -~~ combination 2 - C2). $I^{\uparrow}_{645}$ is most sensitive to τ, while ratios $\Re_{1240}$ and $\Re_{1640}$ are most sensitive to r_{eff}. For the ~~DCC~~ cirrus case, the lookup tables cover τ between ~~6~~ 1 - ~~40~~ 5 with steps of 1 ~~for τ between 6 - 22 and steps of 2 for τ between 24 - 40, while~~ and r_{eff} ~~ranges~~ between 5 - 60 µm with steps of 3 µm. For the ~~cirrus~~ DCC case, the lookup tables cover τ between ~~1~~ 6 - ~~5~~ 40 with steps of 1 ~~and~~ for τ between 6 - 22 and steps of 2 for τ between 24 - 40, while r_{eff} ranges between 5 - ~~60~~ 90 µm with steps of 3 µm ~~. Due to the underlying liquid water cloud during the cirrus case, the simulations are performed with two cloud layers. Homogeneous liquid water clouds with fixed τ = 8 and~~ for r_{eff} ~~= 10~~ between 5 - 56 µm ~~located between 1.5~~ and steps of 4 µm for r_{eff} between 60 - ~~2 km are applied in the radiative transfer simulations. The properties of liquid water cloud are estimated by comparing simulated and measured spectral radiance averaged over the selected time series, where the r_{eff} of liquid water cloud agrees with values of in situ climatological data reported in e. g., Miles et al. (2000). The lookup tables~~ 90 µm.

The measurements of SMART (black crosses) and MODIS (blue circles) are included for both scenes in Fig. 8. For the C1 which is based on $I^{\uparrow}_{1240}$, the MODIS data does not match the lookup table solution space. The results in Section 3.3 show clearly, that $I^{\uparrow}_{\mathrm{M},1240}$ are higher than $I^{\uparrow}_{\mathrm{S},1240}$ by about 15 %. Using the original $I^{\uparrow}_{\mathrm{M},1240}$ for the cirrus case ~~are shifted to higher $I^{\uparrow}_{645}$ because the underlying liquid water cloud enhances the reflected radiation at this wavelength which is dominated by scattering processes. Similar procedures are applied to run the retrievals for the MODIS data. However, the sensor altitude is set fixed at the top of atmosphere (TOA)~~ , all the retrievals of r_{eff} fail because the measurements lie far outside the lookup table solution space (see Fig. 8a), while for the DCC case the retrieval failure is smaller (see Fig. 8c). Enhancing retrieval failure in the cirrus case is due to the larger θ_0. At a larger θ_0, the upward radiance becomes more insensitive to the changes of r_{eff} and consequently the lookup tables are denser. To gain meaningful retrieved cloud properties, a correction of $I^{\uparrow}_{\mathrm{M},1240}$ is applied. Following Lyapustin et al. (2014), a correction factor g is calculated by the slope of linear regression between $I^{\uparrow}_{\mathrm{M},1240}$ and $I^{\uparrow}_{\mathrm{S},1240}$, which results in g = 0.88 for the cirrus case and g = 0.90 for the DCC case. The corrected $I^{\uparrow}_{\mathrm{M},1240}$ (red circles) are added in Fig. 8, which now match the lookup table solution space. Therefore, all following radiance ratio retrievals for the two cloud cases use these corrected $I^{\uparrow}_{\mathrm{M},1240}$.

In the radiance ratio method, ~~estimated~~ measurement uncertainties of 4 % for $I^{\uparrow}_{645}$ and 6 % for $\Re_{1240}$ and $\Re_{1640}$ are considered. ~~Retrieval~~ The retrieval uncertainties are estimated by considering the measurement uncertainties expressed by its double stan-

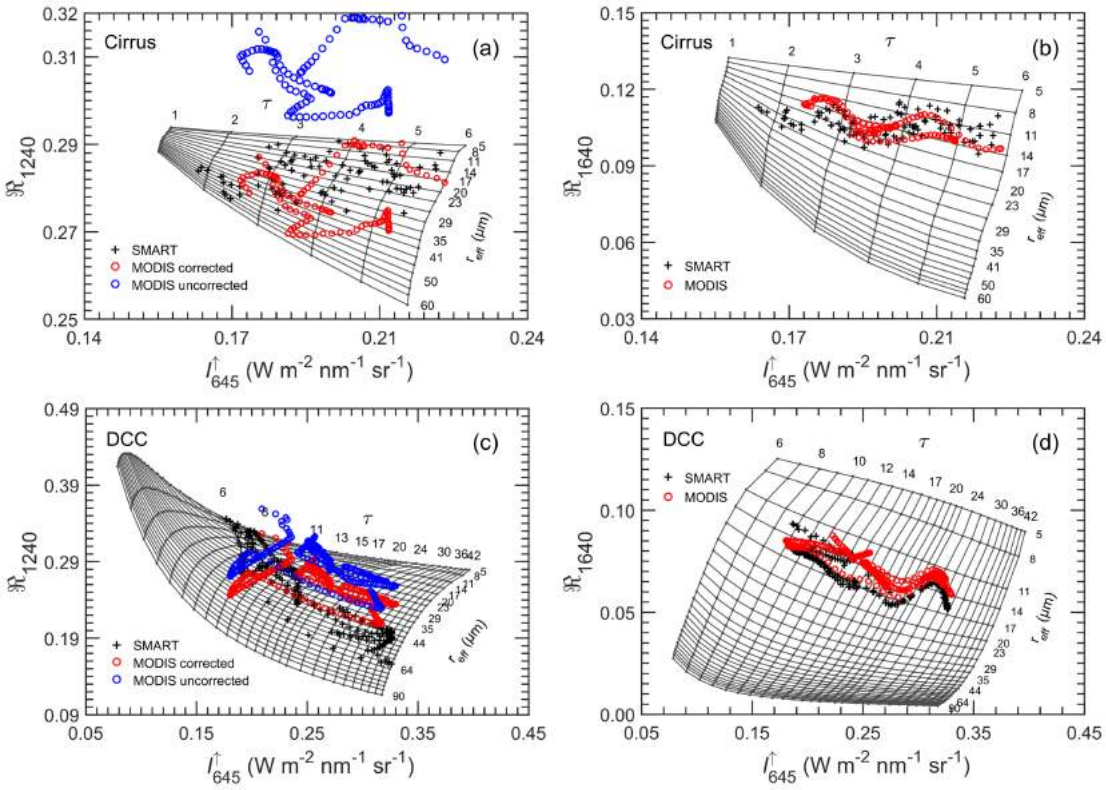

Figure 8. Radiance lookup tables for the cirrus case (a,b) and DCC case (c,d). (a) and (c) are using C1 ($I^{\uparrow}_{645}$ and $\Re_{1240}$), while (b) and (d) are using C2 ($I^{\uparrow}_{645}$ and $\Re_{1640}$). For the cirrus case, the simulations are performed with θ_0 = 37° and assuming GHM (Baum et al., 2014), while for the DCC case θ_0 = 26° and the ice habit of plate (Yang et al., 2013) are applied. Radiance measurements of SMART and MODIS are illustrated by symbols.

dard deviation 2σ. The retrieval is performed by varying each measurements separately by adding and subtracting 2σ which resulted in four solutions. The median of the four solutions is used as the retrieval result of τ and r_{eff}, while the standard deviation is used to represent the retrieval ~~uncertainty~~uncertainties, $\Delta\tau$ for τ and Δr_{eff} for r_{eff}. Note that the ~~retrieval~~ retrievals of r_{eff} using C1 will result in ~~a larger uncertainty compared to~~ larger uncertainties than by using C2 due to smaller absorption by cloud particles at λ = 1240 nm. ~~Consequently~~As a result, the lookup tables of r_{eff} for C1 are more narrow. At a given 6% measurement uncertainty of $\Re_{1240}$, the retrieval can result in uncertainties up 50%.

4.2 Impact of underlying liquid layer clouds on the cirrus retrieval

For the cirrus case~~the uncertainties of the~~ , the properties of the low liquid water cloud are assumed to be constant along the flight legs. This assumption might not hold in reality and affect the retrieved cirrus properties~~are higher due to the additional uncertainties~~ . Therefore, the sensitivity of the cirrus retrieval on the assumed properties of the low liquid water cloud is

quantified using radiative transfer simulations. Spectral upward radiances are simulated for different combinations of liquid water cloud and cirrus properties. The liquid water cloud is varied for τ_{liq} = 6 - 10 and $r_{eff,liq}$ = 6 - 14 µm, while the cirrus is changed for τ_{ci} = 2 - 8 and $r_{eff,ci}$ = 10 - 40 µm. These simulated upward radiances are used as synthetic measurements and analyzed with the retrieval algorithm using C2 ($I^{\uparrow}_{645}$ and $\Re_{1640}$), which assumes a liquid water cloud with τ_{liq} = 8 and $r_{eff,liq}$ = 10 µm. The comparison of synthetically retrieved and original τ_{ci} and $r_{eff,ci}$ is shown in Fig. 9. The annotation of "overestimation" (below one-to-one line) and "underestimation" (above one-to-one line) corresponds to when the retrieval is run with an overestimation and underestimation of the properties of ~~the underlying liquid water clouds.~~ liquid water cloud. The retrieved τ_{ci} are analyzed in Fig. 9a for different τ_{liq}, while $r_{eff,ci}$ and $r_{eff,liq}$ are fixed to 20 µm and 10 µm, respectively. Similarly, the retrieved $r_{eff,ci}$ are analyzed in Fig. 9b for different $r_{eff,liq}$ but for a fixed combination of τ_{ci} = 3 and τ_{liq} = 8. In general, the simulations show that an overestimation of τ_{liq} leads to an underestimation of τ_{ci} because in this case, the liquid water cloud contributes more strongly to the reflected radiation than in reality. Therefore, a smaller τ_{ci} is required to match the measurement, and vice versa. For the range of τ_{ci} analyzed here, the retrieved τ_{ci} is found be over- or underestimated by 1.3 when in reality τ_{liq} is 6 or 10, while the retrieval assumes τ_{liq} = 8. These biases of τ_{ci} show, that τ_{liq} needs to be estimated accurately because a wrong assumption of τ_{liq} almost directly propagates in the uncertainties of τ_{ci}.

A similar behavior is found for the retrieval of $r_{eff,ci}$, where an overestimation of $r_{eff,liq}$ leads to an underestimation of $r_{eff,ci}$, and vice versa. Assuming larger liquid droplets than in reality implies that these droplets contribute more strongly to the measured absorption at λ = 1640 nm, and therefore the ice crystals only contribute less (smaller $r_{eff,ci}$). Fig. 9b illustrates, that the impact of $r_{eff,liq}$ is strongest when small liquid droplets ($r_{eff,liq} \leq 8$ µm) are present. For larger liquid droplets ($r_{eff,liq} > 10$ µm), the impact is reduced. The maximum uncertainties of $r_{eff,ci}$ found for the range of $r_{eff,ci}$ and $r_{eff,liq}$ considered here are about 8 µm for the underestimation of $r_{eff,liq}$, which show a tendency of higher uncertainties for higher $r_{eff,ci}$. The retrieval of $r_{eff,ci}$ is less affected by $r_{eff,liq}$, when the cirrus layer is sufficiently thick ($\tau_{ci} > 5$) since then the cirrus layer will dominate the reflected radiation in the absorption bands.

4.3 Forward simulation of vertically inhomogeneous clouds

It is known from measurements, that the cloud particle sizes can significantly vary with altitudes. For ~~non precipitating~~ nonprecipitating ice clouds, ~~ice crystal sizes typically decrease~~ the ice crystal size typically decreases as a function of altitude ~~(van Diedenhoven et al., 2016; Heymsfield et al., 2017)~~(Heymsfield et al., 2017, e.g.,). However, to simplify the retrieval algorithm vertically homogeneous clouds are commonly assumed in the forward radiative transfer simulations. To quantify the effects of such simplifications, simulations with vertically inhomogeneous ice clouds are performed. Analytical profiles of effective radius as a function of geometrical height are developed ~~according to a formulae~~ using a modified parameterization that was originally proposed by Platnick (2000):

$$r_{\mathrm{eff}}(z,h) = a_0 - \left(a_1 - a_2 \cdot \frac{z}{h}\right)^{1/k}, \tag{4}$$

where the altitude z ranges from 0 at the cloud base to h at the cloud top. ~~Constant $a_0 = r^k_{\mathrm{eff,t}}$ and $a_1 = r^k_{\mathrm{eff,t}} - r^k_{\mathrm{eff,b}}$~~ The parameters $a_0 = r_{\mathrm{eff,t}} + r_{\mathrm{eff,b}}$, $a_1 = r^k_{\mathrm{eff,t}}$, and $a_2 = r^k_{\mathrm{eff,t}} - r^k_{\mathrm{eff,b}}$ are determined from prescribed boundary condition of the

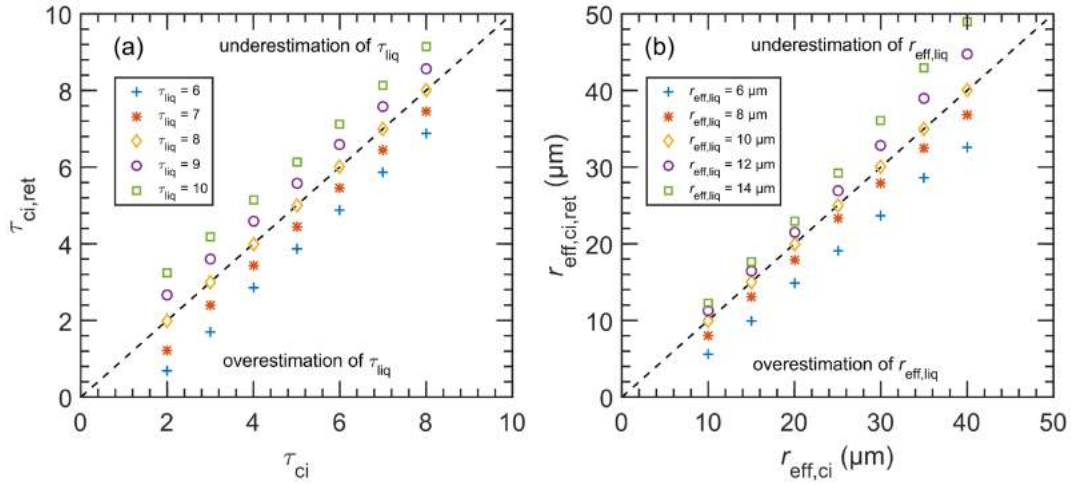

Figure 9. Comparison of synthetically retrieved τ_{ci} (a) and $r_{eff,ci}$ (b). Calculations in (a) are performed by changing τ_{liq} while the original value is 8 and $r_{eff,ci}$ = 20 µm and $r_{eff,liq}$ = 10 µm are fixed. In (b), $r_{eff,liq}$ is changed while the original value is 10 µm and τ_{ci} = 3 and τ_{liq} = 8 are fixed.

cloud top effective radius $r_{\mathrm{eff,t}}$ and the cloud base effective radius $r_{\mathrm{eff,b}}$. To represent a typical vertical structure of ice clouds, k = 3 is chosen. The profiles of effective radius are coupled with the profiles of ice water content, which ~~considerably~~ typically decrease as a function of altitude ~~for ice clouds(Heymsfield et al., 2017)~~in ice clouds.

Table 3. Total optical thickness τ_c, effective radius at cloud top $r_{\mathrm{eff,t}}$ and cloud base $r_{\mathrm{eff,b}}$, ice water content (IWC) from cloud base (CB) to cloud top (CT), with the boundary of geometrical ~~hight~~ height z and thickness h. Retrieved effective radius $r_{\mathrm{eff,ret}}$ is compared to the weighting-estimate $r^*_{\mathrm{eff,w}}$ for two near-infrared wavelengths at λ = 1240 nm and 1640 nm.

	Specification							Validation			
Cloud	τ_c	$r_{\mathrm{eff,b}}$ (µm)	$r_{\mathrm{eff,t}}$ (µm)	k	IWC ($\mathrm{g\,m^{-3}}$)	z_b (km)	z_t (km)	$r^*_{\mathrm{eff,w}}$ (µm) 1240 nm	$r^*_{\mathrm{eff,w}}$ (µm) 1640 nm	$r_{\mathrm{eff,ret}}$ (µm) 1240 nm	$r_{\mathrm{eff,ret}}$ (µm) 1640 nm
A	3	40	10	3	0.1 - 0.04	10	12	~~18.4~~ 18.3	17.7	17.9	17.3
B	15	50	20	3	0.2 - 0.1	6	8	26.6	24.1	26.1	24.0

Fig. 10a and 10b show the profile of effective radius for a representative cirrus (cloud A) and a DCC composed of ice particles only (cloud B). ~~Both~~ The cloud profiles are divided into ~~30~~ 20 layers for the implementation in the radiative transfer simulation~~.~~ ~~Parameters~~, where each layer has a homogeneous thin layer of $\Delta\tau$ = 0.15 for cloud A and 0.75 for cloud B. The parameters used to set up both ~~cloud~~ clouds A and B are summarized in Table 3. Forward radiative transfer simulations are performed to calculate spectral upward radiance above the cloud using an ~~adding/superposition~~ adding-superposition technique from the

cloud top (CT) to the cloud base (CB)~~as described by Platnick (2000). Solar zenith angle θ_0 of 37° for cloud A and 26° for cloud B is used according to the solar position during the measurements.~~ .

4.4 Vertical weighting function

The vertical photon transport depends on the absorption characteristics at the considered wavelengths. With increasing absorption the probability of a photon being scattered back out of the cloud without being absorbed decreases. Thus, utilizing different near-infrared wavelengths with different absorption characteristics in the retrieval will result r_{eff} from different altitudes in the cloud (King et al., 2013). To quantify this effect, the vertical weighting function w_{m} is investigated. The w_{m} describes the contribution of each cloud layer to the absorption considering multiple scattering (Platnick, 2000). Therefore, it can be used to characterize the cloud level where the retrieved r_{eff} is most representative. For nadir observation, w_{m} ~~for nadir observation~~as a function of optical thickness τ is expressed by:

$$w_{\mathrm{m}}(\lambda,\tau,\tau_c,\mu_0,r_{\mathrm{eff}}) = \left|\frac{\mathrm{d}I(\lambda,\tau,\mu_0,r_{\mathrm{eff}})}{\mathrm{d}\tau}\right| \cdot \frac{1}{\int_0^{\tau_c}\left|\frac{\mathrm{d}I(\lambda,\tau,\mu_0,r_{\mathrm{eff}})}{\mathrm{d}\tau}\right|} \frac{1}{\int_0^{\tau_c}\left|\frac{\mathrm{d}I(\lambda,\tau,\mu_0,r_{\mathrm{eff}})}{\mathrm{d}\tau}\right|\mathrm{d}\tau}, \tag{5}$$

I is the radiance above the cloud and τ_{c} is the total cloud optical thickness. Platnick (2000) showed that w_{m} can be used to estimate the retrieved value of effective radius $r^*_{\mathrm{eff,w}}$ (so-called weighting-estimate) from a given profile of $r_{\mathrm{eff}}(\tau)$ by:

$$r^*_{\mathrm{eff,w}}(\lambda,\tau_c,\mu_0,r_{\mathrm{eff}}) = \int_0^{\tau_c} w_{\mathrm{m}}(\lambda,\tau,\tau_c,\mu_0,r_{\mathrm{eff}})\, r_{\mathrm{eff}}(\tau)\,\mathrm{d}\tau\,, \tag{6}$$

w_{m} calculated for ~~of~~ cloud A and B are shown in Fig. 10c and 10d, respectively. For cloud A with τ_{c} = 3, it is found that w_{m} for λ = 1240 nm and 1640 nm are almost homogeneously distributed along the entire profile. Each cloud layer has nearly equal contribution to the absorption, and therefore to the retrieved r_{eff}. Whereas for cloud B with τ_{c} = 15, the upper cloud layers contribute most to the absorption. ~~Consequently, they strongly influence the retrieved r_{eff}. For both~~ w_{m} profiles ~~, the peak~~ for cloud A and B show, that for λ = 1640 nm the maximum is found closer to the cloud top, while for λ = 1240 nm ~~the peak lies deeper in the cloud~~it is located in a deeper layer. This illustrates, that a retrieval of r_{eff} using λ = 1640 nm ~~results in a~~ will result in an r_{eff} ~~which~~ that represents particle sizes located ~~in~~ at a higher altitude compared to λ = 1240 nm. For the two idealized cloud cases (cloud A and B), this would in general lead to $r_{\mathrm{eff},1640} < r_{\mathrm{eff},1240}$. Additionally, the results ~~from both cases~~ show clearly that each cloud layer has a contribution to the absorption. Therefore, it should be noted that ~~retrieved~~ r_{eff} ~~from~~ retrieved by this remote sensing technique does not represent ~~an effective radius~~ a particle size at a single cloud layer only.

Fig. 11a shows the spectral w_{m} calculated for cloud A ~~(cirrus) in the wavelength range~~ at λ between 1000 - 2000 nm, while Fig. 11b ~~displays~~ is the single scattering albedo ~~ω_{o} of ice particles (GHM)~~ $\tilde{\omega}_0$ of GHM with r_{eff} of 10 µm and 15 µm. The ~~ω_{o}~~ $\tilde{\omega}_0$ strongly depends on r_{eff} and describes the degree of absorption by cloud particles at each individual wavelength~~by cloud particles. The ω_{o}~~ . The $\tilde{\omega}_0$ is smaller for larger particles, and therefore the absorption is higher. The spectral w_{m} at each individual cloud layer clearly shows a wavelength dependence. ~~At a wavelength where ω_{o} is small, and therefore the absorption is high , the peak~~ For a wavelength with smaller $\tilde{\omega}_0$ (high absorption by cloud particles), the maximum of w_{m} ~~lies~~ is located

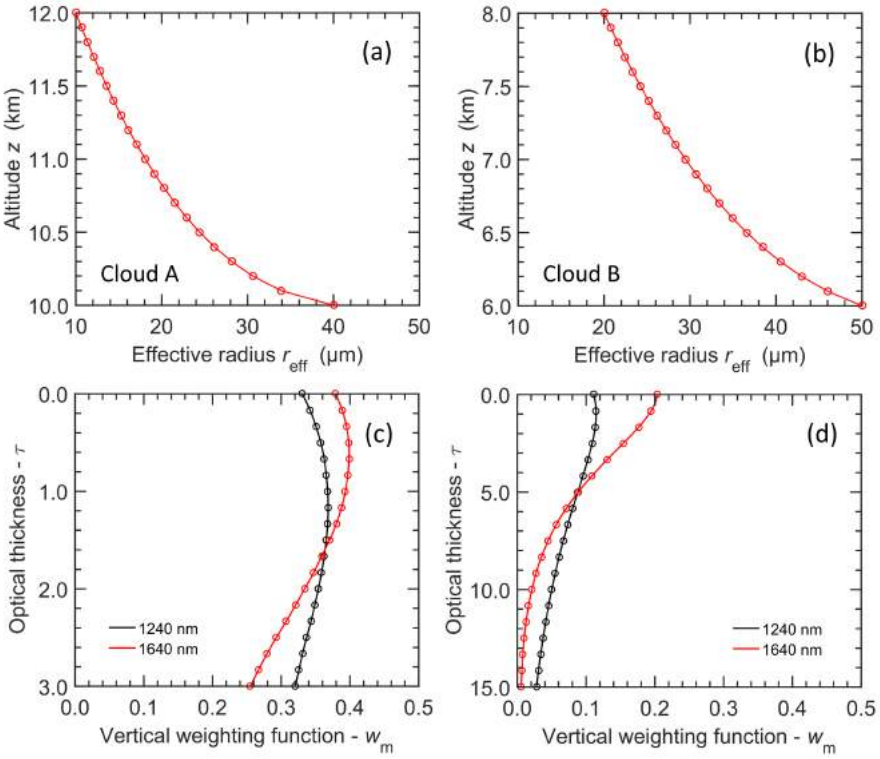

Figure 10. (a) is an analytic effective radius profile of a cirrus (cloud A) while (b) is for a DCC composed of ice particles only (cloud B). Detailed specifications of the two analytic profiles are summarized in Table 3. (c) is w_{m} calculated for cloud A while (d) is for cloud B.

closer to the cloud top. In contrast, for a wavelength with ~~ω_o~~ $\tilde{\omega}_0 \approx 1$ (small absorption ~~),~~ by cloud particles), the w_{m} in the lower layers significantly increases ~~while~~ and the maximum w_{m} is reduced correspondingly. The spectral w_{m} also shows that spectral measurements in the near-infrared wavelengths ~~affords~~ offers more information on the particle sizes located in different cloud altitudes.

~~(a) Spectral vertical weighting function calculated for cloud A (cirrus) in Fig. 10a. (b) Single scattering albedo ω_o of ice particles with an effective radius of 10 m (dashed line) and 15 m (solid line) using the general habit mixture particle (GHM) by Baum et al. (2007).~~

It is found, that w_{m} is a function of the cloud profile itself. Assuming a vertically homogeneous profile in the forward simulation will result in different w_{m} compared to assuming a realistic profile. ~~Consequently, this~~ This may lead to discrepancies in the ~~retrieved cloud properties between~~ r_{eff} retrieved using both assumptions. With the help of w_{m}, possible impacts are investigated by comparing the weighting-estimate $r^*_{\mathrm{eff,w}}$ and the retrieved ~~effective radius~~ $r_{\mathrm{eff,ret}}$ using $\lambda = 1240$ nm and 1640 nm. Radiances above cloud A and B calculated for the entire cloud layer $I^{\uparrow}_{\lambda,\tau_c}$, as described in Section 4.3, serve as synthetic measurements for the radiance ratio retrieval. ~~Two~~ Both combinations, C1 (1240 nm) and C2 (1640 nm), are employed. The resulting $r^*_{\mathrm{eff,w}}$ and $r_{\mathrm{eff,ret}}$ are summarized in Table 3. The ~~results from both approaches show, that the r_{eff} derived using $\lambda = 1640$ nm is~~

~~consistently smaller than using λ = 1240 nm, which agree with the expectation in such conditions where the particle size decreases toward the cloud top. The~~ absolute deviation between $r_{\mathrm{eff,ret,1240}}$ and $r^{*}_{\mathrm{eff,w,1240}}$ is ~~0.5~~ 0.4 µm for ~~both~~ cloud A and ~~B. While between~~ 0.5 µm for cloud B. Between $r_{\mathrm{eff,ret,1640}}$ and $r^{*}_{\mathrm{eff,w,1640}}$, the absolute deviation is 0.4 µm for cloud A and 0.1 µm for cloud B. The r_{eff} retrieved by using measurements at λ = 1640 nm is consistently smaller than λ = 1240 nm, which agree with a condition where the particle size decreases towards the cloud top.

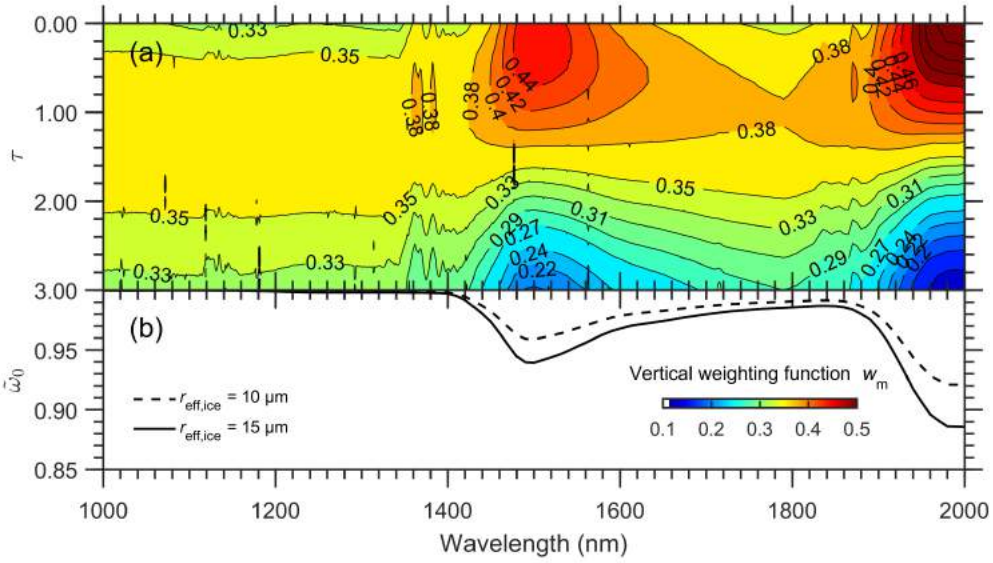

Figure 11. (a) Spectral vertical weighting function calculated for cloud A. (b) Single scattering albedo $\tilde{\omega}_0$ of GHM (Baum et al., 2014) with r_{eff} = 10 µm (dashed line) and 15 µm (solid line).

The comparisons between $r^{*}_{\mathrm{eff,w}}$ and $r_{\mathrm{eff,ret}}$ for cloud A and B yield a systematic deviation. It is found, that retrievals using a vertically homogeneous assumption result in ~~an~~ a slight underestimation of $r_{\mathrm{eff,ret}}$ compared to $r^{*}_{\mathrm{eff,w}}$ which assumes a realistic cloud profile with decreasing particle size towards the cloud top. For the two realistic profiles (cloud A and B), ~~large particles which have~~ larger particles with higher absorption are located in the lower layers. Consequently, w_{m} in the lower cloud layers becomes higher, while w_{m} ~~for~~ in the upper cloud layers is slightly smaller compared to a vertically homogeneous cloud profile (not shown here). ~~However, the~~ The impact of vertical profile assumption will decrease for retrievals using wavelengths with higher absorption by cloud particles such as λ = 1640 nm.

4.5 ~~Heterogeneity~~ Impact of underlying liquid water cloud on the ~~surface albedo~~vertical weighting function

~~The accuracy of the surface albedo assumed in the forward simulations influences the uncertainty of the retrieved cloud properties (Rolland and Liou, 2001; Fricke et al., 2014; Ehrlich et al., 2017). For vertically homogenous clouds, these studies found uncertainties of up to 83 % and 62 % in the retrieved values of τ and r_{eff}, respectively, when an inaccurate surface albedo is assumed in the forward simulation. In the tropical rainforest, such as observed during the ACRIDICON-CHUVA campaign,~~

the heterogeneity of the surface albedo can be high where forested and deforested areas are located close to each other. Fig. **??**a shows a photo of Amazonian surface taken from HALO during the campaign. Several surface types are classified in a small scale area such as (1) forest, (2) dry-land, (3) water body, and (4) wet-land associated with different surface albedos. For airborne measurements over this area, this can lead to sudden changes of the surface albedo along the flight path. Therefore, a representative assumption of homogeneous surface for the whole flight leg is not appropriate.

(a) Picture of Amazonian surface taken during the ARIDICON-CHUVA campaign. Four surface types are classified such as (1) forest, (2) dry-land, (3) water body, and (4) wet-land. (b) w_{m} at λ = 1240 nm (black) and 1640 nm (red) calculated using two spectral surface albedos ρ_{λ} assumed in the forward simulation. $\rho_{\mathrm{S},\lambda}$ is measured by SMART (dashed line), while $\rho_{\mathrm{M},\lambda}$ is derived from the MODIS BRDF/Albedo product (solid line).

Satellite remote sensing is the most practical way to consistently map the surface albedo (Peng et al., 2017). Therefore, for retrievals of DCC over Amazon, the MODIS BRDF/Albedo product is used. Both MODIS-Terra and MODIS-Aqua are used to generate this product in 500 meter resolution. It combines registered, multi-date, multi-band, atmospherically corrected surface reflectance data from the MODIS and MISR instruments to fit a Bidirectional Reflectance Distribution Function (BRDF) in seven spectral bands consisting of three visible bands centered at λ = 460 nm, 555 nm, and 645 nm, and four near-infrared bands centered at λ = 865 nm, 1240 nm, 1640 nm, and 2130 nm (Strahler et al., 1999). The spectral surface albedo derived from the MODIS BRDF/albedo product $\rho_{\mathrm{M},\lambda}$ centered at λ = 645 nm (a), 1240 nm (b), and 1640 nm (b) are shown in Fig. **??**. The values of $\rho_{\mathrm{M},\lambda}$ indicate that the observed DCC was situated above a heterogeneous vegetation surface.

Spectral surface albedo derived from the MODIS BRDF/Albedo product $\rho_{\mathrm{M},\lambda}$ centered at λ = 645 nm (a), 1240 nm (b), and 1640 nm (c). The red arrow indicates HALO flight legs from point A to B during the DCC measurements.

The impact of different surface albedo assumptions on the vertical weighting function w_{m} is investigated. Cloud B specified in Table 3 is chosen for the calculations to represent an anvil of DCC situated over a heterogeneous rainforest surface. w_{m} are calculated for two spectral surface albedos ρ_{λ} assumed in the forward simulation. First, a spectral surface albedo of forest was measured by SMART $\rho_{\mathrm{S},\lambda}$ during the ACRIDICON-CHUVA campaign, which results in $\rho_{\mathrm{S},645}$ = 0.04, $\rho_{\mathrm{S},1240}$ = 0.30, and $\rho_{\mathrm{S},1640}$ = 0.12. Second, a spectral surface albedo is derived from the MODIS BRDF/Albedo product $\rho_{\mathrm{M},\lambda}$. For this purpose, $\rho_{\mathrm{M},\lambda}$ is averaged along HALO flight legs during the DCC measurements, which results in $\rho_{\mathrm{M},645}$ = 0.06, $\rho_{\mathrm{M},1240}$ = 0.21, and $\rho_{\mathrm{M},1640}$ = 0.15. Fig. **??**b shows w_{m} at λ = 1240 nm (black) and 1640 nm (red) calculated for both ρ_{λ}. The dashed line describes w_{m} calculated for $\rho_{\mathrm{S},\lambda}$, while the solid line is for $\rho_{\mathrm{M},\lambda}$. The result shows, that the impact for λ = 1640 nm is negligible because radiation is stronger absorbed by cloud particles and not transmitted to the surface and back. Whereas, changes in ρ_{λ} slightly shift w_{m} at λ = 1240 nm where sufficient radiation is transmitted through the cloud and can interact with the surface. In general, the maximum weighting at cloud top is reduced and shifted to lower altitude when ρ_{λ} is increased. Furthermore, the lower cloud layers are now weighted higher due to the enhanced reflection of transmitted radiation back to the cloud base eventually reaching the sensor above cloud top. For higher ρ_{λ}, even if the correct ρ_{λ} has been considered, the retrieved r_{eff} is located lower because the w_{m} is smaller towards cloud top. Therefore, for cloud B with decreasing particle size towards cloud top, assuming a higher ρ_{λ} will result in a larger retrieved r_{eff} than for assuming a smaller ρ_{λ}. The opposite result is expected for clouds where the particle size decreases toward the cloud top, e.g. adiabatic liquid water clouds.

4.6 ~~Impact of underlying liquid water cloud~~

The changes of the vertical weighting function w_m due to the presence of liquid water ~~cloud~~ clouds below cloud A and B are investigated. Therefore, the calculations of w_m for cloud A and B presented in Section 4.4 are repeated by adding a liquid ~~layer cloud in the radiative transfer simulations~~water cloud layer. For cloud A, the liquid water cloud is located between 1.5 - 2 km with τ = 8 and r_{eff} = 10 µm~~according to the cloud properties observed during the cirrus case~~, which represent a cirrus above a low liquid water cloud. For cloud B, the liquid water cloud is located between 5 ~~–~~and 6 km with τ = 15 and r_{eff} = 15 µm, which represents a DCC topped by an anvil ~~of ice particles, while~~ cirrus, where the lower core of DCC is assumed to be ~~liquid water particles only~~a liquid water cloud. For simplification, the profiles of liquid water cloud are assumed to be vertically homogeneous. For comparison, w_m are calculated and normalized for the ice cloud only. Fig. 12a and 12b show w_m at λ = 1240 nm (black) and 1640 (red) nm calculated for cloud A and cloud B in a condition with (solid line) and without (dashed line) the presence of the liquid water cloud. Additionally, the single scattering albedo ~~ω_0 of ice~~ $\tilde{\omega}_0$ of GHM (blue) and liquid ~~water~~ droplets (red) ~~particles~~ with r_{eff} of 10 µm (dashed line) and 15 µm (solid line) is displayed in Fig. 12c.

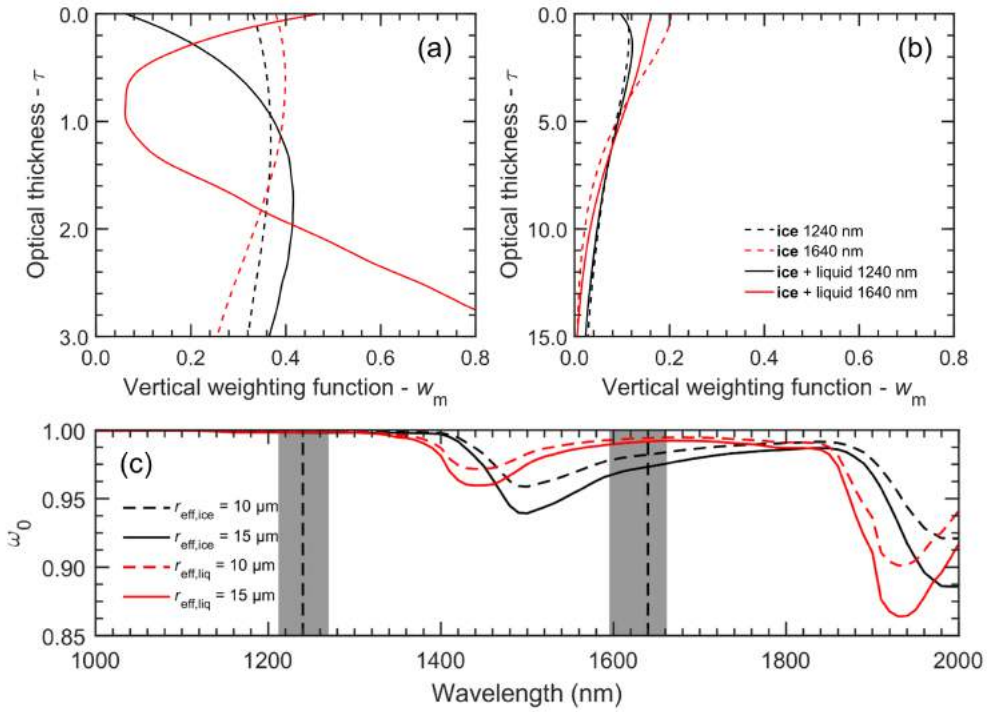

Figure 12. (a) is w_m at λ = 1240 nm and 1640 nm calculated for cloud A, while (b) is for cloud B. Solid line and dashed line describe w_m calculated with and without the presence of underlying liquid water cloud, respectively. (c) ~~is single~~ Single scattering albedo ~~ω_0~~ $\tilde{\omega}_0$ of ~~ice (~~GHM ~~)~~ and liquid water ~~particle~~ droplets with r_{eff} of 10 µm and 15 µm.

~~In general~~According to Platnick (2000), it is expected that ~~a~~ the low liquid water cloud changes w_m similar to a bright surface~~as described in Section ??, where it reflects solar radiation stronger than a dark surface such as water and forest.~~ , where the maximum weighting at cloud top will be reduced and shifted to a lower altitude due to the enhanced reflection of transmitted radiation back to the cloud base eventually reaching the sensor above cloud top. Consequently, this will result in a larger retrieved r_{eff} for clouds with decreasing particle size towards cloud top. The results in Fig. 12a and 12b show, that this indeed holds for the w_m at $\lambda = 1240$ nm where scattering by cloud particles dominates. ~~In both clouds~~ For cloud A and B, the maximum of w_m is shifted to lower altitudes due to multiple ~~reflection~~ reflections of radiation between ~~surface~~ the surface (liquid water cloud) and cloud base ~~. As a consequence, this will result in an increase of the retrieved r_{eff}. However, for~~ (ice cloud). The w_m at $\lambda = 1640$ nm ~~w_m~~ changes differently when adding a liquid water cloud below the ice cloud. The changes of w_m for cloud A are significantly larger compared to cloud B. This ~~pattern~~ behavior results from the stronger absorption by the ice particles at $\lambda = 1640$ nm. ~~The~~ For optically thick cloud B with $\tau_c = 15$, the ice cloud does not transmit sufficient radiation to have a strong interaction with the low level cloud ~~,~~ which leads to ~~almost~~ a similar w_m ~~for the optically thick cloud B with $\tau_c = 15$. However,~~ . In contrast, w_m at cloud top is modified for optically thin cloud A with $\tau_c = 3$ ~~, w_m is modified at the cloud top~~ due to the underlying liquid water cloud. Here the different particle phase and size of the liquid water cloud layer lead to a reduction of the upward radiance $I_\lambda^\uparrow$ when an ice cloud layer is added to the simulations. ~~Due to the small liquid water particles with high ω_0~~ Given that small liquid droplets have a higher $\tilde{\omega}_0$ at $\lambda = 1640$ nm, the liquid water cloud alone reflects ~~stronger~~ more strongly than together with the ice cloud which adds large ice crystals characterized by ~~a lower ω_0~~ smaller $\tilde{\omega}_0$ reducing the total ~~reflectivity. This decrease of $I_\lambda^\uparrow$~~. Decreasing $I_\lambda^\uparrow$ strongly contributes to the w_m close to the cloud top, while at about $\tau = 1$ ~~a~~ the minimum of w_m is observed where $I_\lambda^\uparrow$ changes only slightly. Below $\tau = 1$ (lower altitudes), the impact of the liquid water cloud vanishes and scattering by the ice particles increases $I_\lambda^\uparrow$ again corresponding to higher w_m ~~at~~ towards cloud base. In general, a similar ~~pattern~~ behavior is imprinted in the w_m of ~~the optically thick~~ cloud B but not relevant for the entire w_m due to the higher τ_c of the ice cloud. This also demonstrates, that for optically thick clouds ~~, like~~ such as the DCC case investigated in this study, a retrieval assuming ~~ice cloud only~~ only ice cloud can be applied to retrieve r_{eff} of the upper most cloud layer, even if liquid water clouds are present below the ice ~~layer at cloud top~~cloud layer.

4.6 ~~Optical~~ Comparison of optical thickness and effective radius retrieved by SMART and MODIS

Time series of τ and r_{eff} retrieved from SMART and MODIS radiance measurements, ~~as~~ and from the MODIS cloud product are compared for the two cloud cases~~, cirrus and DCC~~. The MODIS cloud product collection 6, namely MYD06_L2~~(Platnick et al., 2003, 20~~ , provides three different r_{eff} ~~which are retrieved using different~~ (so-called $r_{eff,L,1640}$, $r_{eff,L,2130}$, and $r_{eff,L,3700}$) retrieved using three near-infrared wavelengths centered at $\lambda = 1640$ nm, 2130 nm, and 3700 nm ~~(so-called $r_{eff,1640}$, $r_{eff,2130}$, and $r_{eff,3700}$)~~(Platnick et al., 2017). However, the ~~quality of $r_{eff,1640}$ is~~ information of $r_{eff,L,1640}$ is very limited due to problems of the detectors~~of MODIS-Aqua band 6. Therefore, $r_{eff,1640}$ is not considered in the comparison. The spectral radiance~~ , and therefore it cannot be used in this comparison. Due to the similar ice crystal absorption at $\lambda =$ ~~2130 nm and 3700 nmwhich is used for the MODIS cloud product, $r_{eff,2130}$ and $r_{eff,3700}$, are not covered by the SMART measurements for both cloud cases. However, the~~ 1640 nm and 2130 nm, both wavelengths have an almost identical w_m ~~at $\lambda = 2130$ nm is very similar to w_m of~~

~~λ = 1640 nm (not shown here)~~(Wang et al., 2009; Zhang et al., 2010). For typical cloud profiles ~~as~~ analyzed in Section 4.4, the differences of ~~retrieved $r_{\mathrm{eff},2130}$ and $r_{\mathrm{eff},1640}$~~ r_{eff} retrieved using λ = 1640 nm and 2130 nm are less than ~~0.5~~ 1 µm. Therefore, ~~$r_{\mathrm{eff},2130}$ can be employed to compare the MODIS cloud product and the radiance ratio retrieval~~ $r_{\mathrm{eff,L},2130}$ can be compared with SMART and MODIS r_{eff} retrieved using C2 (~~$r_{\mathrm{eff},1640}$~~1640 nm). For observations over land, the MODIS algorithm combines the reflectivity at λ = 645 nm and 2130 nm (~~C3 -~~ combination 3 ~~) to retrieve τ and $r_{\mathrm{eff},2130}$, respectively~~ - C3). While over ocean, it combines the reflectivity at λ = 858 nm and 2130 nm (~~C4 -~~ combination 4 ~~) to retrieve the respective cloud properties~~ - C4).

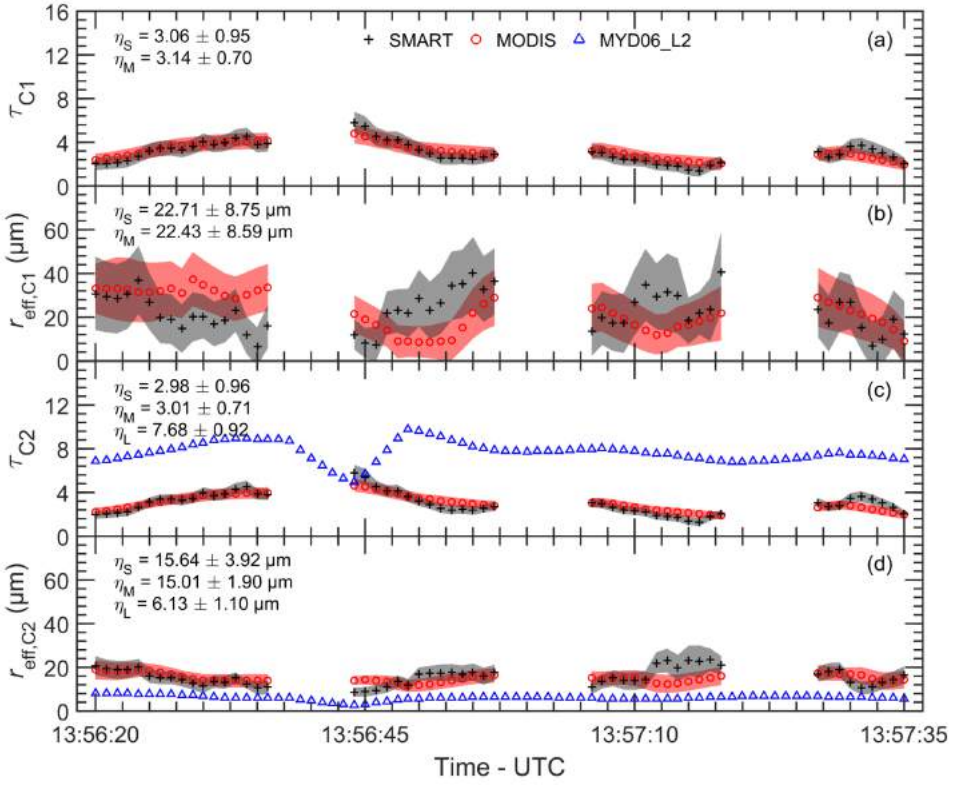

Figure 13. Time series of cirrus τ (a) and r_{eff} (b) retrieved from SMART (black) and MODIS (red) using combination 1 (C1). The dark shaded area describes retrieval uncertainties. η_S (SMART) and η_M (MODIS) represent the mean ± standard deviation along time series. (c) and (d) are the respective properties retrieved using combination 2 (C2). Cloud properties derived from the MODIS cloud product (MYD06_L2), τ_L and $r_{\mathrm{eff,L},2130}$, are shown in blue (only in panel c and d) with the corresponding η_L.

Time series of cirrus optical thickness and effective radius retrieved using C1, $\tau_{\mathrm{ci,C1}}$ and $r_{\mathrm{eff,ci,C1}}$, are presented in Fig. 13a and 13b, respectively. ~~Note that the corrected $I^{\uparrow}_{\mathrm{M},1240}$ by Eq. ?? have applied in the MODIS radiance ratio retrieval.~~ The η describes the mean ± standard deviation of the corresponding cloud properties along the selected time series with ~~a~~ the subscript of "S" for SMART and "M" for MODIS. To quantify the agreement of the retrieved cirrus properties based on

SMART and MODIS, the normalized mean absolute deviation ζ is calculated. A $\zeta_{\tau_{\mathrm{ci,C1}}}$ of ~~0.7 %~~ 1.2 % and a $\zeta_{r_{\mathrm{eff,ci,C1}}}$ of ~~2.5 % is~~ 0.7 % are obtained. Fig. 13c and 13d show time series of cirrus optical thickness and effective radius retrieved using C2, $\tau_{\mathrm{ci,C2}}$ and $r_{\mathrm{eff,ci,C2}}$, respectively. A $\zeta_{\tau_{\mathrm{ci,C2}}}$ of 0.5 % and a $\zeta_{r_{\mathrm{eff,ci,C2}}}$ of ~~2.3 %~~ 2.1 % are obtained. The analysis shows, that deviations between SMART and MODIS in the retrieved cloud properties are only slightly enhanced by the non-linearity in the retrieval algorithm. ~~Cloud~~ Additionally, cloud properties derived from ~~MYD06_L2~~ the MODIS cloud product (blue) are also shown in Fig. 13c and 13d, where η with ~~a~~ the subscript of "L" describes the respective mean $\pm$ standard deviation along the selected time series.

~~Time series of cirrus τ (a) and r_{eff} (b) retrieved from SMART (black) and MODIS (red) using combination 1 (C1). Dark shaded area describes retrieval uncertainties. η_{S} (SMART) and η_{M} (MODIS) represent the mean $\pm$ standard deviation along time series. (c) and (d) are the respective properties retrieved using combination 2 (C2). Cloud products derived from MYD06_L2, τ and $r_{\mathrm{eff,2130}}$, are shown in blue (only in panel c and d). η_{L} represents the mean $\pm$ standard deviation of the derived properties from MYD06_L2 along time series.~~

~~Retrieved cirrus properties~~ Cirrus properties retrieved using combinations C1 and C2 are compared to the MODIS cloud product (combination C4). Along the selected time series, all combinations show that τ_{ci} is homogeneous ~~in the observed area, which is~~ indicated by the small ~~values of~~ standard deviation $\sigma_{\tau_{\mathrm{ci}}}$ ~~only of up to~~ $<$ 1. However, it is found that ~~$\overline{\tau}_{\mathrm{ci,C4}}$~~ $\overline{\tau}_{\mathrm{ci,L,C4}}$ derived from the MODIS cloud product ~~yields a significant overestimation~~ significantly overestimates $\overline{\tau}_{\mathrm{ci,C2}}$ (see Fig. 13c). The absolute deviation between the mean ~~$\overline{\tau}_{\mathrm{ci,C4}}$~~ value $\overline{\tau}_{\mathrm{ci,L,C4}}$ and $\overline{\tau}_{\mathrm{ci,C2}}$ is found up to 4.7 ~~or nearly~~ (160 % ~~. In relative difference). For~~ the MODIS cloud product, the retrieval is ~~performed with an assumption of single layer cloud even if multilayer clouds are reported (Platnick et al., 2017). However, the~~ always performed with the assumption of a single cloud layer even if a multilayer condition is detected (Platnick et al., 2017). Omitting the low liquid water cloud ~~underlying cirrus increases the reflected upward radiances in the visible wavelengths (Finger et al., 2016). Assuming a single layer cloud in the retrieval~~ consequently results in a ~~large overestimation on~~ significant overestimation of the retrieved τ_{ci} ~~because the increase of reflectivity is considered to result from the cirrus alone~~. Including a low ~~level~~ liquid water cloud ~~as~~ in the radiance ratio retrieval as applied to SMART and MODIS, more realistic τ_{ci} are obtained. Furthermore, ~~it is found that the dependency between retrievals of τ and r_{eff} leads to a small difference~~ small differences between $\tau_{\mathrm{ci,C1}}$ and $\tau_{\mathrm{ci,C2}}$ ~~. Fig. 8 shows, that the lookup tables of τ tilt to the right. Consequently, for a larger value of r_{eff}, it will result in a larger value of τ. While for a smaller value of r_{eff}, it will result in a smaller value of τ.~~ are found. For a cirrus cloud where the particle size decreases ~~toward the~~ towards cloud top, it is expected that $r_{\mathrm{eff,C1}} > r_{\mathrm{eff,C2}}$. ~~This finally leads to higher optical thickness retrieved by the combination C1, $\overline{\tau}_{\mathrm{ci,C1}} > \overline{\tau}_{\mathrm{ci,C2}}$~~ Due to the remaining coupling between τ and r_{eff} (non-orthogonal radiance lookup tables), these differences propagate into the retrieved τ, and lead to $\tau_{\mathrm{C1}} > \tau_{\mathrm{ci,C2}}$.

~~Same as Fig. 13 but for the DCC.~~

The results from all approaches show that the mean $\overline{r}_{\mathrm{eff,ci,C1}} > \overline{r}_{\mathrm{eff,ci,C2}} > \overline{r}_{\mathrm{eff,ci,C4}}$. ~~By neglecting~~ It should be noted, that due to omitting the underlying liquid water cloud ~~which is characterized by small liquid water particles,~~ $\overline{r}_{\mathrm{eff,ci,C4}}$ underestimates the ~~particle size of the cirrus cloud~~actual value. The difference between $r_{\mathrm{eff,C1}}$ and $r_{\mathrm{eff,C2}}$ results from the different w_{m} as discussed in Section 4.4, ~~the w_{m} of λ = 1640 nm is shifted towards cloud top compared to λ = 1240 nm and this causes~~ which makes

$r_{\mathrm{eff,C1}} > r_{\mathrm{eff,C2}}$ for a cirrus with decreasing particle size towards cloud top. Additionally, the results show that the standard deviation $\sigma_{\mathrm{r_{eff,ci,C1}}} > \sigma_{\mathrm{r_{eff,ci,C2}}} > \sigma_{\mathrm{r_{eff,ci,C4}}}$. This ~~phenomena indicatesthat more homogeneous particle sizes lie in the higher cloud layers, while mixture particle sizes are located in~~ indicates, that the horizontal variability of ice crystals is higher in lower cloud layers~~due to size sorting and the increased fall speeds of larger particles in ice clouds (van Diedenhoven et al., 2016).~~ ~~Smaller~~, while close to cloud top the ice crystals are distributed more homogeneously along the flight legs. Smaller ice particles with low ~~sedimentation velocity remain in~~ sedimenting velocity remain at the higher altitudes, while larger ice particles with faster ~~sedimentation~~ sedimenting velocity drop into the cloud layers below. ~~The results also show, that~~ This sedimentation is horizontally inhomogeneous due to the variability of the vertical wind velocity and leads to a size sorting and the observed horizontal variability of the particle sizes. The analysis shows, that the uncertainty $\Delta r_{\mathrm{eff,ci,C1}} > \Delta r_{\mathrm{eff,ci,C2}}$~~, which confirms~~. This confirms, that retrievals of r_{eff} using a wavelength with a smaller absorption by cloud particles will result in a ~~higher~~ larger uncertainty. Additionally, it is found that increasing τ and r_{eff} has a positive correlation with increasing $\Delta\tau$ and Δr_{eff}~~.~~ ~~This~~, which is due to decreasing sensitivity in the radiance lookup tables for larger τ and r_{eff}.

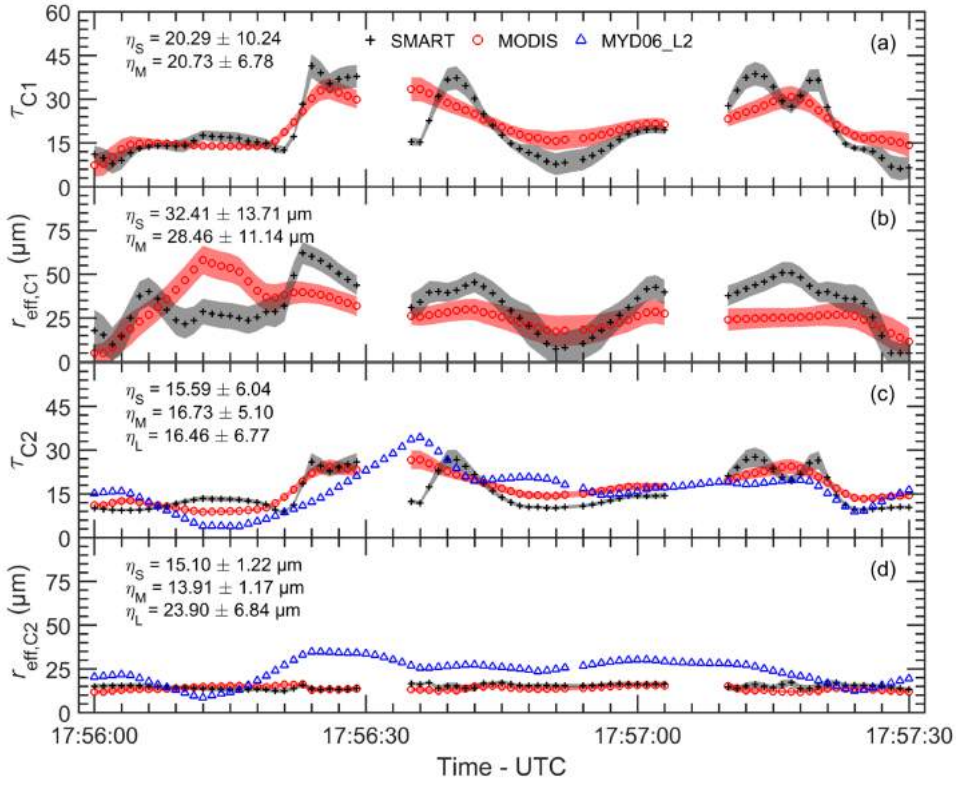

Figure 14. Same as Fig. 13 but for the DCC case.

Time series of DCC optical thickness and effective radius retrieved using C1, $\tau_{\mathrm{dcc,C1}}$ and $r_{\mathrm{eff,dcc,C1}}$, are shown in Fig. 14a and 14b, respectively. ~~The resulting~~ A $\zeta_{\tau_{\mathrm{dcc,C1}}}$ of ~~5.1 % and~~ 1.1 % and a $\zeta_{\mathrm{r_{eff,dcc,C1}}}$ of ~~17.5 % are obtained~~ 6.5 % are obtained between

SMART and MODIS retrievals. Compared to the cirrus case, the larger ~~value of $\zeta_{r_{\mathrm{eff,dcc,C1}}}$~~ horizontal variability indicates a strong ~~microphysical properties evolution~~ evolution of microphysical properties in the deeper layer of DCC. Fig. 14c and Fig. 14d show time series of DCC optical thickness and effective radius retrieved using C2, $\tau_{\mathrm{dcc,C2}}$ and $r_{\mathrm{eff,dcc,C2}}$. A $\zeta_{\tau_{\mathrm{dcc,C2}}}$ of ~~6.1 %~~ 3.5 % and a $\zeta_{r_{\mathrm{eff,dcc,C2}}}$ of ~~2.6 % are obtained~~ 4.1 % are obtained in this case. In addition ~~of~~ to the fast cloud evolution, larger 3-D radiative effects are likely influencing the observations, which can enhance the deviations of ~~the~~ retrieved cloud properties~~between SMART and MODIS~~. The cloud properties derived from ~~MYD06_L2~~ the MODIS cloud product (blue) are also presented in Fig. 14c and 14d. ~~For this case , the MYD06_L2~~ In this case (over land), the MODIS cloud product algorithm uses C3~~(over land). The standard deviation values~~ . The high values of standard deviation $\sigma_{\tau_{\mathrm{dcc}}}$ from approach C1, C2, and C3, which are up to ~~11.1~~10.3, indicate that τ_{dcc} is heterogeneous except in the anvil region. The DCC anvil ~~(noticed as cirrus) is detected~~ is observed between 17:56:00 - 17:56:20 UTC~~and~~ , which is characterized by relatively smaller τ between 8 - ~~20.~~ 15. Later, τ_{dcc} increases sharply corresponding to the DCC core and decreases again ~~toward~~ towards the cloud edge. ~~Looking at each instrument, it is found that~~ The mean value $\overline{r}_{\mathrm{eff,dcc,C1}} > \overline{r}_{\mathrm{eff,dcc,C2}}$ ~~$> \overline{r}_{\mathrm{eff,dcc,C4}}$. This indicates , that the particle size in the DCC also decreases toward the~~ indicates decreasing particle size towards cloud top. ~~Additionally, it is foundthat~~ It is found, that $\overline{r}_{\mathrm{eff,dcc,C3}}$ is larger than $\overline{r}_{\mathrm{eff,dcc,C2}}$ corresponding to the different assumptions of the ice crystal habit of plate (SMART and MODIS retrievals) and aggregated columns (MODIS cloud product). Given that $\sigma_{r_{\mathrm{eff,dcc,C1}}} > \sigma_{r_{\mathrm{eff,dcc,C2}}}$ and $\sigma_{r_{\mathrm{eff,dcc,C2}}} < \sigma_{r_{\mathrm{eff,dcc,C2}}}$ ~~. This condition yields,~~ , this illustrates that the particle sizes are more homogeneous in the level of $r_{\mathrm{eff,dcc,C2}}$ compared to the level of $r_{\mathrm{eff,dcc,C1}}$ ~~(lower cloud layer)~~ and $r_{\mathrm{eff,dcc,C3}}$~~(higher cloud layer)~~.

5 Comparison of retrieval results with in situ ~~measurement~~measurements for the cirrus case

The retrieved ~~effective radius is compared to the in situ effective radius~~ and in situ r_{eff} are compared for the cirrus case. Here, the terminology of ~~$r_{\mathrm{eff,z}}$~~ $r_{\mathrm{eff}}(z)$ is used to describe the ~~in situ~~ particle effective radius sampled at a specific vertical layer z, while the ~~effective radius retrieved using a remote sensing technique~~ retrieved r_{eff} represents a bulk ~~value. The number size distribution measured by the CCP has been converted into the particle effective radius with~~ property of the entire cloud as discussed in Section 4.4. The CCP provides $r_{\mathrm{eff}}(z)$ at 1 Hz temporal resolution~~(Weigel et al., 2016). A binning method is applied to gain the profile of cirrus effective radius with a 20 m vertical resolution~~ . These data are averaged to derive $r_{\mathrm{eff}}(z)$ with a vertical resolution of 65 m. Fig. 15a shows, that the CCP detected a cirrus ~~cloud~~ between 10.7 and 12 km ~~, where~~ with the mean values (solid line) ~~range~~ ranging between 3 - 30 µm. The ~~shaded area illustrates measurement~~ grey area illustrates the estimated uncertainties of the in situ ~~observations~~data. The smallest ~~particle~~ particles with r_{eff} = 3.1 µm ~~is~~ are found at the cloud base z_{b} = 10.7 km and ~~increases~~ grow rapidly up to 30.2 µm at z = 10.8 km. Later, r_{eff} decreases reaching a value of 8.4 µm at the cloud top z_{b} = 11.97 km.

To compare ~~in situ and retrieved effective radius~~retrieved and in situ r_{eff}, the vertical weighting function w_{m} has to be considered. A ~~comparison~~ direct comparison between r_{eff} and $r_{\mathrm{eff}}(z)$ at a single layer is ~~not appropriate because each individual cloud layer contributes to the absorption, as discussed in Section 4.4. The~~ inappropriate because both are defined differently. Note that the w_{m} ~~is calculated using the profile of effective radius $r_{\mathrm{eff,z}}$ and ice water content (IWC) measured by~~ in this study

is calculated in terms of τ increasing from cloud top towards cloud base. Therefore, the conversion of geometrical altitude and optical thickness $\tau(z)$ has to be specified and considered in the analysis. For this purpose, IWC(z) measured by WARAN and $r_{\mathrm{eff}}(z)$ derived from CCP are converted into a profile of the extinction coefficient $\beta(z)$ following the scheme introduced by introduced by Fu and Liou (1993) and Wang et al. (2009):

$$\beta_{\mathrm{e}}(z) \approx \mathrm{IWC}(z) \cdot \left[a + \frac{b}{r_{\mathrm{eff}}(z)}\right], \tag{7}$$

where $a = -6.656 \times 10^{-3}$, $b = 3.686$. $\beta_{\mathrm{e}}(z)$ is in the unit of m^{-1}, IWC(z) in ~~situ instruments. Furthermore, the profile of effective radius $r_{\mathrm{eff,z}}$ is~~ $\mathrm{g\ m}^{-3}$, and $r_{\mathrm{eff}}(z)$ in µm. Further, the extinction profile is used to calculate $\tau(z)$ by integrating $\beta_{\mathrm{e}}(z)$ from cloud top to the altitude level z:

$$\tau(z) = \int_{z}^{z_t} \beta_{\mathrm{e}}(z)\, \mathrm{d}z\,, \tag{8}$$

Using $\tau(z)$, $r_{\mathrm{eff}}(z)$ can be converted into $r_{\mathrm{eff}}(\tau)$. To calculate the w_{m}, the cloud is divided into 20 inhomogeneous layers, where each cloud layer is assigned to a $r_{\mathrm{eff}}(\tau)$. Finally, the $r_{\mathrm{eff}}(\tau)$ is convoluted with the w_{m} to calculate the in situ weighting-estimate $r^*_{\mathrm{eff,w}}$ ~~using~~ given by Eq. 6 to allow a comparison with the retrieved ~~effective radius~~ r_{eff}. Similarly, the weighting-altitude z^*_{w} ~~,~~which characterizes the altitude ~~of weighting-estimate and retrieved effective radius~~ corresponding to the $r^*_{\mathrm{eff,w}}$ and the retrieved r_{eff} can be calculated by:

$$z^*_{\mathrm{w}}(\lambda, \tau_c, \mu_0, r_{\mathrm{eff}}) = \int_{0}^{\tau_c} w_{\mathrm{m}}(\lambda, \tau, \tau_c, \mu_0, r_{\mathrm{eff}})\, z(\tau)\, \mathrm{d}\tau\,, \tag{9}$$

~~where z is the cloud altitudes.~~ Due to different absorption characteristics~~in the wavelength~~, it is expected that z^*_{w} ~~varies~~ will differ for different near-infrared wavelengths~~used in the retrieval~~. The stronger the absorption by cloud particles in the wavelength, the higher the z^*_{w} (closer to cloud top).

The comparison of $r^*_{\mathrm{eff,w}}$ and the mean value of retrieved r_{eff} is presented in Fig. 15b by symbols. Horizontal error bars represent the standard deviation of particle sizes. Vertical error bars indicate the estimated uncertainty of the weighting-altitude of 40 m, which represents the standard deviation of z^*_{w} by varying ice crystal habits in the forward simulations. Additionally, the r_{eff} retrieved using SMART radiance measurements at λ = 1500 nm, 1550 nm, and 1700 nm, and also MODIS radiances centered at λ = 2130 nm and 3700 nm (band 20) are applied in this comparison. The retrieval and the calculation of w_{m} for λ = 3700 nm are performed by considering both solar and thermal radiation. Using these additional wavelengths allows to enhance the vertical resolution of retrieved r_{eff}. Fig. 15b shows, that in situ $r^*_{\mathrm{eff,w}}$ and retrieved r_{eff} agree within the standard deviation for all altitudes and reproduce the decrease of particle size towards the cloud top. However, it is obvious that although retrievals of r_{eff} using multi near-infrared wavelengths result in particle sizes from different cloud altitudes, this passive retrieval technique only provides information of particle size in the cloud top layers. This is because the retrieved r_{eff} represents a vertically weighted value, where cloud the top layers are weighted at most.

Table 4. The mean ± standard deviation η of cirrus effective radius determined by in situ weighting-estimate (CCP) and retrievals (SMART, MODIS, and MYD06_L2) using near-infrared wavelengths between 1240 nm - 3700 nm. The wavelengths have been sorted in order that the degree of absorption by cloud particles increases to the right. z_{w}^{*} is the weighting-altitude.

λ	1240 nm	1700 nm	1640 nm	2130 nm	1550 nm	1500 nm	3700
η_{CCP} (µm)	19.0 ± 9.8	18.3 ± 9.6	18.0 ± 9.5	17.5 ± 9.4	17.0 ± 9.3	16.7 ± 9.3	7.0 ±
η_{SMART} (µm)	~~22.1~~ 22.7 ± ~~8.9~~ 8.8	~~19.7~~ 16.5 ± ~~7.1~~ 6.7	~~14.6~~ 15.6 ± 3.9	-	13.9 ± ~~2.7~~ 3.7	~~14.8~~ 15.7 ± ~~2.7~~ 2.1	-
η_{MODIS} (µm)	~~23.3~~ 22.4 ± ~~9.1~~ 8.6	-	~~13.9~~ 15.0 ± 1.9	~~-~~14.8 ± 4.9	-	-	~~-~~7.2 ±
η_{MYD06} (µm)	-	-	-	~~6.3~~ 6.2 ± 1.2	-	-	4.8 ±
z_{w}^{*} (km)	11.39	11.42	11.44	11.46	11.48	11.49	11.8

~~The comparison of in situ weighting-estimate $r_{\mathrm{eff,w}}^{*}$ and the mean value of retrieved effective radius r_{eff} are presented in Fig. 15b by symbols. Horizontal error bars represent the standard deviation , while vertical error bars are the estimated uncertainty of weighting-altitude $\Delta z_{\mathrm{w}}^{*}$. $\Delta z_{\mathrm{w}}^{*}$ is estimated by the standard deviation of z_{w}^{*} calculated with different ice crystal shapes assumed in the forward simulations, which results in a value of 40 m. Additional r_{eff} retrieved by use of additional wavelengths of SMART at λ = 1500 nm, 1550 nm, and 1700 nm are applied in the comparison. By use of these additional wavelengths of SMART allows to enhance the vertical resolution of~~ Table 4 summarizes the mean ± standard deviation η of in situ $r_{\mathrm{eff,w}}^{*}$ and retrieved r_{eff} ~~. In addition, the MODIS cloud product (MYD06_L2), $r_{\mathrm{eff,2130}}$ and $r_{\mathrm{eff,3700}}$, are also employed in the comparison. The w_{m} for λ = 3700 nm is calculated using solar radiation only and does not account thermal emissivity.~~

~~In general, results from in situ weighting-estimates,~~ from SMART and MODIS~~retrievals, and MODIS cloud products (MYD06_L2) show that the particle size in the observed cirrus decreases toward the cloud top. Additionally, the results also confirm that although retrievals of effective radius using multi near-infrared wavelengths result in particle sizes from different cloud altitudes, this conventional retrieval technique only provides information on the cloud-top effective radius. This is due to the fact, that the retrieved r_{eff} represents a vertically weighted value where cloud top layers are weighted at most, which is in agreement with analyses reported by Chang and Li (2002), Chang and Li (2003), Zhang et al. (2010), King and Vaughan (2012), , King et al. (2013), and van Diedenhoven et al. (2016).~~

~~(a) Profile of effective radius $r_{\mathrm{eff,z}}$ determined from in situ measurements (solid line), while the grey area represents the uncertainties of in situ observations. (b) Comparison of in situ weighting-estimate (CCP) and the mean value of retrieved effective radius (SMART, MODIS, and MYD06) for λ between 1240 nm - 3700 nm. Horizontal error bars represent the standard deviation, while vertical error bars are $\Delta z_{\mathrm{w}}^{*}$. (c) Scatter plot between in situ weighting-estimate and the mean value of retrieved effective radius. The grey line is the one-to-one line, while the labels at each data point describe the wavelength used in the retrievals.~~

~~Table 4 summarizes the mean ± standard deviation η of effective radius from r_{eff} ,~~ and ~~$r_{\mathrm{eff,w}}^{*}$, and the weighting-altitude~~ z_{w}^{*} for ~~multi~~ near-infrared wavelengths between 1240 nm - 3700 nm. Additionally, MODIS cloud products, $r_{\mathrm{eff,L,2130}}$ and

$r_{\mathrm{eff,L,3700}}$ are included in the table for the comparison. To quantify the agreement between in situ ~~weighting-estimate and retrieved effective radius~~$r^*_{\mathrm{eff,w}}$ and retrieved r_{eff}, the normalized mean absolute deviation ζ is calculated. The ~~resulting ζ between the~~ deviations of in situ $r^*_{\mathrm{eff,w}}$ and ~~the mean value of SMART retrievals is 7.6 %, 3.6 %, 10.5 %, 9.9 %, and 6.1 % for $r_{\mathrm{eff,1240}}$, $r_{\mathrm{eff,1700}}$, $r_{\mathrm{eff,1640}}$, $r_{\mathrm{eff,1550}}$, and $r_{\mathrm{eff,1500}}$, respectively. The resulting~~ SMART r_{eff} range between ζ ~~between the~~ = 3.2 % (λ = 1500 nm) and ζ = 10.3 % (λ = 1550 nm). Between $r^*_{\mathrm{eff,w}}$ and ~~the mean value of MODIS retrievals is 10.1 % and 12.7 % for $r_{\mathrm{eff,1240}}$ and $r_{\mathrm{eff,1640}}$, respectively. While between the $r^*_{\mathrm{eff,w}}$ and the mean value of MODIS cloud products (MYD06_L2), the resulting~~ MODIS r_{eff}, the ζ ~~is 47.5 % and 19.3 %~~ results in a value between 1.5 % for λ = 3700 nm and 9.1 % for ~~$r_{\mathrm{eff,2130}}$ and $r_{\mathrm{eff,3700}}$, respectively. The large deviation between $r^*_{\mathrm{eff,w,2130}}$ and~~ λ = 1640 nm. Overall, the values of ζ are in the range between $1.5 - 10.3$ % and agree within the horizontal standard deviation, as shown in Fig. 15b.

The r_{eff} derived from the MODIS cloud product ~~$r_{\mathrm{eff,2130}}$ is due to the presence of~~ are obviously affected by the low liquid water cloud, ~~where the MODIS cloud product does not consider it. However, the influence is almost negligible for $r_{\mathrm{eff,3700}}$ due to strong absorption by cloud particles~~ which is not included in the algorithm of MODIS operational retrieval. Therefore, a ζ of 47.5 % and 19.3 % is obtained for $r_{\mathrm{eff,L,2130}}$ and $r_{\mathrm{eff,L,3700}}$, respectively. The absorption by the ice crystals at λ = 3700 nm ~~. Except the MODIS cloud product $r_{\mathrm{eff,2130}}$, the values of ζ range between $3.6 - 19.3$ %, which agree within the standard deviation.~~

is very strong. Consequently, the first top layers will dominate the absorption and significantly reduce the effect of the underlying liquid water cloud. Fig. 15c shows ~~a scatter plot~~ scatter plots of in situ ~~weighting-estimate and retrieved effective radius. The symbols represent which data is compared to the in situ. The grey~~ $r^*_{\mathrm{eff,w}}$ and r_{eff} retrieved from SMART (black triangles) and MODIS (red dots), while the dashed line represents the one-to-one line. ~~The result shows, that there is only a small correlation between the variation of in situ and retrieved effective radius, which is in agreement with analyses reported by King et al. (2013). The deviation~~ There is a robust agreement between in situ ~~and retrieved effective radius depends on the choice of near-infrared wavelength used in the retrieval algorithm~~$r^*_{\mathrm{eff,w}}$ and retrieved r_{eff} with a correlation coefficient R^2 of 0.82. The variability of particle size distributions~~and the~~, the uncertainties of deriving r_{eff} from the in situ measurements, the presence of liquid water cloud ~~underlying cirrusare considered as potential error contributors. In addition,~~ below cirrus, and the uncertainties caused by the choice of ice crystal shapes for the retrievals are considered as the main contributor to address the ~~simplification in the retrieval forward simulations which assume a vertically homogeneous cloud is also considered to cause the~~ discrepancies between in situ ~~and retrieved effective radius, which is in agreement with the finding discussed in Zhang et al. (2010) and Nagao et al. (2013). This argument is confirmed by the profile of cirrus effective radius measured by in situ, which clearly show in-cloud vertical inhomogeneity, as shown in Fig. 15a. Therefore, a vertically homogeneous assumption in the retrieval forward simulation is not appropriate.~~ $r^*_{\mathrm{eff,w}}$ and retrieved r_{eff}.

6 Conclusions

Accurate solar radiation measurements are necessary to ~~obtain a~~ retrieve high-quality cloud products ~~, e.g., cloud~~ such as optical thickness τ and particle effective radius r_{eff}~~, from satellite remote sensing~~. Small measurement uncertainties propagate ~~and may~~

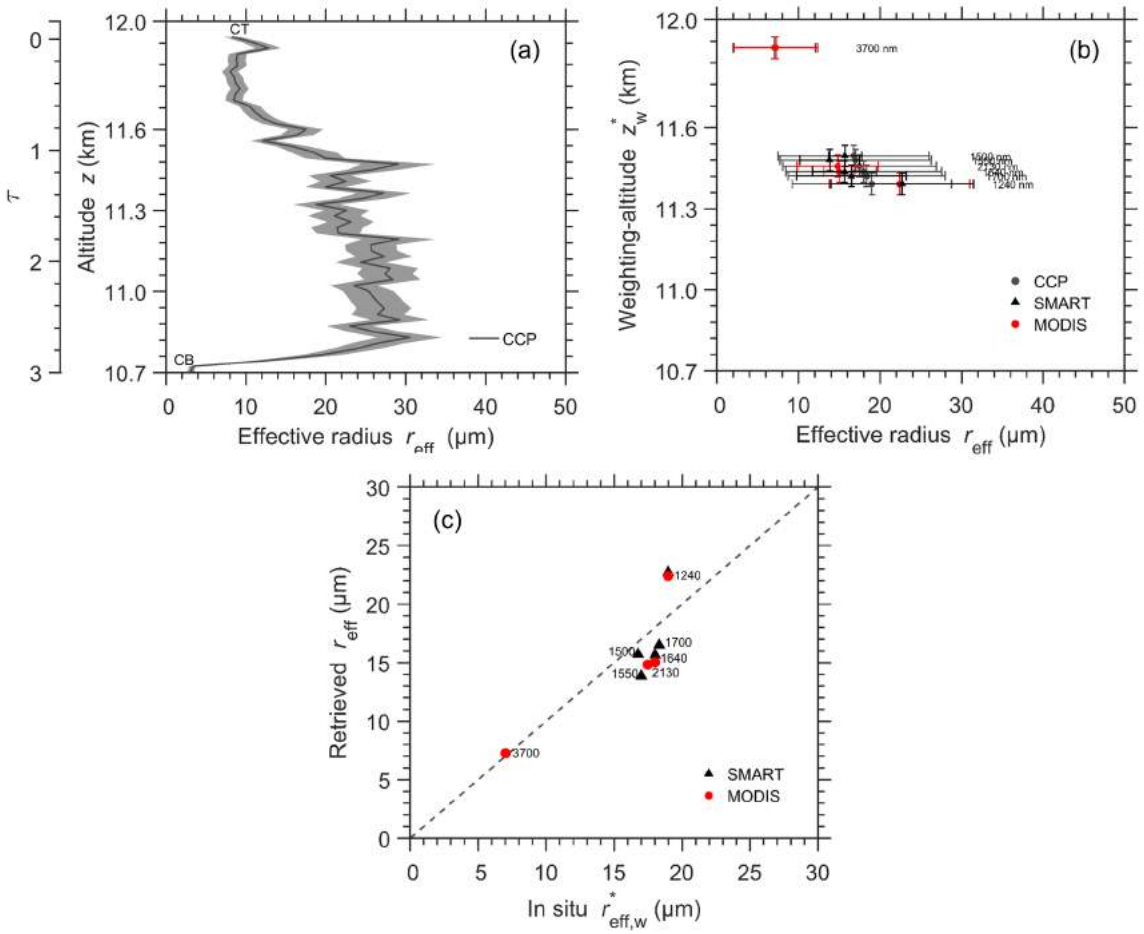

Figure 15. (a) Profile of effective radius $r_{\mathrm{eff}}(z)$ from the in situ measurements (CCP - solid line). The grey area represents the uncertainties of in situ data. (b) Comparison of the in situ $r^*_{\mathrm{eff,w}}$ and the mean value of r_{eff} retrieved by SMART and MODIS for λ between 1240 nm - 3700 nm. Horizontal error bars represent the standard deviation of effective radius, while vertical error bars are the uncertainty of the weighting-altitude. (c) Scatter plots between the in situ $r^*_{\mathrm{eff,w}}$ and the mean value of retrieved r_{eff}. The dashed line is the one-to-one line. The labels at each data point describe the wavelengths used to derive the r_{eff}.

~~potentially amplify in the retrieval algorithm. Airborne-satellite validation is one option to access the retrieval uncertainties . The cases for a comparison of airborne and satellite derived cloud products have to be selected carefully~~through the retrieval processes. Additional retrieval uncertainties may arise from, e.g., ~~cloud top altitudes, time delays should be minimized, cloud shadows should be discarded, and identical observation geometries of aircraft and satellite should be guaranteed.~~

~~A validation of upward (cloud-reflected) radiance and cloud products of MODIS-Aqua was performed for the case of cirrus and DDC using airborne SMART measurements during the two HALO campaigns,~~ the assumption of surface albedo, ice crystal shapes, and cloud vertical profile, as well as multilayer cloud scenes. Such situations make remote sensing of cloud

properties complex and challenging. Collocated airborne and satellite measurements incorporated with in situ observation is one option to assess the uncertainties. Two selected cloud cases, a cirrus above low liquid water clouds and a DCC topped by an anvil cirrus measured during the ML-CIRRUS and ACRIDICON-CHUVA. For cirrus measurements, it is found that MODIS radiances centered at λ = 1240 nm are systematically overestimated to those measured by SMART. The slope of linear regression between SMART and MODIS radiances centered at λ = 1240 is calculated, which results in a value of 0.86. This value is used to reduce MODIS radiance measurements centered at λ = 1240 nm. Comparisons of the mean value of upward radiance centered , are investigated in this study.

Spectral upward radiance measured above the clouds by SMART and MODIS are compared for the cirrus and DCC case. Comparisons of spectral upward radiance at λ = 645 nm , 1240 nm, and 1640 nm between 400 - 1800 nm yield a normalized mean absolute deviation with a maximum value of 1.36% between $0.2 - 7.7\%$ for the cirrus case and 6.7% $1.5 - 8.3\%$ for the DCC case. The higher deviations in case of DCC are related deviation is larger for the DCC case due to the fast cloud evolution, which already significantly changed changes the cloud properties within the 1 min during the time delay between SMART and MODIS . In addition, larger 3-D radiative effects are considered.

The MODIS cloud products were evaluated by airborne remote sensing and in situ measurements using different approaches. observation. A radiance ratio retrieval is applied to SMART and MODIS nadir upward radiances to simultaneously retrieve τ and $r_{\rm eff}$, as well as to investigate the propagation of measurement uncertainties into the retrieval. Two combinations, C1 ($I^{\uparrow}_{645}$ and $\Re_1$) and C2 ($I^{\uparrow}_{645}$ and $\Re_2$) are applied. Using used in the retrieval algorithm, where $\Re_1 = I^{\uparrow}_{1240}/I^{\uparrow}_{645}$ and $\Re_2 = I^{\uparrow}_{1240}/I^{\uparrow}_{645}$. By applying the ratios, the measurement uncertainties due to the radiometric calibration of the sensor cancel, and therefore the retrieval uncertainty is are reduced. In this way, the uncertainties of radiance ratio retrieval are smaller compared to the usual common bi-spectral method. Using different near-infrared wavelengths with different absorption characteristics by cloud particles in the retrieval algorithm provides $r_{\rm eff}$ from different cloud altitudes. A retrieval using C1 represents (1240 nm) results in an $r_{\rm eff}$ from a deeper lower cloud layer, while using C2 yields (1640 nm) results in an $r_{\rm eff}$ from a higher cloud layer . Therefore, those different combinations can be used to investigate the vertical variability layer closer to cloud top. To some degree, these two combinations can give a snapshot of the vertical variation of particle sizes in the cloud. However, using C1 in the retrieval algorithm results in larger uncertainties in the retrieved cloud properties due to the small absorption by cloud particles at it should be noted that retrievals using low absorption wavelength (e.g., λ = 1240 nm) will result in higher retrieval uncertainties.

The impact of assuming vertically homogeneous cloud in the retrieval is investigated. For ice clouds where the particle size typically decreases toward the cloud top, vertical weighting function is used to analyze the impact of the vertical profile assumption on the retrieval. A systematic deviation of the retrieved cloud properties is found between retrievals assuming a vertically homogeneous cloud lead to an underestimation in the retrieved $r_{\rm eff}$. In a sensitivity study for an exemplary ice cloud with cloud base effective radius $r_{\rm eff,b}$ of 40 compared to realistic cloud profiles. For ice clouds with decreasing $r_{\rm eff}$ towards cloud top, retrievals assuming vertically homogeneous cloud will result in an underestimation of $r_{\rm eff}$ of up to 1 µm, cloud topeffective radius $r_{\rm eff,t}$ of 10 m and total optical thickness τ_c of 3, an absolute deviation of 0.5 m and 0.4 m is obtained when using λ = 1240 nm and 1640 nm, respectively. While for an ice cloud with $r_{\rm eff,b}$ = 50 m, $r_{\rm eff,t}$ = 20 m, and τ_c = 15, an absolute

deviation of 0.5 mand 0.1 m is obtained when using λ = 1240 nm and 1640 nm, respectively. The results show, that the . The impact is larger for a retrieval using a wavelength where cloud particles absorb less radiation.In this case, more radiations are transmitted in the retrievals using wavelengths with smaller absorption by cloud particles (e.g., λ = 1240 nm), when lower cloud layers increasing the contribution of the lower cloud layerscontribute more strongly to the reflected radiance. The vertical weighting function has shownalso shows, that each individual cloud layer has a contribution to affects the absorption imprinted in the radiance reflected above cloud top . Furthermore, it is found that the profile of weighting function depends with a weighting depending on the cloud profile itself and the chosen wavelength. Therefore, it should be noted that the r_{eff} retrieved using this remote sensing technique do not represent r_{eff} by this solar remote sensing does not represent $r_{\mathrm{eff}}(z)$ at a single cloud layer only. The Instead, the retrieved r_{eff} describes a single bulk value, which represents bulk property of the entire cloud layer.

It is found that a higher surface albedo does change the vertical weighting function by increasing the weighting of the lower cloud layers. An enhanced surface reflections increases the interaction of radiation with the lower cloud layers and shifts the vertical weighting towards lower altitudes. Consequently, the retrieved r_{eff} will change for different surface albedos assumed in the forward simulation. For ice clouds where the particle size increases toward the cloud top, the retrieved value of r_{eff} will increase above a high reflecting surface. As observed during the ACRIDICON-CHUVA campaign, the surface heterogeneity in the Amazonian rainforest is high, where forested and deforested areas are located close to each other. In this condition, the surface albedo can change suddenly along the flight path. Therefore, in this study the MODIS BRDF/Albedo product is used, which consistently maps the spectral surface albedo over land surfaces.

The presence The occurrence of liquid water cloud underlying cirrus leads to significant discrepancies on below cirrus significantly leads to an overestimation of the retrieved cirrus properties. In general, the liquid water cloud acts similar to a bright surface, however the impact depends on the cloud properties and the wavelengths used τ, when the low cloud layer is omitted in the retrieval . The liquid water cloud enhances the radiance at visible wavelengths, which results to an overestimation of retrieved cirrus τ. While, the impact on the algorithm. In such conditions, the vertical weighting function of the cirrus will change and biases the retrieved cirrus r_{eff} is shown by changes of the vertical weighting function. When the cirrus τ is optically thin , if the cirrus layer is sufficiently thin ($\tau < 5$). The radiation is transmitted through the cirrus and reflected by the low liquid water cloud back to the cirrus. Consequently, the contribution of the lower cloud layers to the absorption absorption of radiation, and the vertical weighting function at cloud base in the lower layers is enhanced. For typical cirrus where the particle size decreases toward with decreasing particle size towards the cloud top, the retrieved cirrus r_{eff} becomes larger when a liquid water cloud is present occurs below the cirrus. When the cirrus τ is sufficiently thick ($\tau > 5$), the impact is reduced. The accuracy of the properties of the low liquid water cloud also determines the uncertainties of the retrieved cirrus properties. Underestimating the liquid water τ will artificially increase cirrus τ. When the liquid water r_{eff} is underestimated, the retrieved cirrus r_{eff} becomes larger than in reality. The opposite results are expected when the properties of the low liquid water cloud are overestimated.

The cloud properties retrieved by SMART and MODIS are compared for the two cloud cases. For the cirrus case, the normalized mean absolute deviation of the retrieved cloud properties from SMART and MODIS using combination C1 and C2 is found

~~in the range of up to 0.5 %~~ to be about 1.2 % for τ and ~~2.5 %~~ 2.1 % for r_{eff}. ~~These deviations are only~~ The deviations are slightly larger than ~~the deviations found for the upward radiance comparisons. This indicates,~~ those found in the comparisons of upward radiance, showing that the errors are only slightly ~~enhanced~~ amplified by the non-linearity in the retrieval algorithm. ~~The cirrus~~ Cirrus τ derived from the MODIS cloud product ~~results to a significant overestimation of up to 160 % compared to the retrievals using C1 and C2. This is due to the presence of liquid water cloud, which is not considered by the~~ overestimate the results from SMART and MODIS retrievals because the MODIS cloud product algorithm assumes only a single cloud layer for their operational retrievals. For the DCC case, ~~it results of up to 6.1 %~~ the deviation is found up to be about 3.5 % for τ and ~~17.5 %~~ 6.5 % for r_{eff}. In this case, the fast cloud evolution ~~is the major issue, as well as~~ and larger 3-D radiative effects ~~. The dependency between the retrieval of τ and r_{eff} is analyzed, which leads to small discrepancies in the retrieved τ between all approaches~~contribute most to the retrieval uncertainties. For both cloud cases, it is found that the particle size decreases ~~toward~~ towards the cloud top. ~~Mixture particle sizes are~~ A higher horizontal variability of r_{eff} is observed in the lower cloud layers, while ~~more homogeneous particle sizes are located in the higher cloud layers~~ in the upper layers the particle sizes are more homogeneous.

For the cirrus case, the ~~effective radius retrieved by remote sensing technique (SMART, MODIS, and MYD06_L2) is compared to the effective radius measured by the in situ instrument (CCP). The terminology of $r_{\mathrm{eff,z}}$ is introduced to describe the profile of effective radius measured by in situ sampled at a specific altitudes z, while the remote sensing effective radius~~ retrieved r_{eff} ~~represents a single bulk value. To compare in situ and retrieved effective radius, the~~ are compared to in situ measurements. To allow the comparison of both methods, the vertical weighting function ~~has to be considered. The vertical weighting function is calculated using the profiles of particle effective radius and ice water content measured by in situ. To calculate a particle size comparable to the retrieved effective radius, the in situ weighting-estimate $r^{*}_{\mathrm{eff,w}}$ is calculated by convoluting the profile of effective radius with the vertical weighting function. Additional~~ is considered. Using additional near-infrared wavelengths of SMART ~~at λ = 1700 nm, 1550 nm, and 1550 nm are employed in the radiance ratio retrieval to increase the information~~ and MODIS increases the information on particle size extracted from the spectral measurements ~~of SMART~~ and the vertical resolution of ~~the~~ retrieved r_{eff}. ~~Except the $r_{\mathrm{eff,2130}}$, the resulting~~ The normalized mean absolute deviation between in situ and retrieved ~~effective radius varies between 3.6 – 19.3 %, depending on the chosen wavelength and agree~~ r_{eff} ranges between 1.5 – 10.3 %, which falls within the standard deviation ~~value. The large deviation on the $r_{\mathrm{eff,2130}}$ which is up to 48 % is due to the presence of liquid water cloud, which is not considered by the MODIS cloud product~~with a correlation coefficient of 0.82. The variability of particle size distributions, the uncertainties of deriving r_{eff} from the in situ measurements, the presence of liquid water cloud below ~~the~~ cirrus, and the ~~simplification in the retrieval algorithm by assuming a vertically homogeneous cloud in the forward radiative transfer simulation are considered as the potential error contributors .~~

~~Additionally, the weighting-altitude z^{*}_{w} which characterizes the altitude of retrieved r_{eff} was calculated by convoluting the altitudes with the vertical weighting function. For wavelengths characterized by a high absorption by cloud particles, z^{*}_{w} are located in higher altitudes compared to wavelengths dominated by scattering. However, this conventional retrieval technique provides information only on the cloud-top effective radius because the~~ uncertainties caused by unconstrained choice of ice crystal shapes for the retrievals are identified as the major contributors which can reveal the discrepancies

between in situ and retrieved r_{eff} ~~represents a vertically weighted value where cloud top layers are weighted at most. Further studies have to be performed to develop an advanced method combined with spectral measurements of SMART, which has the potential to reconstruct the vertical profile of cloud microphysical properties. Simultaneous airborne and satellite remote sensing, and airborne in situ observations analyzed in this study for the two cases illustrate the need of well calibrated and carefully collocated measurements to develop, test, and validate cloud remote sensing methods~~. The assumption of vertically homogeneous cloud in the retrieval algorithm has only a small impact on the retrieval results.

Acknowledgements. This work was supported by the Max Planck Society (MPG), the German Science Foundation (DFG) funding the SPP HALO 1294 and the grants of WE 1900/35-1 and VO 1504/4-1, the German Aerospace Center (DLR), and the FAPESP (Sao Paulo Research Foundation) grants 2009/15235-8 and 2013/05014-0. The HGF is acknowledged for supports under the contract number W2/W3-60). ~~The author~~ C. Mahnke and R. Weigel received funding by the German BMBF within the joint ROMIC-project SPITFIRE (01LG1205A). Trismono C. Krisna acknowledges the Ministry of Research, Technology and Higher Education of the Republic of Indonesia (RISTEKDIKTI) and the German Academic Exchange Service (DAAD) for the research grant under the scheme of Indonesia-German Scholarship Programme (IGSP). The entire ML-CIRRUS and ACRIDICON-CHUVA ~~project~~ team is gratefully acknowledged for collaboration and support.

References

Ackerman, S., Moeller, C., Strabala, K., Gerber, H., Gumley, L., Menzel, W., and Tsay, S.-C.: Retrieval of effective microphysical properties of clouds: A wave cloud case study, Geophys. Res. Lett., 25, 1121–1124, 1998.

Afchine, A., Rolf, C., Costa, A., Spelten, N., Riese, M., Buchholz, B., Ebert, V., Heller, R., Kaufmann, S., Minikin, A., Voigt, C., Zöger, M., Smith, J., Lawson, P., Lykov, A., Khaykin, S., and Krämer, M.: Ice particle sampling from aircraft – influence of the probing position on the ice water content, Atmos. Meas. Tech., 2017, 1–23, doi:10.5194/amt-2017-373, 2017.

Anderson, G., Clough, S., Kneizys, F., Chetwynd, J., and Shettle, E.: AFGL Atmospheric Constituent Profiles (0–120 km), Tech. Rep. AFGL-TR-86-0110, AFGL (OPI), Hanscom AFB, MA 01736, 1986.

Baum, B. A., Yang, P., Nasiri, S., Heidinger, A. K., Heymsfield, A., and Li, J.: Bulk scattering properties for the remote sensing of ice clouds. Part III: High-resolution spectral models from 100 to 3250 cm^{-1}, J. Appl. Meteor., 46, 423–434, 2007.

Baum, B. A., Yang, P., Heymsfield, A. J., Bansemer, A., Cole, B. H., Merrelli, A., Schmitt, C., and Wang, C.: Ice cloud single-scattering property models with the full phase matrix at wavelengths from 0.2 to 100Âµm, J. Quant. Spectrosc. Radiat. Transfer, 146, 123 – 139, doi:https://doi.org/10.1016/j.jqsrt.2014.02.029, electromagnetic and Light Scattering by Nonspherical Particles XIV, 2014.

Baumgardner, D., Strapp, W., and Dye, J. E.: Evaluation of the Forward Scattering Spectrometer Probe. Part II: Corrections for Coincidence and Dead-Time Losses, J. Atmos. Oceanic Technol., 2, 626–632, doi:10.1175/1520-0426(1985)002<0626:EOTFSS>2.0.CO;2, 1985.

Berendes, T. A., Mecikalski, J. R., MacKenzie, W. M., Bedka, K. M., and Nair, U. S.: Convective cloud identification and classification in daytime satellite imagery using standard deviation limited adaptive clustering, J. Geophys. Res., 113, D20 207, 2008.

Bierwirth, E.: Airborne measurements of the spectral surface albedo over morocco and its influence on the radiative forcing of saharan dust, Ph.D. thesis, Johannes Gutenberg University Mainz, Germany, 2008.

Braga, R. C., Rosenfeld, D., Weigel, R., Jurkat, T., Andreae, M. O., Wendisch, M., Pöhlker, M. L., Klimach, T., Pöschl, U., Pöhlker, C., Voigt, C., Mahnke, C., Borrmann, S., Albrecht, R. I., Molleker, S., Vila, D. A., Machado, L. A. T., and Artaxo, P.: Comparing parameterized versus measured microphysical properties of tropical convective cloud bases during the ACRIDICON–CHUVA campaign, Atmos. Chem. Phys., 17, 7365–7386, doi:10.5194/acp-17-7365-2017, 2017.

Brückner, M., Pospichal, B., Macke, A., and Wendisch, M.: A new multispectral cloud retrieval method for ship-based solar transmissivity measurements, J. Geophys. Res. Atmos., 119, 11.338–11.354, doi:10.1002/2014JD021775, 2014.

Carlsen, T., Birnbaum, G., Ehrlich, A., Freitag, J., Heygster, G., Istomina, L., Kipfstuhl, S., Orsi, A., Schäfer, M., and Wendisch, M.: Comparison of different methods to retrieve optical-equivalent snow grain size in central Antarctica, The Cryosphere, 11, 2727–2741, doi:10.5194/tc-11-2727-2017, https://www.the-cryosphere.net/11/2727/2017/, 2017.

Cecchini, M. A., Machado, L. A. T., Andreae, M. O., Martin, S. T., Albrecht, R. I., Artaxo, P., Barbosa, H. M. J., Borrmann, S., Fütterer, D., Jurkat, T., Mahnke, C., Minikin, A., Molleker, S., Pöhlker, M. L., Pöschl, U., Rosenfeld, D., Voigt, C., Wenzierl, B., and Wendisch, M.: Sensitivities of Amazonian clouds to aerosols and updraft speed, Atmos. Chem. Phys. Discuss., 2017, 1–23, doi:10.5194/acp-2017-89, 2017.

Chang, F.-L. and Li, Z.: Estimating the vertical variation of cloud droplet effective radius using multispectral near-infrared satellite measurements, J. Geophys. Res., 107, AAC 7–1–AAC 7–12, doi:10.1029/2001JD000766, 2002.

Chang, F.-L. and Li, Z.: Retrieving vertical profiles of water-cloud droplet effective radius: Algorithm modification and preliminary application, J. Geophys. Res., 108, doi:10.1029/2003JD003906, 4763, 2003.

Chang, F. L. and Li, Z. Q.: A new method for detection of cirrus overlapping water clouds and determination of their optical properties, J. Atmos. Sci., 62, 3993–4009, 2005.

Chen, R. Y., Chang, F. L., Li, Z. Q., Ferraro, R., and Weng, F. Z.: Impact of the vertical variation of cloud droplet size on the estimation of cloud liquid water path and rain detection, J. Atmos. Sci., 64, 3843–3853, 2007.

Dye, J. E. and Baumgardner, D.: Evaluation of the Forward Scattering Spectrometer Probe. Part I: Electronic and Optical Studies, J. Atmos. Oceanic Technol., 1, 329–344, doi:10.1175/1520-0426(1984)001<0329:EOTFSS>2.0.CO;2, 1984.

Ehrlich, A., Wendisch, M., Bierwirth, E., Herber, A., and Schwarzenböck, A.: Ice crystal shape effects on solar radiative properties of Arctic mixed-phase clouds - Dependence on microphysical properties, Atmos. Res., 88, 266–276, 2008.

Ehrlich, A., Bierwirth, E., Istomina, L., and Wendisch, M.: Combined retrieval of Arctic liquid water cloud and surface snow properties using airborne spectral solar remote sensing, Atmos. Meas. Tech., 10, 3215–3230, doi:10.5194/amt-10-3215-2017, 2017.

Eichler, H., Ehrlich, A., Wendisch, M., Mioche, G., Gayet, J.-F., Wirth, M., Emde, C., and Minikin, A.: Influence of ice crystal shape on retrieval of cirrus optical thickness and effective radius: A case study, J. Geophys. Res., 114, D19203, doi:10.1029/2009JD012215, 2009.

Emde, C., Buras-Schnell, R., Kylling, A., Mayer, B., Gasteiger, J., Hamann, U., Kylling, J., Richter, B., Pause, C., Dowling, T., and Bugliaro, L.: The libRadtran software package for radiative transfer calculations (version 2.0.1), Geosci. Model Dev., 9, 1647–1672, doi:10.5194/gmd-9-1647-2016, 2016.

Finger, F., Werner, F., Klingebiel, M., Ehrlich, A., Jäkel, E., Voigt, M., Borrmann, S., Spichtinger, P., and Wendisch, M.: Spectral optical layer properties of cirrus from collocated airborne measurements and simulations, Atmos. Chem. Phys., 16, 7681–7693, doi:10.5194/acp-16-7681-2016, 2016.

Fisher, A.: Cloud and cloud-shadow detection in SPOT5 HRG imagery with automated morphological feature extraction, Remote Sensing, 6, 776–800, doi:10.3390/rs6010776, 2014.

Frey, W.: Airborne in situ measurements of ice particles in the tropical tropopause layer, Ph.D. thesis, Johannes Gutenberg-Universität, 2011.

Frey, W., Borrmann, S., Kunkel, D., Weigel, R., de Reus, M., Schlager, H., Roiger, A., Voigt, C., Hoor, P., Curtius, J., Krämer, M., Schiller, C., Volk, C. M., Homan, C. D., Fierli, F., Di Donfrancesco, G., Ulanovsky, A., Ravegnani, F., Sitnikov, N. M., Viciani, S., D'Amato, F., Shur, G. N., Belyaev, G. V., Law, K. S., and Cairo, F.: In situ measurements of tropical cloud properties in the West African Monsoon: Upper tropospheric ice clouds, Mesoscale Convective System outflow, and subvisual cirrus, Atmos. Chem. Phys., 11, 5569–5590, doi:10.5194/acp-11-5569-2011, 2011.

Fricke, C., Ehrlich, A., Jäkel, E., Bohn, B., Wirth, M., and Wendisch, M.: Influence of local surface albedo variability and ice crystal shape on passive remote sensing of thin cirrus, Atmos. Chem. Phys., 14, 1943–1958, doi:10.5194/acp-14-1943-2014, 2014.

Fu, Q. and Liou, K.: Parameterization of the radiative properties of cirrus clouds, J. Atmos. Sci., 50, 2008–2025, 1993.

Gueymard, C. A.: The sun's total and spectral irradiance for solar energy applications and solar radiation models, Sol. Energy, 76, 423–453, 2004.

Hahn, J., Warren, G., London, J., Chervin, M., and Jenne, R.: Atlas of simultaneous occurrence of different cloud types over land, 1984.

Heymsfield, A. J., Krämer, M., Luebke, A., Brown, P., Cziczo, D. J., Franklin, C., Lawson, P., Lohmann, U., McFarquhar, G., Ulanowski, Z., and Tricht, K. V.: Cirrus Clouds, Meteorological Monographs, 58, 2.1–2.26, doi:10.1175/AMSMONOGRAPHS-D-16-0010.1, 2017.

Holz, R. E., Platnick, S., Meyer, K., Vaughan, M., Heidinger, A., Yang, P., Wind, G., Dutcher, S., Ackerman, S., Amarasinghe, N., Nagle, F., and Wang, C.: Resolving ice cloud optical thickness biases between CALIOP and MODIS using infrared retrievals, Atmos. Chem. Phys., 16, 5075–5090, doi:10.5194/acp-16-5075-2016, 2016.

Jäkel, E., Walther, J., and Wendisch, M.: Thermodynamic phase retrieval of convective clouds: impact of sensor viewing geometry and vertical distribution of cloud properties, Atmos. Meas. Tech., 6, 539–547, doi:10.5194/amt-6-539-2013, 2013.

Jensen, M. P. and Del Genio, A. D.: Radiative and microphysical characteristics of deep convective systems in the tropical western Pacific, J. Appl. Meteor., 42, 1234–1254, 2003.

Järvinen, E., Schnaiter, M., Mioche, G., Jourdan, O., Shcherbakov, V. N., Costa, A., Afchine, A., Krämer, M., Heidelberg, F., Jurkat, T., Voigt, C., Schlager, H., Nichman, L., Gallagher, M., Hirst, E., Schmitt, C., Bansemer, A., Heymsfield, A., Lawson, P., Tricoli, U., Pfeilsticker, K., Vochezer, P., Möhler, O., and Leisner, T.: Quasi-Spherical Ice in Convective Clouds, J. Atmos. Sci., 73, 3885–3910, doi:10.1175/JAS-D-15-0365.1, 2016.

Kaufmann, S., Voigt, C., Jeßberger, P., Jurkat, T., Schlager, H., Schwarzenboeck, A., Klingebiel, M., and Thornberry, T.: In situ measurements of ice saturation in young contrails, Geophys. Res. Lett., 41, 702–709, 2014.

Kaufmann, S., Voigt, C., Jurkat, T., Thornberry, T., Fahey, D. W., Gao, R.-S., Schlage, R., Schäuble, D., and Zöger, M.: The airborne mass spectrometer AIMS – Part 1: AIMS-H_2O for UTLS water vapor measurements, Atmos. Meas. Tech., 9, 939–953, doi:10.5194/amt-9-939-2016, 2016.

Kim, D. Y. and Ramanathan, V.: Solar radiation budget and radiative forcing due to aerosols and clouds, J. Geophys. Res., 113, D02 203, 2008.

King, M., Tsay, S.-C., Platnick, S., Wang, M., and Liou, K.-N.: Cloud retrieval algorithms for MODIS: Optical thickness, effective particle radius, and thermodynamic phase, MODIS Algorithm Theoretical Basis Document, No. ATBD-MOD-05, 1997, 1997.

King, N. J. and Vaughan, G.: Using passive remote sensing to retrieve the vertical variation of cloud droplet size in marine stratocumulus: An assessment of information content and the potential for improved retrievals from hyperspectral measurements, J. Geophys. Res. Atmos., 117, doi:10.1029/2012JD017896, d15206, 2012.

King, N. J., Bower, K. N., Crosier, J., and Crawford, I.: Evaluating MODIS cloud retrievals with in situ observations from VOCALS-REx, Atmos. Chem. Phys., 13, 191–209, doi:10.5194/acp-13-191-2013, 2013.

Klingebiel, M., de Lozar, A., Molleker, S., Weigel, R., Roth, A., Schmidt, L., Meyer, J., Ehrlich, A., Neuber, R., Wendisch, M., and Borrmann, S.: Arctic low-level boundary layer clouds: in situ measurements and simulations of mono- and bimodal supercooled droplet size distributions at the top layer of liquid phase clouds, Atmos. Chem. Phys., 15, 617–631, doi:10.5194/acp-15-617-2015, 2015.

Korolev, A.: Limitations of the Wegener-Bergeron-Findeisen mechanism in the evolution of mixed-phase clouds, J. Atmos. Sci., 64, 3372–3375, 2007.

Lance, S., Brock, C. A., Rogers, D., and Gordon, J. A.: Water droplet calibration of the Cloud Droplet Probe (CDP) and in-flight performance in liquid, ice and mixed-phase clouds during ARCPAC, Atmos. Meas. Tech., 3, 1683–1706, doi:10.5194/amt-3-1683-2010, 2010.

Lane, T. P. and Sharman, R. D.: Intensity of thunderstorm-generated turbulence revealed by large-eddy simulation, Geophys. Res. Lett., 41, 2221–2227, doi:10.1002/2014GL059299, 2014.

Larar, A. M., Smith, W. L., Zhou, D. K., Liu, X., Revercomb, H., Taylor, J. P., Newman, S. M., and Schlüssel, P.: IASI spectral radiance validation inter-comparisons: case study assessment from the JAIVEx field campaign, Atmos. Chem. Phys., 10, 411–430, doi:10.5194/acp-10-411-2010, 2010.

LeBlanc, S. E., Pilewskie, P., Schmidt, K. S., and Coddington, O.: A spectral method for discriminating thermodynamic phase and retrieving cloud optical thickness and effective radius using transmitted solar radiance spectra, Atmos. Meas. Tech., 8, 1361–1383, doi:10.5194/amt-8-1361-2015, 2015.

Lindsey, D. T., Hillger, D. W., Grasso, L., Knaff, J. A., and Dostalek, J. F.: GOES climatology and analysis of thunderstorms with enhanced 3.9-mu m reflectivity, Mon. Wea. Rev., 134, 2342–2353, 2006.

Liou, K.-N.: Influence of cirrus clouds on weather and climate processes: A global perspective, Mon. Wea. Rev., 114, 1167–1199, 1986.

Luo, Z. J., Jeyaratnam, J., Iwasaki, S., Takahashi, H., and Anderson, R.: Convective vertical velocity and cloud internal vertical structure: An A-Train perspective, Geophys. Res. Lett., 41, 723–729, doi:10.1002/2013GL058922, 2013GL058922, 2014.

Lyapustin, A., Wang, Y., Xiong, X., Meister, G., Platnick, S., Levy, R., Franz, B., Korkin, S., Hilker, T., Tucker, J., Hall, F., Sellers, P., Wu, A., and Angal, A.: Scientific impact of MODIS C5 calibration degradation and C6+ improvements, Atmos. Meas. Tech., 7, 4353–4365, doi:10.5194/amt-7-4353-2014, 2014.

Mayer: Book Review: Barry, R.G., The Late R. Chorley: Atmosphere, Weather and Climate. Eighth Edition., Meteor. Z., 14, 79–80, 2005.

McFarquhar, G. and Heymsfield, A.: Microphysical characteristics of three anvils sampled during the central equatorial pacific experiment, J. Atmos. Sci., 53, 2401–2423, 1996.

McFarquhar, G. M. and Heymsfield, A. J.: The definition and significance of an effective radius for ice clouds, J. Atmos. Sci., 55, 2039–2052, 1998.

Mecikalski, J. R., Feltz, W. F., Murray, J. J., Johnson, D. B., Bedka, K. M., Bedka, S. T., Wimmers, A. J., Pavolonis, M., Berendies, T. A., Haggerty, J., Minnis, P., Bernstein, B., and Williams, E.: Aviation applications for satellite-based observations of cloud properties, convection initiation, in-flight icing, turbulence, and volcanic ash, Bull. Amer. Meteor. Soc., 88, 1589–+, 2007.

Miles, N. L., Verlinde, J., and Clothiaux, E. E.: Cloud droplet size distributions in low-level stratiform clouds, J. Atmos. Sci., 57, 295–311, 2000.

Miller, D. J., Zhang, Z., Ackerman, A. S., Platnick, S., and Baum, B. A.: The impact of cloud vertical profile on liquid water path retrieval based on the bispectral method: A theoretical study based on large-eddy simulations of shallow marine boundary layer clouds, J. Geophys. Res., 121, 4122–4141, doi:10.1002/2015JD024322, 2016.

Molleker, S., Borrmann, S., Schlager, H., Luo, B., Frey, W., Klingebiel, M., Weigel, R., Ebert, M., Mitev, V., Matthey, R., Woiwode, W., Oelhaf, H., Dörnbrack, A., Stratmann, G., Grooß, J.-U., Günther, G., Vogel, B., Müller, R., Krämer, M., Meyer, J., and Cairo, F.: Microphysical properties of synoptic-scale polar stratospheric clouds: in situ measurements of unexpectedly large HNO_3-containing particles in the Arctic vortex, Atmos. Chem. Phys., 14, 10 785–10 801, doi:10.5194/acp-14-10785-2014, 2014.

Mu, Q., Wu, A., Xiong, X., Doelling, D. R., Angal, A., Chang, T., and Bhatt, R.: Optimization of a Deep Convective Cloud Technique in Evaluating the Long-Term Radiometric Stability of MODIS Reflective Solar Bands, Remote Sensing, 9, 535, doi:10.3390/rs9060535, 2017.

Nagao, T. M., Suzuki, K., and Nakajima, T. Y.: Interpretation of Multiwavelength-Retrieved Droplet Effective Radii for Warm Water Clouds in Terms of In-Cloud Vertical Inhomogeneity by Using a Spectral Bin Microphysics Cloud Model, J. Atmos. Sci., 70, 2376–2392, doi:10.1175/JAS-D-12-0225.1, 2013.

Nakajima, T. and King, M.: Determination of the optical thickness and effective particle radius of clouds from reflected solar radiation measurements. Part I: Theory, J. Atmos. Sci., 47, 1878–1893, 1990.

Painemal, D. and Zuidema, P.: Assessment of MODIS cloud effective radius and optical thickness retrievals over the Southeast Pacific with VOCALS-REx in situ measurements, J. Geophys. Res., 116, doi:10.1029/2011JD016155, d24206, 2011.

Peng, S., Wen, J., Xiao, Q., You, D., Dou, B., Liu, Q., and Tang, Y.: Multi-Staged NDVI Dependent Snow-Free Land-Surface Shortwave Albedo Narrowband-to-Broadband (NTB) Coefficients and Their Sensitivity Analysis, Remote Sensing, 9, doi:10.3390/rs9010093, 2017.

Platnick, S.: Vertical photon transport in cloud remote sensing problems, J. Geophys. Res., 105, 22 919–22 935, 2000.

Platnick, S., King, M. D., Ackerman, S. A., Menzel, W. P., Baum, B. A., Riédi, J. C., and Frey, R. A.: The MODIS cloud products: Algorithms and examples from Terra, IEEE Trans. Geosci. Remote Sens., 41, 459–473, 2003.

Platnick, S., Meyer, K. G., King, M. D., Wind, G., Amarasinghe, N., Marchant, B., Arnold, G. T., Zhang, Z., Hubanks, P. A., Holz, R. E., Yang, P., Ridgway, W. L., and Riedi, J.: The MODIS Cloud Optical and Microphysical Products: Collection 6 Updates and Examples From Terra and Aqua, IEEE Trans. Geosci. Remote Sens., 55, 502–525, doi:10.1109/TGRS.2016.2610522, 2017.

Rolland, P. and Liou, K.: Surface variability effects on the remote sensing of thin cirrus optical and microphysical properties, J. Geophys. Res., 106, 22 965–22 977, doi:10.1029/2001JD900160, 2001.

Rosenfeld, D. and Lensky, I. M.: Satellite-based insights into precipitation formation processes in continental and maritime convective clouds, Bull. Amer. Meteor. Soc., 79, 2457–2476, 1998.

Rozanov, V. and Kokhanovsky, A.: Semianalytical cloud retrieval algorithm as applied to the top altitude and the cloud geometrical thickness determination from top-of-atmosphere reflectance measurements in the oxygen A band, J. Geophys. Res., 109, doi:10.1029/2003JD004 104, 2004.

Savtchenko, A., Kummerer, R., Smith, P., Gopalan, A., Kempler, S., and Leptoukh, G.: A-Train Data Depot: Bringing Atmospheric Measurements Together, IEEE Transactions on Geoscience and Remote Sensing, 46, 2788–2795, doi:10.1109/TGRS.2008.917600, 2008.

Schumacher, C., Stevenson, S. N., and Williams, C. R.: Vertical motions of the tropical convective cloud spectrum over Darwin, Australia, Quart. J. Roy. Meteor. Soc., 141, 2277–2288, doi:10.1002/qj.2520, 2015.

Schumann, U., Baumann, R., Baumgardner, D., Bedka, S. T., Duda, D. P., Freudenthaler, V., Gayet, J.-F., Heymsfield, A. J., Minnis, P., Quante, M., Raschke, E., Schlager, H., Vázquez-Navarro, M., Voigt, C., and Wang, Z.: Properties of individual contrails: a compilation of observations and some comparisons, Atmos. Chem. Phys., 17, 403–438, doi:10.5194/acp-17-403-2017, 2017.

Sherwood, S. C., Minnis, P., and McGill, M.: Deep convective cloud-top heights and their thermodynamic control during CRYSTAL-FACE, J. Geophys. Res., 109, doi:10.1029/2004JD004811, d20119, 2004.

Shettle, E.: Comments on the use of LOWTRAN in transmission calculations for sites with the ground elevated relative to sea level, Appl. Opt., 28, 1451–1452, 1989.

Shupe, M. D. and Intrieri, J. M.: Cloud radiative forcing of the Arctic surface: The influence of cloud properties, surface albedo, and solar zenith angle, J. Climate, 17, 616–628, 2004.

Slingo, A.: Sensitivity of the Earths Radiation Budget to Changes in Low Clouds, Nature, 343, 49–51, 1990.

Sohn, B.-J., Choi, M.-J., and Ryu, J.: Explaining darker deep convective clouds over the western Pacific than over tropical continental convective regions, Atmos. Meas. Tech., 8, 4573–4585, doi:10.5194/amt-8-4573-2015, 2015.

Sourdeval, O., C.-Labonnote, L., Baran, A. J., and Brogniez, G.: A methodology for simultaneous retrieval of ice and liquid water cloud properties. Part I: Information content and case study, Quart. J. Roy. Meteor. Soc., 141, 870–882, doi:10.1002/qj.2405, 2015.

Stamnes, K., Tsay, S.-C., Wiscombe, W., and Laszlo, I.: DISORT, a General-Purpose Fortran Program for Discrete-Ordinate-Method Radiative Transfer in Scattering and Emitting Layered Media: Documentation of Methodology, Tech. rep., Dept. of Physics and Engineering Physics, Stevens Institute of Technology, Hoboken, NJ 07030, 2000.

Stephens, G. L. and Kummerow, C. D.: The remote sensing of clouds and precipitation from space: A review, J. Atmos. Sci., 64, 3742–3765, 2007.

Strahler, A., Muller, J., and Members, M. S. T.: MODIS BRDF/Albedo product: Algorithm Theoretical Basis Document Version 5.0, 1999.

Stubenrauch, C., Rossow, W., Kinne, S., Ackerman, S., Cesana, G., Chepfer, H., Di Girolamo, L., Getzewich, B., Guignard, A., Heidinger, A., et al.: Assessment of global cloud datasets from satellites: Project and database initiated by the GEWEX radiation panel, Bull. Amer. Meteor. Soc., 94, 1031–1049, 2013.

Sun, J.-Q., Xiong, X., Barnes, W. L., and Guenther, B.: MODIS reflective solar bands on-orbit lunar calibration, IEEE Trans. Geosci. Remote Sens., 45, 2383–2393, 2007.

van Diedenhoven, B., Fridlind, A. M., Cairns, B., and Ackerman, A. S.: Variation of ice crystal size, shape, and asymmetry parameter in tops of tropical deep convective clouds, J. Geophys. Res., 119, 11,809–11,825, doi:10.1002/2014JD022385, 2014.

van Diedenhoven, B., Fridlind, A. M., Cairns, B., Ackerman, A. S., and Yorks, J. E.: Vertical variation of ice particle size in convective cloud tops, Geophys. Res. Lett., 43, 4586–4593, doi:10.1002/2016GL068548, 2016GL068548, 2016.

Voigt, C., Schlager, H., Ziereis, H., Kärcher, B., Luo, B., Schiller, C., Krämer, M., Popp, P., Irie, H., and Kondo, Y.: Nitric acid in cirrus clouds, Geophys Res Lett, 33, 2006.

Voigt, C., Jessberger, P., Jurkat, T., Kaufmann, S., Baumann, R., Schlager, H., Bobrowski, N., Giuffrida, G., and Salerno, G.: Evolution of CO2, SO2, HCl, and HNO3 in the volcanic plumes from Etna, Geophys. Res. Lett., 41, 2196–2203, 2014.

Voigt, C., Schumann, U., Minikin, A., Abdelmonem, A., Afchine, A., Borrmann, S., Boettcher, M., Buchholz, B., Bugliaro, L., Costa, A., Curtius, J., Dollner, M., Dörnbrack, A., Dreiling, V., Ebert, V., Ehrlich, A., Fix, A., Forster, L., Frank, F., Fütterer, D., Giez, A., Graf, K., Grooß, J.-U., Groß, S., Heimerl, K., Heinold, B., Hüneke, T., Järvinen, E., Jurkat, T., Kaufmann, S., Kenntner, M., Klingebiel, M., Klimach, T., Kohl, R., Krämer, M., Krisna, T. C., Luebke, A., Mayer, B., Mertes, S., Molleker, S., Petzold, A., Pfeilsticker, K., Port, M., Rapp, M., Reutter, P., Rolf, C., Rose, D., Sauer, D., Schäfler, A., Schlage, R., Schnaiter, M., Schneider, J., Spelten, N., Spichtinger, P., Stock, P., Walser, A., Weigel, R., Weinzierl, B., Wendisch, M., Werner, F., Wernli, H., Wirth, M., Zahn, A., Ziereis, H., and Zöger, M.: ML-CIRRUS: The Airborne Experiment on Natural Cirrus and Contrail Cirrus with the High-Altitude Long-Range Research Aircraft HALO, Bull. Amer. Meteor. Soc., 98, 271–288, doi:10.1175/BAMS-D-15-00213.1, 2017.

Wan, Z.: New refinements and validation of the collection-6 {MODIS} land-surface temperature/emissivity product, Remote Sensing of Environment, 140, 36 – 45, doi:10.1016/j.rse.2013.08.027, 2014.

Wang, L., Qu, J. J., Xiong, X., Hao, X., Xie, Y., and Che, N.: A new method for retrieving band 6 of aqua MODIS, IEEE Geoscience and Remote Sensing Letters, 3, 267–270, doi:10.1109/LGRS.2006.869966, 2006.

Wang, X., Liou, K. N., Ou, S. S. C., Mace, G. G., and Deng, M.: Remote sensing of cirrus cloud vertical size profile using MODIS data, J. Geophys. Res., 114, doi:10.1029/2008JD011327, d09205, 2009.

Warren, S., Hahn, C., and London, J.: Simultaneous occurrence of different cloud types, J. Climate Appl. Meteor., 24, 658–667, 1985.

Weigel, K., Rozanov, A., Azam, F., Bramstedt, K., Damadeo, R., Eichmann, K.-U., Gebhardt, C., Hurst, D., Kraemer, M., Lossow, S., Read, W., Spelten, N., Stiller, G. P., Walker, K. A., Weber, M., Bovensmann, H., and Burrows, J. P.: UTLS water vapour from SCIAMACHY limb measurementsV3.01 (2002-2012), Atmos. Meas. Tech., 9, 133–158, doi:10.5194/amt-9-133-2016, 2016.

Wendisch, M. and Brenguier, J.-L.: Airborne Measurements for Environmental Research – Methods and Instruments, Wiley–VCH Verlag GmbH & Co. KGaA, Weinheim, Germany, Weinheim, Germany, iSBN: 978-3-527-40996-9, 2013.

Wendisch, M. and Mayer, B.: Vertical distribution of spectral solar irradiance in the cloudless sky: A case study, Geophys. Res. Lett., 30, 1183–1186, doi:10.1029/2002GL016529, 2003.

Wendisch, M., Heintzenberg, J., and Bussemer, M.: Measurement-based aerosol forcing calculations: the influence of model complexity, Meteor. Z., 10, 45–60, 2001.

Wendisch, M., Pilewskie, P., Jäkel, E., Schmidt, S., Pommier, J., Howard, S., Jonsson, H. H., Guan, H., Schröder, M., and Mayer, B.: Airborne measurements of areal spectral surface albedo over different sea and land surfaces, J. Geophys. Res., 109, Art. No. D08 203, doi:10.1029/2003JD004392, 2004.

Wendisch, M., Pilewskie, P., Pommier, J., Howard, S., Yang, P., Heymsfield, A. J., Schmitt, C. G., Baumgardner, D., and Mayer, B.: Impact of cirrus crystal shape on solar spectral irradiance: A case study for subtropical cirrus, J. Geophys. Res., 110, doi:10.1029/2004JD005294, d03202, 2005.

Wendisch, M., Yang, P., and Pilewskie, P.: Effects of ice crystal habit on thermal infrared radiative properties and forcing of cirrus, J. Geophys. Res., 112, D03 202, doi:10.1029/2006JD007899, 2007.

Wendisch, M., Pöschl, U., Andreae, M. O., Machado, L. A. T., Albrecht, R., Schlager, H., Rosenfeld, D., Martin, S. T., Abdelmonem, A., Afchine, A., Araujo, A., Artaxo, R., Aufmhoff, H., Barbosa, H. M. J., Borrmann, S., Braga, R., Buchholz, B., Cecchini, M. A., Costa, A., Curtius, J., Dollner, M., Dorf, M., Dreiling, V., Ebert, V., Ehrlich, A., Ewald, F., Fisch, G., Fix, A., Frank, F., Fütterer, D., Heckl, C., Heidelberg, F., Hüneke, T., Jäkel, E., Järvinen, E., Jurkat, T., Kanter, S., Kästner, U., Kenntner, M., Kesselmeier, J., Klimach, T., Knecht, M., Kohl, R., Kölling, T., Krämer, M., Krüger, M., Krisna, T. C., Lavric, J. V., Longo, K., Mahnke, C., Manzi, A. O., Mayer, B., Mertes, S., Minikin, A., Molleker, S., Münch, S., Nillius, B., Pfeilsticker, K., Pöhlker, C., Roiger, A. E., Rose, D., Rosenow, D., Sauer, D., Schnaiter, M., Schneider, J., Schulz, C., de Souza, R. A. F., Spanu, A., Stock, P., Vila, D., Voigt, C., Walser, A., Walter, D., Weigel, R., Weinzierl, B., Werner, R., Yamasoe, M. A., Ziereis, H., Zinner, T., and Zöger, M.: The ACRIDICON-CHUVA campaign: Studying tropical deep convective clouds and precipitation over Amazonia using the new German research aircraft HALO, Bull. Am. Meteorol. Soc., doi:10.1175/BAMS-D-14-00255.1, 2016.

Werner, F., Siebert, H., Pilewskie, P., Schmeissner, T., Shaw, R. A., and Wendisch, M.: New airborne retrieval approach for trade wind cumulus properties under overlying cirrus, J. Geophys. Res. Atmos., 118, 3634–3649, doi:10.1002/jgrd.50334, 2013.

Wind, G., Platnick, S., King, M. D., Hubanks, P. A., Pavolonis, M. J., Heidinger, A. K., Yang, P., and Baum, B. A.: Multilayer Cloud Detection with the MODIS Near-Infrared Water Vapor Absorption Band, J. Appl. Meteorol. Climatol., 49, 2315–2333, doi:10.1175/2010JAMC2364.1, 2010.

Wiscombe, W.: Improved Mie scattering algorithms, Appl. Opt., 19, 1505–1509, 1980.

Wolf, K., Ehrlich, A., Hüneke, T., Pfeilsticker, K., Werner, F., Wirth, M., and Wendisch, M.: Potential of remote sensing of cirrus optical thickness by airborne spectral radiance measurements at different sideward viewing angles, Atmos. Chem. Phys., 17, 4283–4303, doi:10.5194/acp-17-4283-2017, 2017.

Wylie, D., Jackson, D. L., Menzel, W. P., and Bates, J. J.: Trends in global cloud cover in two decades of HIRS observations, J. Climate, 18, 3021–3031, 2005.

Xiong, X., Sun, J., Chiang, K., Xiong, S., and Barnes, W.: MODIS on-orbit characterization using the moon, Sensors, Systems And Next-Generation Satellites Vi, 4881, 299–307, 2003.

Xiong, X. X. and Barnes, W.: An overview of MODIS radiometric calibration and characterization, Adv. Atmos. Sci., 23, 69–79, 2006.

Yang, P., Bi, L., Baum, B. A., Liou, K.-N., Kattawar, G. W., Mishchenko, M. I., and Cole, B.: Spectrally consistent scattering, absorption, and polarization properties of atmospheric ice crystals at wavelengths from 0.2 to 100 μm, J. Atmos. Sci., 70, 330–347, doi:10.1175/JAS-D-12-039.1, 2013.

Zhang, S., Xue, H., and Feingold, G.: Vertical profiles of droplet effective radius in shallow convective clouds, Atmos. Chem. Phys., 11, 4633–4644, doi:10.5194/acp-11-4633-2011, 2011.

Zhang, Z. B., Platnick, S., Yang, P., Heidinger, A. K., and Comstock, J. M.: Effects of ice particle size vertical inhomogeneity on the passive remote sensing of ice clouds, J. Geophys. Res., 115, D17 203, doi:10.1029/2010JD013835, 2010.